On-Chip Biosensing Platforms based on Gold and Silicon Optical Nano-Resonators

Özlem Yavaş

Supervisor: Prof. Romain Quidant

Co-supervisor: Dr. Vanesa Sanz Beltran

Plasmon Nano-Optics Group

This dissertation is submitted for a degree of

Philosophy Doctor

UPC-PMT, Castelldefels February 2019

to my family

Acknowledgements

"If I have seen further it is by standing on the shoulders of Giants."

Isaac Newton

Taking credit for this PhD thesis all by myself would be tantamount to hypocrisy. There are many people listed below, who have been crucially important for the success of the projects I finished during my PhD. In my opinion, if you talk about success, you have to also talk about luck. Below lies the proof of how lucky I was.

First of all, I want to thank Prof. Romain Quidant for being an extremely positive, motivating, understanding and trusting group leader. With his support, even the hardest problems ahead became achievable. His kindness and optimism always inspired me (and it still does) and I consider myself extremely lucky to have worked with Romain as my PhD supervisor. Thank you!

I want to also thank my co-supervisor Dr. Vanesa Sanz who has always been supportive and comforting in the times of desperation in the lab. She developed the surface functionalization protocols I used for LSPR experiments and I am very happy to have had her around during my PhD and learn from her. She set a great example of hardworking, dedicated scientist for me.

Besides my official supervisors Romain and Vanesa, I was extremely lucky to have Dr. Mikael Svedendahl's guidance during the last years of my PhD. All the Comsol simulations presented in this thesis have been done by Mikael, but that is only the tip of the iceberg showing his support and help. He is an exceptionally smart, efficient and kind person who always supported and encouraged me.

I have to mention that if I had seen further, it is by standing on the shoulders of Dr. Maria Alejandra Ortega, Dr. Srdjan Acimovic, Dr. Johann Berthelot and other former members of PNO who worked on the biosensing projects. Their efforts in the project before I have started my PhD made my work easier. I had the privilege to build on what they have started. I thank to Mariale for training me on her last weeks at ICFO as a PhD student. I was lucky to have her around in the very beginning. I thank Srdjan, for all the useful discussions on Skype and always motivating and encouraging me about the LSPR project.

I thank Dr. Paulina Dobosz for keeping my curiosity alive and exciting me for going back to the lab, whenever I needed a push. I learned a lot from her. She had been a great friend and supportive colleague. I also owe her all of my 4 hangovers in Barcelona during the last 4 years.

I also thank Dr. Luis Miguel Fidalgo for all the useful discussions on micro fabrication. He was always able to see the big picture and motivate me.

I thank Jose Garcia Guirado, my officemate and labmate for his help and training in the cleanroom. I appreciate the entertainment he provided by his ''only jose'' stickers he puts on everything. I am also thankful to him for keeping me young and fresh in a freezing office. There was no winner of the AC wars during the last 5 years, only constant sore throat on my side and constant sweating on Jose's.

I need to express my gratitude to the whole PNO group for keeping a functional work environment and their support. I especially thank Alexia Stollman for reading my thesis rigorously and helping me to improve it.

I thank to Dr. Jil Schwender for being the nicest and sweetest alarm clock I have ever had. Starting every day with a friendly chat and coffee together made getting up easier. She had been an incredible friend the whole time and we laughed and cried together along the way. Thank you girl!

Dr. Michal Tomza deserves to be mentioned here as he had been a great friend, a psychologist, a cook, a running trainer, a tour guide, and a tubing cutter for me! He had been my neighbor, my best friend and he even acted like a parent when I needed one around. He deserves to be proud of this thesis. And yes, at times, he cut tygon tubings in the lab for me, so that I can do my experiments without focusing on this menial task. He claimed to do it because it helped him take a break from his work, but I think he actually liked our long gossips.

Out of all of the people I met at ICFO, I have to thank Adeel Afridi the most, because he is a jealous and possessive friend who would not forgive me if I don't. I don't know how he will continue his PhD without me. I am so grateful for our ridiculous discussions about very philosophical subjects. I honestly don't know who will answer my hardest questions in life if I don't have him around on a daily basis.

My friends, scattered to different countries, receive my constant gratitude not only for the support with my PhD thesis, but also for their love and friendship. I don't have any siblings, but I know that if I had sisters, they would be just like Ece, Özgün and Burcu! They always had time for me when I needed to chat. By being there for me no matter what, they made distances small, goals achievable and life brighter. I thank all of them one by one.

Finally and most importantly, I am grateful to my wonderful family. I thank my parents for bearing with me for 30 years, for being supportive, loving and caring. I thank my mom for being the most wonderful and giving person that she is, for being my best friend, and for all the wonderful food that she stuffed in my freezer whenever she visited me! I thank my father for only caring about my happiness; always giving the priority to me being happy. I know that me getting a PhD in physics means more to him than to anybody else in the world. However, if today I decided to quit, he would support me regardless. Knowing this keeps me going. Teşekkürler bikilerim!

I thank my partner, Tomek, for the warmth he continuously provides. I am grateful to him for believing in my success, contributing to my growth and bringing food to ICFO on the days I had to work until late. I don't know how I got so lucky to have him and his loving family by my side.

You see, I was not alone on this path and I am very grateful for all those wonderful people and many more that I could not refer here. I am the luckiest person in the world. And I also worked hard for this PhD. ;)

Abstract

Point-of-care (POC) devices are compact, mobile and fast detection platforms expected to advance early diagnosis, treatment monitoring and personalized healthcare, and revolutionize today's healthcare system, especially in remote areas. The need for POC devices strongly drives the development of novel biosensor technology. Building a small, fast, simple, and sensitive platform for biomolecule detection is a challenge that relies on the integration of multiple fields of expertise and engineering.

Optical nanoresonators have shown great promise as label-free biosensors because of direct light coupling and sub-wavelength sensing modes. Metallic nanoresonators with localized surface plasmon resonances (LSPR) are already well studied and were proven a solid alternative to the commercialized surface plasmon resonance (SPR) sensors. More recently, dielectric nanoresonators have also gained traction due to the reduced losses and the ability to manipulate both the electric and magnetic components of the incident light.

In this thesis, we advance the field of biosensing and use optical nanoresonators as operative platforms relevant for disease diagnosis and treatment monitoring. By combining different optimized optical nanoresonators, both metallic and dielectric, with state-of-the-art microfluidics and surface chemistry, we have developed and tested several detection platforms.

We first focused on developing a microfluidic lab-on-chip device for multiplexed biosensing utilizing the LSPR of gold nanoresonator arrays. By simultaneously tracking the extinction of 32 sensor arrays, we demonstrated multiplexed quantitative detection of four breast cancer markers in human serum. We showed that with well-optimized immunoassays, a low limit of detection (LOD) can be reached, paving the way towards clinically-relevant POC devices.

Additionally, we implemented silicon nanoresonators supporting Mie resonances into functional and clinically-relevant applications. By integrating several arrays of Si nanoresonators with state-of-the-art microfluidics, we demonstrated their ability to detect cancer markers in human serum with high sensitivity and high specificity.

Furthermore, we showed that the fabrication of Si nanoresonator array using low cost and scalable projection lithography leads to sufficiently low limits of detection, while enabling cheaper and faster sensor production for future POC applications. We also investigated the respective role of electric and magnetic dipole resonances and showed that they are associated with two different transduction mechanisms: resonance redshift and extinction decrease.

Our work advances the development of future point-of-care sensing platforms for fast and low cost health monitoring at the molecular scale.

Table of Contents

List of Figures

List of Tables

INTRODUCTION

Early diagnosis, personalized treatments and treatment monitoring are essential in the fight against devastating disorders. Biosensing is a key element in all of them. Today's healthcare system highly depends on sample diagnostics by large laboratories outside of the doctor's office. A single doctor visit is generally not enough to reach a diagnosis and define a treatment. Usually patients will see the doctor, have samples extracted, wait for the sample to be analyzed in an external laboratory facility before returning to the doctor to be informed of their condition. The impracticality of these time consuming and costly processes is significantly amplified in remote areas and/or underdeveloped countries. The additional challenges from the travel distances as well as the scarcity of resources lead to even longer waiting times before a diagnoses can be made, which have serious consequences for patients, especially those requiring urgent care. This pushed many scientists and researchers to develop point-of-care (POC) diagnostic devices and systems. Their goal is to bring the steps of sample collection, analytical testing and the result interpretation together, all within the immediate vicinity of the patient.

According to World Health Organization (WHO), a POC device needs to be Affordable, Sensitive, Specific, User-friendly, Rapid and Equipment-Delivered (ASSURED). One specific ASSURED method was already used by Persians in the 11th century in the form of urinalysis. This technique relied on collecting urine samples from a patient and checking its odour and colour to make a diagnosis. It was affordable, sensitive and specific for its time, user-friendly (easy to perform), very rapid (no need for any equipment or preparation), and equipment-delivered (easy diagnosis taking place in vicinity of the patient).

Today, the goal of scientists and engineers in this field is to develop ASSURED POC diagnostic devices for various kinds of patient samples, which are not only boasting improved specificity and sensitivity but also, remain highly-affordable, easy to use and fast. This is an extremely complex task as biological processes are highly complex, even at the single-cell level. Hundreds of molecules collaborate to perform a single vital function in a cell. For multicellular organisms as complex as humans, it is extremely challenging, if not impossible, to build a universal device for diagnostics. Simultaneous and sensitive detection of multiple biomarkers is already required to diagnose or track individual conditions. Tackling this very

complex problem requires researchers to combine multiple disciplines and technologies. Especially, keeping in mind the necessity of performing diagnostics fast and in the vicinity of the patients in critical cases, lots of effort needs to be put into this research with the goal of moving towards specified POC devices for certain types of samples and diseases. Lab-on-chip (LOC) technology is one of the key elements that reduces the cost, size and reagent volume of POC devices. It enables the automation of the multiple analytical steps of a diagnostic assay and offers user-friendly and mobile devices. It is a strong enabling tool, developed over the last few decades, both in research and for the industry. It has already achieved successful commercialization for certain applications such as ELISA with integrated sample processing and glucose monitoring. Some microfluidic chips that can perform sample preparation, cell lysis, purification and many other laborious analytical steps already exist, proving that an entire laboratory can fit into of a few square centimetres. The development of such industrial chips, which can perform tens of different functions, relies on the development of small modules with separate single functions that are then combined to form a larger more complex system. This has the significant advantage of allowing researchers to develop and test a single function at a time. Working on simpler modules allows faster design iteration, with chips tested continuously in a chip-in-a-lab manner, i.e. placing them in bulky custom-made control and read-out set-ups for quick, customized and specific testing. Then, these separately-tested individual modules are integrated to form the complex and ultimately multifunctional industrial chips for direct use in POC devices. Therefore, even though current academic efforts in the direction of POC LOC system developments look more like chip-in-a-lab then lab-on-a-chip, these steps are crucial in the development of this technology for real life applications. Another key element of POC devices is the biosensing mechanism, which is responsible for the detection of the specifically targeted biomarkers of the POC device, and ultimately determines the device sensitivity. It essentially transduces the biochemical information into a detectable signal. For clinical diagnostics, the gold standard biosensing technique is enzyme linked immunosorbent assay (ELISA). This method, used both in research and by large analytical laboratories, requires using bulky well-plates and large amounts (microliters to millilitres) of samples and reagents as well as cumbersome plate readers. It is clearly not a method suitable for POC diagnostics.

The chemistry used for ELISA relies on multiple incubation steps of labelled or conjugated antibodies and substrate solutions. The available biosensing transduction methods that can be combined with LOC technologies are based on fluorescence microscopy or impedance measurements. Optical detection schemes

hold great advantages, such as the possibility of label-free measurements, ease of performance, and scalability.

Surface Plasmon Resonance (SPR) is an optical phenomenon that is highly sensitive to events on the surface of the metals, making it an interesting tool for biosensing. SPR sensing is based on exciting surface plasmon resonances at the interface of the metal and its surrounding environment, and therefore requires a specific optical configuration. This requirement is not optimal with the portability and small size expected from POC devices. A simpler method involves using a localised surface plasmon resonance (LSPR). This resonance is excited by incident light interacting with subwavelength scale metallic nanostructures, as opposed to thin films used for SPR-based sensors. LSPR is very sensitive to changes in its environment, allowing a simpler sensing setup. It is therefore not surprising that LSPR phenomenon has already been extensively studied and has already been used for biosensing applications. Its integration with microfluidic chips however, was relatively immature at the beginning of this work since most studies lacked clinically-relevant results and/or fully functional, practical and an automatable chip design for multiple analyte detection.

More recently, dielectric nanostructures with a high refractive index have attracted attention due to their ability to manipulate the electric and magnetic components of the incident light. They are proposed as an alternative to metallic nanostructures for SPR sensing because they do not suffer from ohmic losses and provide better quality factor resonances with unique optical properties allowing the engineering of meta-properties. All-dielectric nanophotonics is a rapidly growing field for a number of different applications. However, there are only a few studies, so far, in the biosensing field. They all lack realistic and clinically-relevant experiments, leaving a wide gap in the literature, with a significant potential impact.

The goal of this thesis work is to develop on-chip biosensing platforms that integrate microfluidics, optical nanoresonators, and relevant surface chemistry achieving robust, sensitive, specific, rapid, and real-time detection of clinically-relevant biomarkers. The first objective of the project is to develop an LSPR based microfluidic platform for the multiplexed detection of cancer markers in human serum. The second objective is to explore and develop sensing with dielectric nanoresonators, as opposed to the classically-used metal nanostructures for on-chip biosensing applications.

The multidisciplinary nature of this work integrates different disciplines of science and technology. In Chapter 1, the different concepts involved in this research are

explained. These include optical nanoresonators, microfluidics, and the surface chemistry used in chip fabrication and for biosensing.

Chapter 2 presents the experimental techniques that are used to manufacture and operate the lab-on-chip platforms, integrate the sensors, and interpret the experimental results.

Chapter 3 focuses on the development of the LOC platform with LSPR based sensors for multiplexed and fully-automated biosensing. The detection of four breast cancer markers in human serum is demonstrated. In addition, the chip design and system optimization are shown, as well as a comparison with the gold standard ELISA technique.

Chapter 4 presents the results of on-chip sensing experiments with periodic silicon nanoresonator arrays fabricated by electron beam lithography. The electric dipole resonances of the nanoresonators and the diffractive modes of the periodic nanoresonator arrays are demonstrated to be effective for sensing. Results from cancer marker detection experiments are also presented and compared with the results obtained for the same bioassays using LSPR sensors.

Chapter 5 focuses on semi-random silicon nanoresonator arrays to explore the different transduction mechanisms of the nanoresonators. These resonators are no longer periodic and do no longer need to be fabricated by long and costly electron beam lithography. The different transduction mechanisms are associated with different resonance modes through simulations and their sensing performance is then demonstrated for cancer biomarker detection.

1 CONCEPTS AND BACKGROUND

The sensing platforms developed during this PhD work are highly multidisciplinary, integrating fields from nanophotonics and microfluidics to surface and biochemistry. The plasmonic nanostructures are used for optical sensing. Microfluidics is used to deliver samples and target molecules to the sensors, as well as sensor preparation steps in a controlled environment. Surface chemistry is used to prepare the sensors to capture the target molecules and run the immunoassays.

In this chapter, I introduce the basic concepts that are involved in this dissertation, starting with presenting the basics of resonant light scattering nanostructures in both metallic and dielectric nanoparticles. Next, I focus on microfluidics, followed by the surface chemistry that was used in our experimental scheme.

1.1 Light-nanoparticle interaction

Light scattering by small particles is a well-known and studied phenomenon, historically originating from the work of Lord Rayleigh in 1871.[1] When light is incident on a small particle, the electric charges in the particle are displaced by the electric field of the incident light, setting them into oscillatory motion. These accelerating charges radiate electromagnetic energy, which is known as scattering. In addition to scattering, some of the incident energy is transformed into heat, resulting in absorption. Therefore, the incident light is extinct due to both scattering from and absorption by the particle. Both of these contributions depend significantly on the properties of the particle material and the surrounding media, as will be discussed in this chapter.

Mie theory, developed by Gustav Mie in 1908, describes the electromagnetic field scattered and absorbed by a homogeneous and isotropic sphere of an arbitrary radius a, due to an incident plane wave of wavelength λ. Mie theory involves expanding electromagnetic fields into spherical harmonics and determining their expansion coefficients using boundary conditions. According to Mie theory[2] , the

scattering, extinction and absorption cross-sections of the particle can be expressed as follows:

$$C_{sc}^{Mie} = \frac{\lambda^2}{2\pi}\sum_{n=1}^{\infty}(2n+1)\{|a_n|^2 + |b_n|^2\},$$

$$C_{ext}^{Mie} = \frac{\lambda^2}{2\pi}\sum_{n=1}^{\infty}(2n+1)Re\{a_n + b_n\}, \quad (1)$$

$$C_{abs}^{Mie} = C_{ext} - C_{sc,}$$

where the expansion coefficients a and b are[2]:

$$a_n = \frac{m\psi_n(mx)\psi_n'(x) - \psi_n\psi_n'(mx)}{m\psi_n(mx)\xi_n'(x) - \xi_n(x)\psi_n'(mx)}$$

$$b_n = \frac{\psi_n(mx)\psi_n'(x) - m\psi_n\psi_n'(mx)}{\psi_n(mx)\xi_n'(x) - m\xi_n(x)\psi_n'(mx)} \quad (2)$$

ψ and ξ are related to Bessel functions of the first kind. m is the relative refractive index $m = \frac{n_{particle}}{n_{medium}}$, and x is the size factor $x = ka$, where k is the wave vector in the medium. These cross sections are valid for particles of all materials and sizes.

Let's consider the example where a homogeneous subwavelength sphere with dielectric function $\epsilon(\omega)$ and radius a ($a \ll \lambda$) is placed into a homogeneous medium with dielecric constant ε_m. Asϵ_m. As the particle size is much smaller than the wavelength of the incident light, the phase of the harmonically oscillating electromagnetic field can be considered constant across the particle volume ($E = E_0 z$). This reduces the problem into one with a particle in an electrostatic field (Figure 1-1).

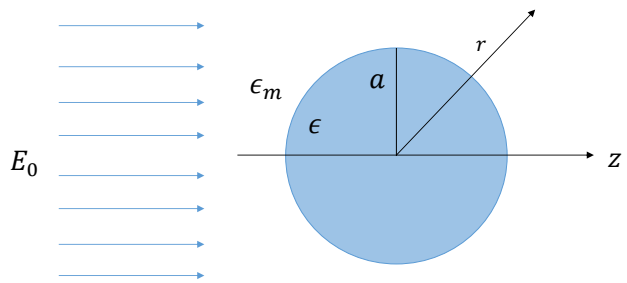

Figure 1-1 Sketch of a spherical nanoparticle placed into an electrostatic field (modified from S.A.Maier[3]).

Solving the Laplace equation and applying the boundary conditions, the electric field inside and outside the particle is found to be:

$$E_{in} = \frac{3\epsilon_m}{\epsilon + 2\epsilon_m} E_{0,}$$
$$E_{out} = E_0 + \frac{3n(n\,.p) - p}{4\pi\epsilon_0\epsilon_m}\left(\frac{1}{r^3}\right), \tag{3}$$

where n is the normal unit vector pointing the location where the field is calculated, $p = \epsilon_0\,\epsilon_m \alpha E_0$ is the dipole moment of the particle and r is the distance from the center of the sphere to the point where the field is calculated. The polarizability of the particle is then[3]:

$$\alpha = 4\pi a^3 \frac{\epsilon - \epsilon_m}{\epsilon + 2\epsilon_m}, \tag{4}$$

From this equation one can see that when $|\varepsilon + 2\,\varepsilon_m|$ reaches a minimum, the polarizability experiences a resonant enhancement. The scattering and absorption cross sections of the particle are given by[3]:

$$C_{sc} = \frac{k^4}{6\pi}|\alpha|^2 = \frac{8\pi}{3}k^4 a^6 \left|\frac{\epsilon - \epsilon_m}{\epsilon + 2\epsilon_m}\right|^2,$$
$$C_{abs} = kIm[\alpha] = 4\pi k\, a^3 Im\left[\frac{\epsilon - \epsilon_m}{\epsilon + 2\epsilon_m}\right]. \tag{5}$$

Note that the same results in Eq. 5 can be derived from the general Mie theory cross sections by retaining only the first term (by coefficients a_1 and b_1), which represents the dipole mode and neglecting the other terms.

It is also interesting to note that for small particles absorption is the dominating mechanism, with its cross-section, scaling with α^3, as opposed to a^6 for scattering.

As the size of the particle increases, the dipole resonance redshifts due to the weakening of the restoring force caused by polarized charges in the particle. The bigger the particle, the more separated the charges at the opposite ends of the particle are. This results in a decrease of their interaction, shifting the resonance to longer wavelengths.

The resonance behavior of a spherical particle is very well known and used as an example for its simplicity. The shape of the particle however also heavily influences this resonant behavior. The more complex the shape of the nanostructure, the more complex its optical response will be. These responses are then usually simulated numerically, using models and different software, because there is no analytical solution to Maxwell's equations for them.

It can be seen from Eq. 5 that the extinction ($C_{ext} = C_{sc} + C_{abs}$) experiences a resonance also when the polarizability is resonant, thus, it also depends on the dielectric function of the medium. This is the reason why these nanostructures make good sensors and the key takeaway message of this section: any changes in a nanostructures' dielectric environment can be directly correlated to changes in its' optical behavior.

So far, the equations in this section are valid for nanoresonators of any material. From now on, we will focus on metallic and dielectric nanoresonators only, as these are the materials used in the sensors developed in this thesis. The difference between the dielectric and metallic nanostructures stems from their different dielectric functions and the existence of the free electrons in metals as opposed to dielectric materials.

1.1.1 Resonances of metallic nanoresonators

The free electrons in the metals oscillate around the fixed positively charged background due to the electric field of the incident light, resulting in electromagnetic excitations confined on the surface of the metal called surface plasmons. For propagating plasmons, matching the momentum of the incident field to the one of the surface plasmons requires special geometries[4–6] which can be complex, whereas in subwavelength nanoparticles direct illumination is able to excite resonances once the resonance condition, shown above, is satisfied. These resonances of the metallic nanostructures are called localized surface plasmon resonances (LSPR). Metallic nanoresonators such as gold and silver can exhibit

their resonances in the visible light spectrum, making them attractive and practical candidates for many applications in biomedicine and sensing.[7–10] Besides this, these nanoparticles highly localize and enhance the electromagnetic fields around them in the spatial ranges that match the sizes of biomolecules such as proteins and antibodies (mode-analyte overlap). This is why these particles are very sensitive to molecules in their vicinity.

Drude model approximates the dielectric function of a metal:

$$\epsilon_{Drude}(\omega) = 1 - \frac{\omega_p^2}{\omega^2 + i\gamma\omega}, \tag{6}$$

where $\omega_p = \sqrt{n_e e^2/(m_e \epsilon_0)}$ is the plasma frequency, n_e is the electron density of the metal and e and m_e are the charge and mass of an electron. γ is the damping term and ω is the frequency of the incident light. The wavelength dependence of the dielectric function of gold is shown in Figure 1-2. One can see that the imaginary part of the dielectric function is non-zero, which is a damping factor of the oscillations, indicating losses. These result in a widening of the resonance peaks, increasing the full width at half maximum ($w = FWHM$) which corresponds to a lowering of the quality factor ($= \lambda_{res}/w$).

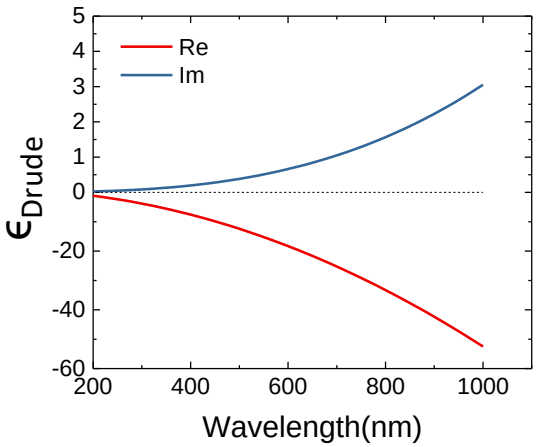

Figure 1-2 Dielectric function of gold calculated by Drude model. The values for gold taken from [Johnson and Christy, 1972].[11]

LSPR is a very well-studied phenomenon which is already being used in some applications in the fields of biosensing, cancer treatment, SERS and imaging.[7–10,12] The following sections and chapters of this thesis focus on the biosensing applications of LSPR phenomena.

1.1.2 Resonances of dielectric nanoresonators

Even though it has been so many years since the Mie theory completely described the multipolar resonances of dielectric particles, interest in this field has recently been renewed with the emergence of all-dielectric nanophotonics field, which allow increasing control over sensor design, fabrication and characterization techniques.[13,14] Due to the ability of dielectric nanoparticles to support electric displacement currents inside them, they can exhibit magnetic dipole resonances as opposed to their metallic counterparts. This ability to manipulate both the electric and magnetic components of the electromagnetic waves incident upon them combined with their low-loss resonances paves the way to applications such as cloaking[12], superlensing[15], negative refraction[16] and suggest them as an alternative to their metallic counterparts. The high quality factor resonance peaks of dielectric nanostructures, along with their easily engineered resonance modes are what has attracted the attention of the sensing community recently.[17–20]

The magnetic modes are characterized by the displacement current inside the particle inducing a magnetic dipole moment in the orthogonal direction. Focusing on Si nanocylinders (Si NCs), as they are used in this thesis for sensing applications, Figure 1-3 shows the magnetic and electric dipole (MD and ED) resonances of the Si NCs. As shown in Figure 1-3a, the circular electric displacement current requires sufficient electric field retardation at the bottom and top of the particle, therefore magnetic dipole modes can only be excited in the Si NCs that have the height large enough. This height corresponds to larger than 50-100 nm for silicon.[21]

The electric dipole resonance is due to the polarization of the charges inside the particle due to the electric field of the incoming light. The oscillation of the electric charges induces a magnetic current loop. This mode can be supported in shallow particles, since the magnetic permittivity of cylinder and the surrounding material is 1, and supports the magnetic current loop.

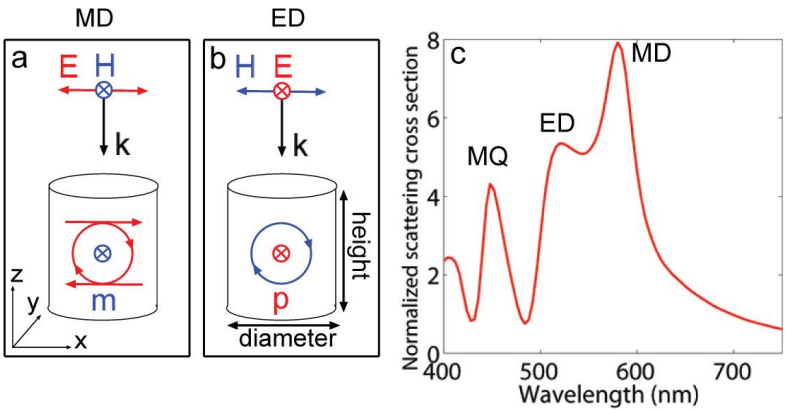

Figure 1-3 (a) magnetic dipole (MD) and (b) electric dipole (ED) modes shown for dielectric nanocylinders. The circulating displacement currents are indicated inside the particle, inducing magnetic and electric dipole moments. (c) The scattering cross sections for the 100nm tall Si NC with diameter of 150 nm, exhibiting MD and ED and magnetic quadruploe (MQ) modes. Reprinted from Polman et. al.[22]

The higher order terms in the Mie extinction cross section define the higher order multipole modes of the resonances. In high dielectric constant nanostructures, depending on their size and geometry, electric and magnetic dipoles, quadrupoles and higher order modes are present. A clever engineering of the structures geometry can make some of these modes to appear in the visible range, which is particularly interesting because it significantly simplifies the optics needed for detection.

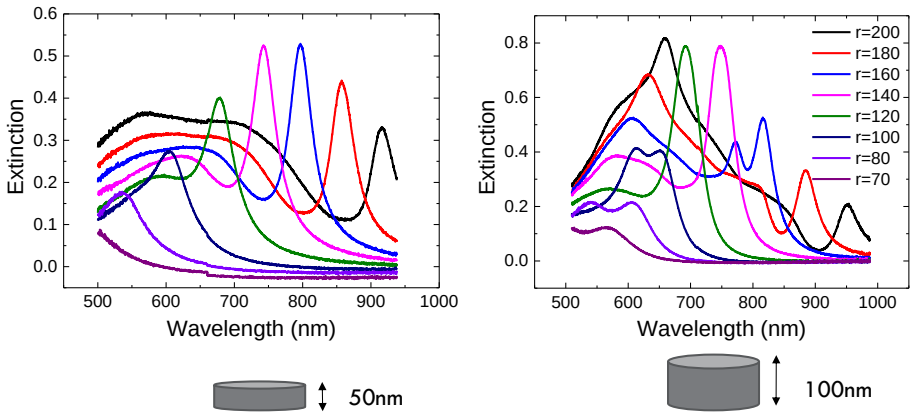

Figure 1-4 Resonances of Si NCs of different radii and heights with fixed interparticle separation $s = 200$ nm in the array.

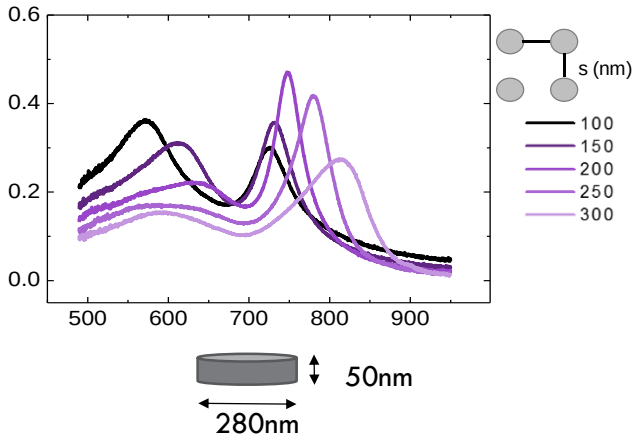

Figure 1-5 Resonances of Si NC arrays of fixed radius (r=140 nm) and height (h=50 nm) with varying interparticle separations.

Since we focus on the arrays of Si nanocylinders (Si NC) in next chapters, where their height and radius are the critical geometrical parameters (Figure 1-4), ensemble geometry properties such as periodicity or interparticle distances are also important (Figure 1-5). It is worth noting that the shallow particles only exhibit electric dipole modes whereas as the height increases, the structures start supporting electric displacement currents resulting in additional magnetic modes in Figure 1-4. There are many valuable reviews and detailed analysis for further information on the optical resonances of dielectric nanodisks and cylinders.[13,21,23,24]

1.2 Sensing with optical nanoresonators

The dependence of the resonances of these optical nanoresonators on the dielectric constant of their surrounding media, enables them to be used as very sensitive sensing tools. They can be used, for example, to sense the refractive index changes in their surrounding media in bulk (bulk refractive index sensitivity, BRIS) or molecule adsorptions onto their surfaces.

The BRIS of a nanostructure is a measure of how much its resonance wavelength will change when the refractive index of its surrounding medium, n, changes[25]:

$$BRIS = \frac{\partial \lambda_{res}}{\partial n} = -\frac{4n}{\left(\frac{\partial \epsilon}{\partial \lambda_{res}}\right)} \tag{7}$$

This can be derived by taking the derivative of the resonance condition $\epsilon(\lambda_{res}) = -2\epsilon_m$.

Having a good BRIS, being a good indicator of the sensing ability of the sensors, does not always necessarily imply good biosensing performance for a sensor. The high BRIS might also result from non-localized electromagnetic field, which would lower the particles ability to detect molecules because it would be highly sensitive to background noises.

The sensitivity of nanoresonators to molecules adsorbing onto their surface is what is crucial for them to be able to be used to gain biologically meaningful information. The molecules adsorbed onto the surface of the nanoresonators can be treated as a uniform coating layer with refractive index n_l. Following the extinction cross section of a coated sphere[14], the molecular sensitivity, S follows as[25]:

$$S = Re\left\{\frac{\partial\lambda_{res}}{\partial n_l}\right\} = -\frac{4n_l}{\left(\frac{\partial\epsilon'}{\partial\lambda_{res}}\right)}\Delta \qquad (8)$$

where Δ is the volume fraction of the adsorbed layer occupying the mode volume of the particle. For a layer of zero thickness $\Delta = 0$ and for a layer that covers the whole mode volume $\Delta = 1$. ϵ' is the real part of the dielectric function $\epsilon = \epsilon' + i\epsilon''$ of the particle. Thus, a good overlap between adsorbates and the modes are crucial for efficient utilization of BRIS for biosensing applications.

The way we utilize the sensitivity of the resonances to the environmental changes is through observing the resonance peak response to these changes. By a home-made transmission spectroscopy set-up collecting the light transmitted from the nanoresonator arrays, we track the extinction peaks of them. We track up-to 32 sensor array positions by scanning the fabricated chip with a galvo.

Tracking the shift of the resonance peak position of these nanostructures is the conventional way of tracking the changes in their surroundings. A Red-shifted peak position corresponds to an increase in the refractive index (RI) of the surrounding medium or to the adsorption of a molecule onto the sensor surface while a blue-shift indicates the opposite, a lowering RI or the desorption of molecules from the sensor surface.

Centroid tracking is a method which has been proposed to improve the performance of these sensors[26] because more pixels from the CCD camera are

involved in this tracking method, compared to the peak tracking which only uses data from a few pixels. The centroid of the resonance is calculated as[26]

$$\lambda_c = \frac{\int_{\lambda_s}^{\lambda_s+s} \lambda\,[E(\lambda) - E_{base}]d\lambda}{\int_{\lambda_s}^{\lambda_s+s} [E(\lambda) - E_{base}]d\lambda}, \tag{9}$$

where the s is the span of the wavelength range $[\lambda_s, \lambda_s + s]$ to be considered for the centroid calculation, E_{base} is the value of the extinction at λ_s and $\lambda_s + s$. Figure 1-6a shows these parameters and the centroid position on the extinction spectrum of the gold nanorod arrays that are used for sensing in Chapter 3. In Figure 1-6b a comparison of peak and centroid tracking for LSPR sensors (gold nanorod arrays) is presented for an antibody binding to the sensor surface. The sensor preparation, a baseline measurement with buffer solution, the antibody binding steps, followed by washing and blocking steps can all be observed as the peak and centroid shift. It becomes clear however that the the signal to noise ratio of the centroid shift is higher than thatthe one of the peak shift, proving the superiority of the centroid tracking method for this application. This is why this is the method used for the sensing experiments in this thesis unless otherwise specified.

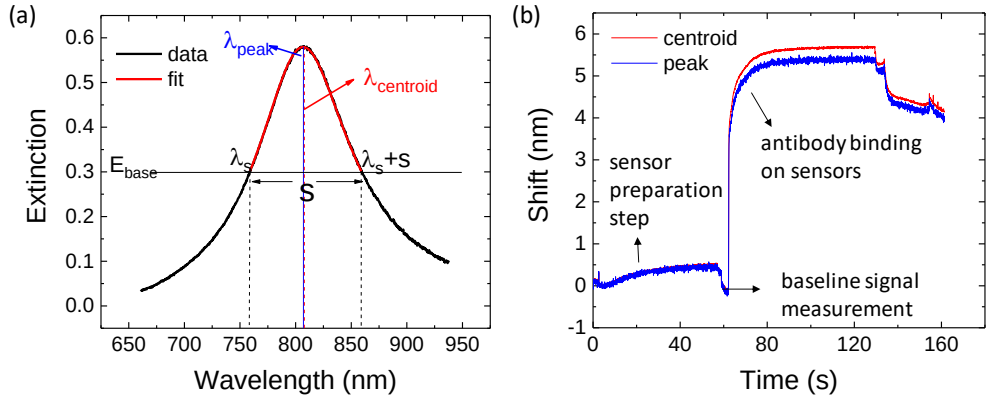

Figure 1-6 Peak vs centroid tracking. (a) Parameters for centroid tracking method shown on an extinction spectrum of a gold nanorod array. (b) Comparison of the centroid and peak shifts calculated for an antibody binding event on the same LSPR sensor array as in (a)

1.2.1 Sensing with metallic nanoresonators (LSPR)

Surface plasmon resonances (SPRs) of thin films are commonly used for sensing RI changes and detecting biomolecules. It is a well explored and commercialized concept.[27] With the advancement of controlled fabrication and manipulation of the metallic nanostructures, LSPR sensing applications have attracted attention since 2000s.[28–30] The metallic nanoparticles, especially gold and silver are extensively used to sense both bulk RI and molecular binding events. Nanoparticles in solution or on substrate are used for detection of biomolecules with very low limits of detection.[31–37] Very high sensitivities can be reached by engineering the shape, size and organization of the nanoresonators to tune the field confinement around the nanoresonators for optimum mode-analyte overlap. The ability to directly couple to LSPRs as opposed to complex excitation setups for SPR, is highly beneficial in building devices that can be simpler and more compact. In Chapter 3, we discuss in detail about lab-on-chip integrated LSPR based sensors, and present our multiplexed LSPR based microfluidic platform.

1.2.2 Sensing with dielectric nanoresonators

Advancing fabrication and simulation methods paved the way to new developments in the field of all-dielectric nanophotonics, leading scientists and engineers to explore different applications of the resonances of high refractive index dielectric nanoresonators. Among the applications, biosensing is one that has not yet been explored as much as its LSPR counterparts. There are very recent theoretical and experimental demonstrations of the refractive index sensing with Mie resonance modes of dielectric nanoparticles, exploring different behaviors of electric and magnetic multipole modes under changing surrounding medium.[17,18,20,38–40]

By the time this thesis project started, there was a gap in the literature on using the resonances of dielectric nanostructures for clinically relevant biosensing applications. At the time of writing this thesis dissertation, there are few publications that focus on biomolecule detection with these resonance modes. A part of our work here focuses on filling this gap, bridging the field of all-dielectric nanophotonics with on-chip biosensing applications that are clinically relevant and explore the compatibility of those fields for meaningful POC product development. Chapters 4 and 5 focus on the works completed with that goal in mind also presenting a brief comparison between LSPR sensing and dielectric nanoresonators based sensing.

1.3 Microfluidics for Lab-on-chip biosensing platforms

In order to perform controlled sensing measurements with high throughput and in a multiplexed manner, we integrate optical nanoresonators with microfluidic channel networks. Microfluidic platforms allow for easy delivery of different samples (biomolecules) to different sensors and run parallel measurements. The micrometers scale of channel sizes for sample delivery, meet the need for measuring with nanostructure arrays of the similar dimensions.

Microfluidics refers to the control and manipulation of fluid flows inside channels with diameter dimensions in the micrometer-scale. At such a small scale, the observed flow is laminar, in contrast to the turbulent flows existing at the macro-scale where fluids move more chaotically. In the laminar flow regime, the fluid flows in parallel layers with no perpendicular cross-currents or swirls (Figure 1-7).

The Reynolds number (Re) is the dimensionless parameter that indicates whether the fluid flow inside a channel is laminar or turbulent[41]:

$$Re = \frac{inertial\ forces}{viscous\ forces} = \frac{v2d_h p}{\mu v} = \frac{\rho v d_h}{\mu} \qquad (10)$$

where ρ is the density, v is the velocity and μ is the viscosity of the fluid, and D_h is the hydraulic diameter of the channel ($d_h = 4A/P_w$, where A is the cross sectional area of the channel and P_w is the wetted perimeter). Re values below 2000 define the laminar regime. For channel diameters around 100 μm or smaller, and a low rate of fluid flow 1 cm/s, laminarity is ensured.[42]

In the laminar flow regime, the flow velocity in the middle of the channel is very high, compared to very low flow velocities (ideally zero) at the walls of the channel. For sensing applications, the sensors are placed on one wall of the channel, meaning the transport of target molecules in the sample to the sensors is dominated by diffusion since there is no advection towards the channel walls.

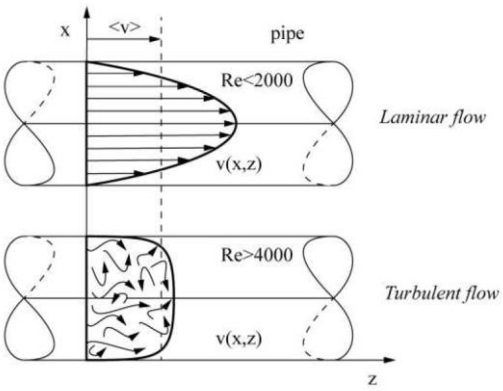

Figure 1-7 The flow speed profile in a pipe for laminar and turbulent flow conditions. (reprinted from O. Reynolds[43]).

The fluid flow rate in microfluidic channels is analogous to that of the electric circuits. A channel's width and length determines its hydraulic resistance, just like the electric resistance in electric circuits. The pressure applied is analogous to voltage and the flow rate is to current. This analogy helps in designing the necessary microfluidic channel network for a specific application.

For our sensing platforms, we employ microfluidics to deliver fluids to different sensing sites simultaneously, in a highly controlled manner with no cross contamination. To have full control over the multiple reagents and analytes needed for these sensing applications, we make use of microfluidic chips made of two-layer PDMS (poly-dimethilsiloxane) channel networks. PDMS is a polymer that is commonly used to develop lab-on-a-chip applications due to its optical transparency, biocompatibility, elasticity and easy fabricability. Although not the ideal material for mass fabrication, it is quite attractive for laboratory tests, because it is suited to cheap and easy design iterations. More importantly, its elasticity enable the development of microfluidic chips with micro-valves that can be fabricated by multi-layer soft lithography.

In these two-layer PDMS microfluidic chip designs, the control layer channel network overlaps with the flow layer channel network at specific points. Only a thin PDMS layer separates the control and flow layers creating a micromechanical valve in this position. When the control layer channel that is filled with air or water is pressurized, the actuated elastic membrane collapses into the flow layer, blocking the flow of the liquid inside the channel.[44] Flow and control layers can be arranged in two ways, allowing for push-up or push-down type of valves as shown in Figure 1-8. In the state-of-the-art microfluidic platforms, the challenges such as mixing, sorting, generating gradients and molecular transport are tackled by

researchers in numerous creative ways and it continues to be an interesting field for engineers and biologists.[44–49]

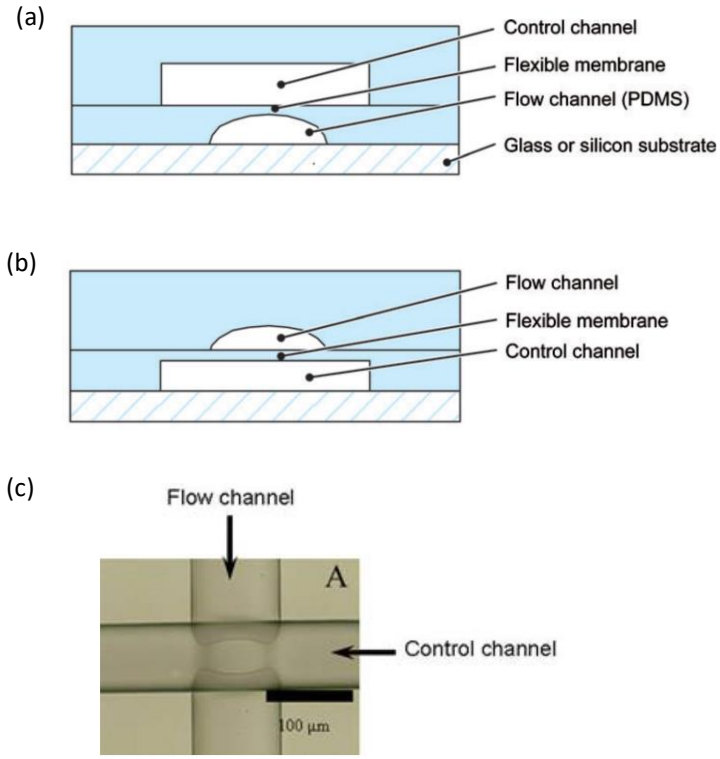

Figure 1-8 Micro-mechanical valves in two-layer PDMS chips. (a) Push-down and (b) push-up valve architecture (reprinted from Melin et. al.[44]). (c) Picture of a valve in a closed state (reprinted from Stanford Microfluidics Foundry webpage[50]).

In our sensing platforms we rely on the push-down design, in order to integrate the optical sensor arrays with the flow layer of the chip (see Chapter 2 for further details). We aim for simultaneous and parallel detection of different biomolecules or samples on a single microfluidic chip with multiple nanosensor arrays located in different channels of the chip. For target molecule detection, we utilize immunoassays (see next section). Therefore, it is important to design channel networks that can introduce common reagents into multiple experimental channels simultaneously, as well as enabling individual access to these channels for measuring different samples in parallel. This is satisfied with a special design of channels, inlets and outlets of these channels, and control valves that regulate the flow on those channels to perform the steps of immunoassays and sensor preparation.

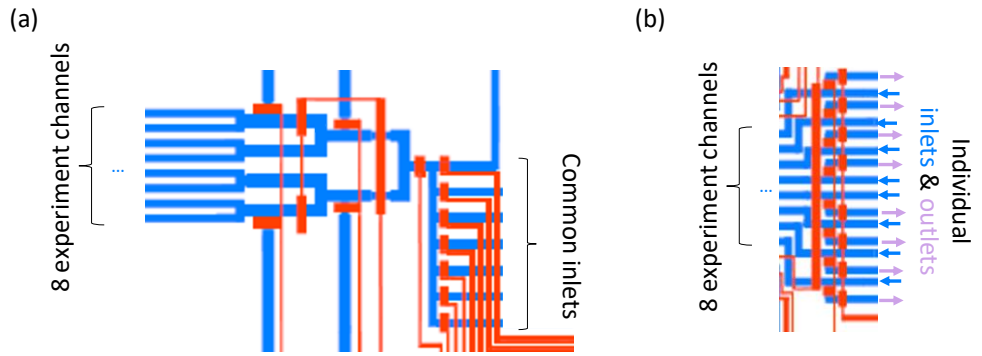

Figure 1-9 Microfluidic flow (blue) and control (red) channel architecture for (a) common treatment of all experimental channels and (b) individual treatment of each experiment channels.

Figure 1-9a shows the architecture that allows common reagents to be introduced into all experimental channels simultaneously with the same flow rate. To allow this, the channels need to have the ''tree'' structure, equally dividing the laminar flow of the reagent/sample from the common inlets into the experiment channels. By opening and closing the valves, which are the red areas intersecting the blue flow channels, the flow from different inlets can be directed to the channels. Similarly Figure 1-9b shows the architecture for individual channel treatment, where the inlets and outlets are separately connected to each channel. Those individual outlets are used when the channels are treated with common inlets in our architecture.

The full layouts of the microfluidic channel networks used in experiments will be explained in Chapters 3 and 4, as for different experiments, slightly different designs are utilized.

1.4 Surface Chemistry

Surface chemistry deals with the chemical changes at the interface of two materials/environments. We need to employ surface chemistry for multiple reasons in our platforms. One is to bind the PDMS chips onto the sensor substrates for performing sensing assays, and the other is to functionalize the sensor surface so that the target molecules can be attached to the surface of the sensors for detection.

1.4.1 Chip binding

Binding the sensor substrates to the PDMS chips requires modifications of both material surfaces. Prior to this, the PDMS chip layers (control and flow) need to be bound covalently so that the chip can endure the pressures that will applied during the measurements.

Two PDMS layers form a bond when the surface methyl groups are oxidized with oxygen or UV ozone plasma. When both oxidized layers are brought into contact, covalent bonding occurs in several minutes.

Binding the glass substrates with PDMS chips relies on the same method. Glass and PDMS are oxidized by the oxygen plasma and brought into contact for covalent binding. Some applications that require forming organic self-assembled monolayers (SAM) on the sensor surface prior to chip assembly pose a crucial problem, as the plasma activation of the substrate would lead to destruction of the SAM. Therefore, in those cases, for the chip assembly, only the PDMS surface is oxidized and brought to pressure contact with the substrate at lower temperature. This results in slightly weaker but sufficiently strong binding for the sensing experiments.

1.4.2 Sensor functionalization

To detect biomolecules, we run sandwich immunoassays on the optical nanoresonators. The key step is to immobilize antibodies on the sensors, without non-specific binding. In some cases, the passive adsorption of molecules onto the sensor surface is not strong enough or even possible, therefore, the functionalization of the sensor surface is necessary for running a robust immunoassay. The SAM of mercaptoundecanoic acid (MUA) is used on gold sensors to act as a link between sensors and the antibodies. The activation of carboxylic acid groups of MUA with EDC (carbodiimide) – NHS (N-hydrocarboxysuccinimide) reaction is used for immobilizing antibodies onto the MUA (Figure 1-10a). Once the antibodies are immobilized, before the target molecule is introduced into the environment, the active MUA sites that are uncovered by antibodies are blocked by ethanolamine (Figure 1-10b). This method is commonly used in plasmonic sensing applications, therefore the protocols are well established in the literature[51–55], and only need to be adapted to our sensors.

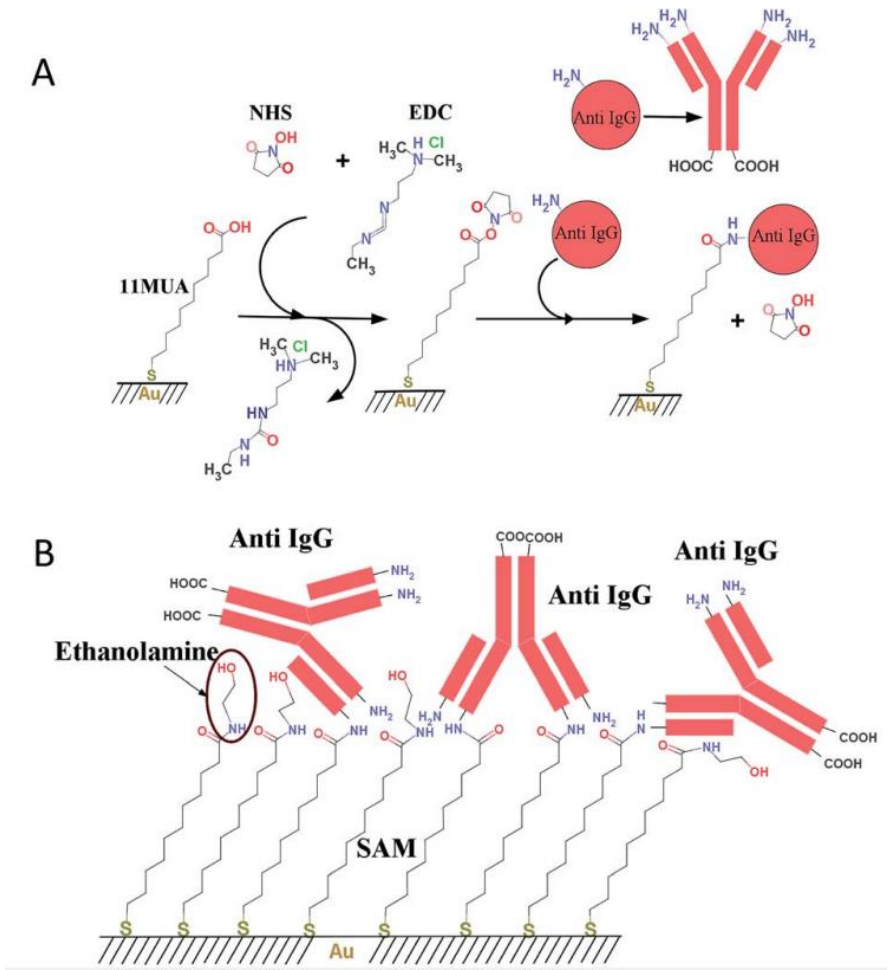

Figure 1-10 Surface fucntionalization. (a) EDC-NHS chemistry on MUA for antibody immobilization on gold. (b) Ethanolamine blocking of the active MUA sites after antibody immobilization. (reprinted from Bhadra et. al.[52])

After antibody immobilization and ethanolamine blocking steps, the sandwich immunoassay can be performed on the sensors, described in detail in Chapter 2.

2 METHODS FOR ON-CHIP BIOSENSING WITH OPTICAL-NANORESONATORS

The experimental methods used in the measurements consists of combination of multiple fields and technologies.

The work flow of a regular on-chip sensing experiment consists of (i) fabricating the desired type and design of NRs on a glass substrate, (ii) fabricating the microfluidic chip with desired channel networks, (iii) preparing the NR sensor surface for sensing experiments, (iv) assembling the sensors with the microfluidic chip and (v) further chemical preparation of the sensors and (vi) finally the biomolecular sensing steps followed by (vii) data processing. Multiple manufacturing steps are usually prone to failing, due to incompatibilities between materials, fabrication steps and the complexity of the procedures. Many steps of fabrication and preparation procedures have to be followed and combined carefully in order to achieve a successful sensing measurement. The average time of fabrication of a biosensing platform we focused on in the scope of this thesis is between 2 days to 4 days.

The most crucial aspect for developing a reliable point-of-care diagnostic device development is reproducibility. For a platform that consists of multiple fabrication steps and materials, it is very important to follow proper fabrication and preparation steps in order to perform successful experiments and obtain reliable results.

In this chapter, the methods used throughout the thesis will be described in detail. The fabrication of both gold and silicon nanoresonators (NR), preparation of the NRs for biosensing experiments, fabrication of microfluidic chips and the integration of the chips with sensors will be explained. In the last section, the details of the sensing procedure on-chip will be given.

2.1 Fabrication of Nanoresonators for Biosensing

Nanoresonators (NRs) are the structures that have at least one dimension that ranges between 1-100 nm. To fabricate the structures in highly controlled and reproducible ways, highly controlled environments such as cleanrooms are needed, equipped with machines for fabrication and characterization of those structures. The nanostructures can be fabricated by top-down or bottom-up techniques, where the former constitutes of the fabrication of the nanostructures from a larger block of material and the latter is based on fabrication of nanostructures using atoms or molecules as the building blocks and bringing them together to form the desired structure.[56] The top-down methods are used for the NRs employed in the projects followed in next chapters.

Au and Si NR based sensing platforms are in the scope of this thesis. For the LSPR sensing platform that is developed and presented in chapter 3, gold nanorod arrays are employed, whereas for the Si NR based platforms that are presented in chapter 4, Si nanocylinder (Si-NC) arrays are used. Two types of Si-NC arrays are fabricated: periodic and semi-random. The different fabrication procedures are described in following sections.

E-beam lithography is a highly controllable method, enabling the fabrication of highly reproducible samples with high resolution in feature size and high accuracy in positioning and aligning.[57] It also provides the ability to design and fabricate different nanostructures in parallel with desired optical and mechanical properties. Therefore, we used e-beam lithography for fabricating sensors consisting of periodic and highly ordered structures.

Despite its advantages, e-beam lithography is not a cost-effective method and it also suffers from high exposure times for patterning a small area of the sample. Colloidal lithography techniques are implemented to fabricate simpler arrays in a large-scale and cheap manner.[58] When periodicity is not crucial colloidal lithography is a more suited fabrication method because it is significantly more efficient. Therefore, we used a colloidal lithography method customized in our lab, in order to fabricate randomly distributed Si-NC arrays for the part of the results presented in Chapter 5.

2.1.1 Fabrication of gold NRs

The fabrication procedure of gold nanorod arrays is based on electron beam (e-beam) lithography with negative resist, followed by a reactive ion etching (RIE)

process. Figure 2-1 shows the fabrication procedure for gold nanorod arrays. The steps are as follows:

Cleaning: The glass substrate (PGO MEMPAX) of 25x25 mm with thickness of 0.4 mm is cleaned with soap and water, followed by aceton and IPA rinsing.

Metallization: The cleaned substrate is coated with 2 nm of Ti layer for adhesion, followed by 50 nm of Au layer in the Lesker Lab18 evaporator with the coating rate of 1 A/s.

Resist coating: The metallized sample is then spin coated with negative e-beam resist ARN-7500-08 at 8000 rpm and baked at 85 C for 1 min.

E-beam writing: In the negative resist e-beam lithography, the unexposed regions of the resist are removed by developer.

The e-beam exposure of the desired pattern is realized by CRESTEC CABL writer. The pattern design is prepared in the custom software of the CRESTEC CABL. The optimization of parameters of exposure such as exposure time (dose), the current, etc. are crucial for obtaining high quality structures and it is important to test and fix those parameters by running test samples. The exposure time for one sample is around 4 hours regarding the number and the size of arrays needed to perform the experiments that will be described in Chapter 3.

Developing: The exposed sample is developed in 1:4 AR-300-47 developer for 3 minutes and rinsed with water and dried with N_2.

The sample is baked at 85 C for 1 min to obtain resist contrast for RIE step.

RIE: The gold layer is etched using directional argon plasma at the rate of 15 nm/sec using the ARN resist as etch mask.

Cleaning: The mask is then cleaned by either O_2 plasma or dipping the substrate into 1:3 piranha solution (Hydrogen peroxide: Sulfuric acid) for 10 seconds. The latter worked better for cleaning the sensor surface, eventhough requires careful handling of the acid and longer than 10 sec washing causes the Ti layer to be etched away, therefore the dissociation of the gold nanorodos from the substrate surface.

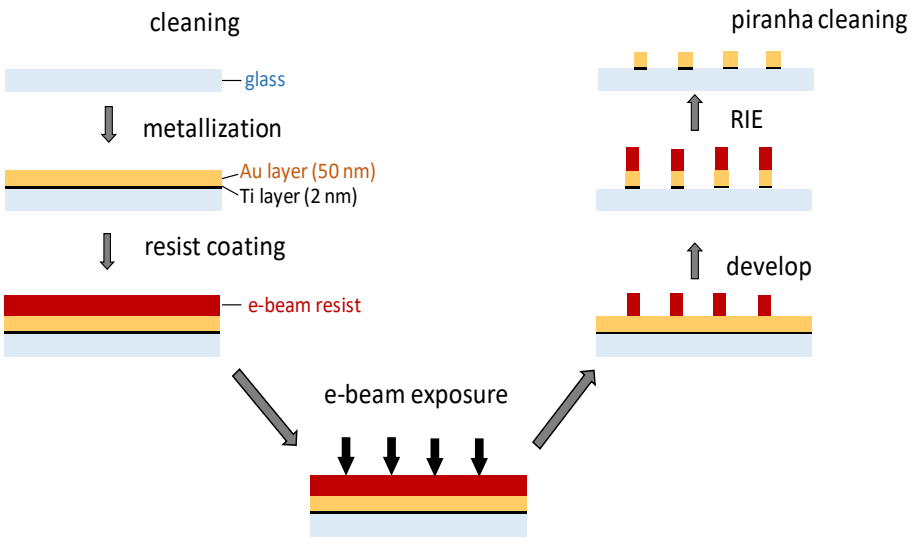

Figure 2-1 Fabrication procedure of gold nanostructures with negative e-beam resist.

Following the cleaning of the substrate, the gold sensor surface is functionalized as will be described later in this chapter.

2.1.2 Fabrication of silicon sensors

periodic Si nanodisk arrays

Periodic Si nanodisk arrays were fabricated using standard e-beam lithography (EBL) followed by a reactive ion etching (RIE) step very similar to the gold nanorod fabrication described in previous section. We used the silicon-coated quartz substrates (Siegert Wafers) of 25x25 mm. The resist coating, e-beam writing, developing steps are kept the same as in Au NR fabrication. After that, the nanodisk patterns were transferred to the silicon layer by RIE using SF6 and C4F8 gases for etching. After the RIE, the substrate cleaning is done in the same way as described for Au NRs.

semi-randomly distributed Si nanocylinder (Si-NC) arrays

For the fabrication of the semi-randomly distributed Si-NCs with no long-range order but with a typical interparticle distance the fabrication procedure is as follows:

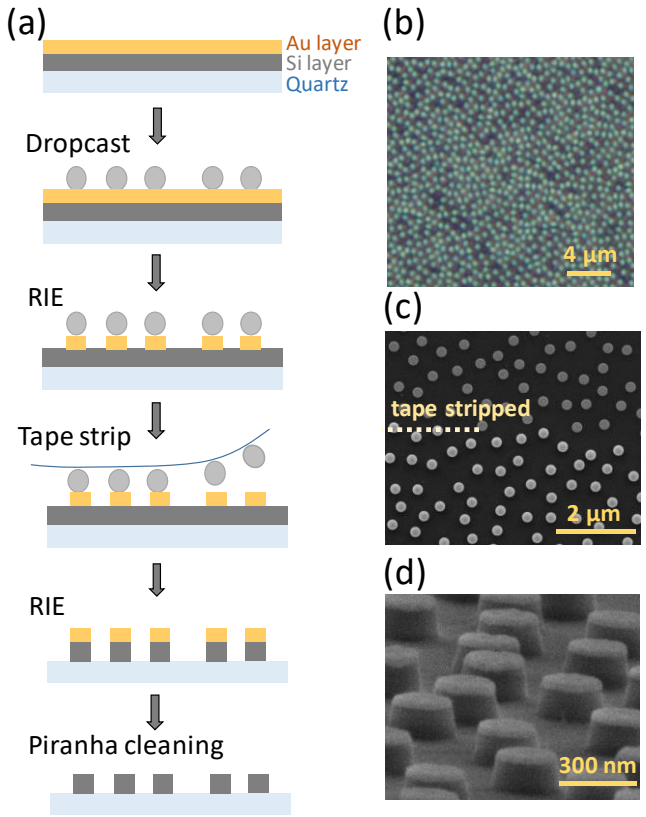

Figure 2-2: Fabrication steps of randomly distributed silicon nanocylinder (Si-NC) arrays. (a) Fabrication steps of Si-NC arrays. (b) Dark field microscopy image of the sulfate latex beads dropcasted on the gold layer. (c) The SEM image of the substrate after the tape stripping step showing the stripped regions with gold nanodisks (above the dashed line) and unstripped regions with the beads on top of gold nanodisks (below the dashed line). (d) The SEM image of the substrate after etching the Silicon layer by RIE, using the gold disks as etching mask. The gold mask is seen on the Si-NCs.

Cleaning: The Si-coated quartz substrates of 25x25 mm that are purchased from Siegert Wafer, GmbH were cleaned by aceton and IPA rinsing.

Metallization: After cleaning the substrates, 2nm of Ti layer is coated as an adhesion layer on silicon and then 50 nm of Au layer is evaporated on the thin Ti layer.

Bead dropcasting: Then the sample is treated with O_2 plasma for 5 seconds at 100 Watts (200 ml/min flow). After the plasma, the sample is incubated for 1 minute in 0.2% Poly-diallyl dimethylammonium chloride (PDDA) solution for surface activation and the surface becomes positively charged, and then washed with water and dried with N_2. After the surface activation step, the sample becomes ready for the dropcasting the Sulfate Latex beads (Thermofisher, S37491, 0.2 µm)

which are stabilized by sulfate charges (negatively charged). 0.2% w/v solution of beads is drocasted on the substrate, covering the whole surface, and after 1 minute, the surface was quickly rinsed with water and dried with N_2. For our sensing application, we removed the beads around the edges of the sample, using a scotch tape, leaving the beads only in the center of the substrate, where we will then scan for sensing. The whole sample surface with beads can be patterned in different ways mentioned in the main text. Figure 2-2b shows the dark field microscopy image of the beads dropcasted on the gold layer.

Gold mask etching by RIE: The Au layer on the sample, masked by the beads, is then etched by Ar gas (40 sccm) for 3 min 20 s.

Tape stripping: The beads are then removed by tape stripping from over the Au nanodisks. Figure 2-2c shows the SEM image of the tape stripped substrate after gold mask etching.

Si etching by RIE: Au nanodisks are used as a mask for etching Si layer in RIE with C_4F_8 (70sccm) and SF_6 (45sccm) gases at a rate of 0.27 nm/s. Figure 2-2d shows the SEM image of the sample after 130 nm Si etching step, where the gold mask layer on the Si-NCs are visible.

Removal of gold mask and cleaning: Finally, the sample is washed inside piranha solution, which lifts off the Au layer by etching the Ti layer below and cleans the silicon nanodisk surface.

The final radius and the density of the silicon nanodisks are 140 nm and 2.1 disks/1μm^2.

With this EBL-free method, the whole sample area can be patterned with nanostructures simultaneously without altering the fabrication time or the cost. The areas on the substrate to be patterned can be selected by tape stripping the beads away before using them as an etch mask. More precise bead stripping method is described by Acimovic et. al for patterning the sample surface with precision of few micrometers by using a homemade PDMS stripping tape.[33] For our sensing device, we tape stripped the edges of the sample, leaving the beads at the center of the substrate.

2.1.3 Sensor preparation and surface chemistry

In the scope of this thesis, the on-chip sensing experiments are all based on sandwich immunoassay format. For selective and reliable biomolecule detection, the surface of the sensors need to be coated by capture antibodies that will recognize the target biomolecule. In order to selectively immobilize the capture antibodies on the sensor surface, sensors are functionalized as described below.

Gold sensors

The surface of the gold sensors are coated with self-assembled monolayer (SAM) of mercaptoundecanoic acid (MUA), in order to have carboxyl groups on gold surface to immobilize the capture antibodies with their amine groups.[54] The fabricated gold nanorod arrays are incubated in 2.5 mM MUA in ethanol solution at room temperature for 18 hours (overnight). Then rinsed by ethanol and dried with N_2.

Silicon sensors

In this thesis, we have not focused on developing a specific surface treatment for Si sensors. All the experiments rely on the passive adsorption of the biomolecules onto the Si surface. According to the preliminary tests and results that we obtained, the passive adsorption of the antibodies on Si sensor surface provides a strong attachment to the surface and eliminates the additional surface activation steps. The specificity and the sensing performance of the sensors are discussed in Chapter 4.

2.2 Microfluidic chip fabrication

The PDMS microfluidic chips consisting of two layers are fabricated by UV photolithography followed by multilayer soft lithography[46] based on molding the uncured PDMS by a photoresist-on-silicon wafer mold fabricated by a UV lithography. The fabrication workflow therefore briefly consists of (i) designing the channel networks for control and flow layers of the chip, (ii) printing the designs onto a transparency mask, (iii) transferring the designs onto silicon wafers by UV lithography, (iv) using the fabricated control and flow molds for PDMS casting, (v) curing the PDMS, (vi) stripping the control layer and punching the holes to access the control channels, (vii) aligning and bonding the control and flow layers, (viii) punching the holes to access the flow layer. After that, the PDMS chip is ready to be assembled with the substrate with sensors.

2.2.1 UV photolithography for mold fabrication

The master molds for flow and control layer are fabricated through standard UV photolithography in the cleanroom using AZ9260 negative photoresist and Quintel Q4000 mask aligner. The clean Si wafers are spin coated with AZ9260 at 2000 rpm. Flow mold is coated with single layer while the control mold is coated double layer of AZ9260 for obtaining higher channels. The transparency mask with respective flow and control layer designs are used for UV lithography and the wafers are developed in MIF860 developer. The flow layer mold is post-baked at 120 C oven for 30 minutes. The post-bake makes the channel profile round, which is crucial for push-down valves, in order to obtain full closure of the valves. The control layer is left unbaked as the rectangular channel profile is desired. The final thicknesses of the flow and control layer resist are around 10 µm and 24 µm respectively.

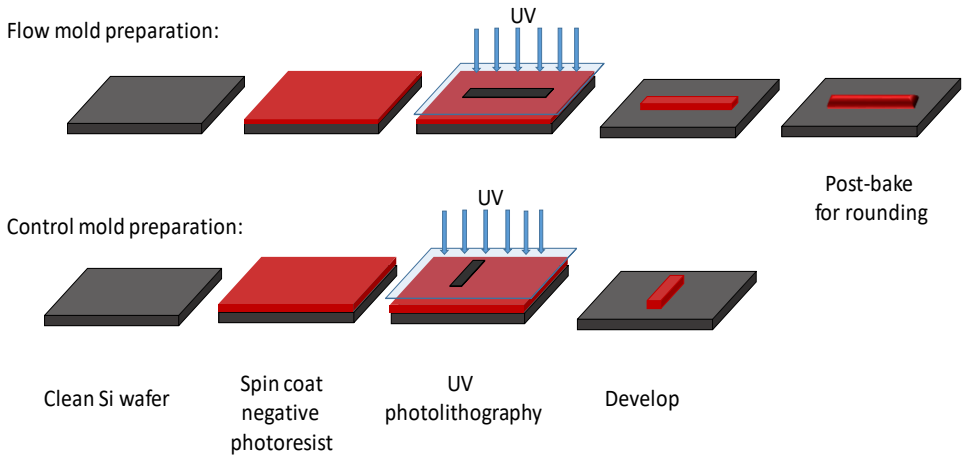

Figure 2-3 Fabrication of the molds for microfluidics photolithography

Once the master molds are fabricated for a set design, they can be reused for fabrication PDMS chip batches.

For the platforms developed in this thesis, 4 inch silicon wafers are prepared as master molds, containing 4 copies of the same chip design. Therefore each batch fabrication lead to 4 PDMS chips, saving time and effort.

2.2.2 Multilayer Soft Lithography for PDMS microfluidics

Multilayer soft lithography is used for the fabrication of the PDMS chips. Uncured PDMS is casted on the master molds in order to transfer the channel design onto the polymer.

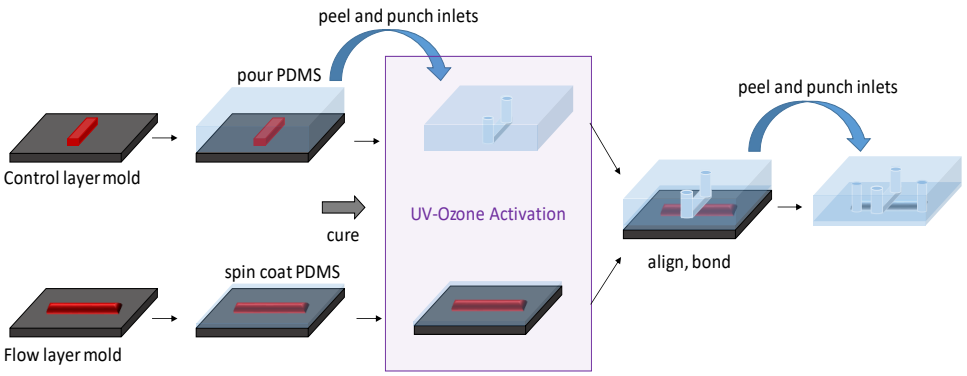

Figure 2-4 PDMS chip fabrication by multilayer soft lithography.

PDMS polymer mixture with its curing agent is prepared for control and flow layer fabrication with the ratio of 1:10 and 1:5. The reason for high curing agent ratio for flow layer is that the stiffness of the layer helps providing more robust valves. The Si wafer molds are treated with TMCS (trimethylchlorosilane) vapor prior to each use to prevent from adhesion of PDMS on the mold. PDMS is poured onto the control layer mold in a petri dish up to a thickness of 0.5 mm whereas it is spin coated onto the flow layer mold with 2200 rpm for thickness of around 20 µm. Then the molds with PDMS is baked at 80C for 1h for curing and the cured PDMS on control layer is peeled and holes are punched for accessing the control channels. The flow layer is left on the mold and both PDMS parts are treated with UV ozone plasma for activation for 3 mins. They are then aligned and bound using a stereo microscope and baked for 10 h at 80C for complete binding and curing. Then the multilayer PDMS chip is peeled off from the flow layer mold and the inlets to the flow channels are punched. At this stage the PDMS chip can be stored until integration with the sensors which is described in the next section.

2.3 LOC Assembly

The LOC assembly is the step that integrates substrates with the fabricated and prepared sensors with the PDMS chips. The bond between substrate and the PDMS chip needs to be very strong in order to operate the chip with required high pressures for valve control. This can be a non-trivial challenge as the conventional methods for covalently binding PDMS to glass involves O_2 plasma activation of both materials. The organic molecules such as SAM of MUA on the sensors are very sensitive to this treatment. Another challenge is the high temperatures used for baking the assembled chip for covalent bonding.

For the chips presented in this thesis, the PDMS is treated with UV Ozone plasma for 3 minutes and quickly aligned and pressed on the substrate with sensors prepared as described in section 2.1.3. The assembled chip is baked at 50 C for 10 hours. No significant effect of baking at 50C on the MUA was observed in the sensing experiments.

2.4 Opto-fluidic setup

We have used an opto-fluidic setup for measuring and tracking the resonances of the sensor arrays and controlling the sample and reagent flow on the LOC devices by manipulating the micromechanical valves on them. This setup consists of the optical part and the fluidic part that will be explained in this section.

The optical setup was built in our group, before I started my PhD studies. It is a home-made optical microscope in bright-field transmission that consists of a VIS-NIR light source (Olympus) to excite the resonances of the sensor arrays, a galvo to scan different arrays for parallel measurements, and an ANDOR spectrometer to detect the resonances in the transmitted light (Figure 2-5a). A broad-band linear polarizer, a set of irises and condenser lens is used to focus the incident light on the nanorod arrays. The transmitted light is directed toward the galvo mirror, and focused onto the fiber, that guides it to the spectrometer. One camera with low magnification is incorporated to image the full layout of the microfluidic device and another camera with high magnification was used to image the area with sensing regions on the device. A home-developed Labview interface is used to control the spectrometer and the galvo scanning system (Figure 2-5b). The setup measures the extinction peak and centroid positions at the sampling rate of 10 Hz. The sampling rate is limited by the spectrometer's read-out time. The software tracks up to 32 sensor arrays on the chip in real time and plots the corresponding resonance shifts of simultaneously tracked sensor arrays in parallel. The software also stores the data offline and more precise data processing (see Section 2.7).

(a) (b)

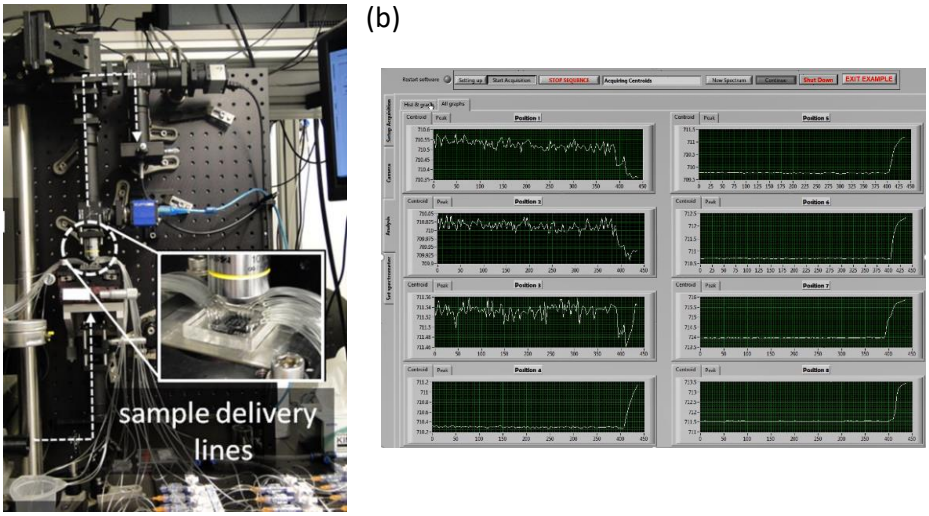

Figure 2-5 Optical setup and control software. (a) the optical setup with the microfluidic device in the close-up.(Modified from Acimovic et. al.[34]) (b) the screenshot from the extinction tracking software. The real time resonance shift plots for 8 different sensor arrays on the chip.

The automated fluidic control setup was built in the scope of my PhD thesis. The fluid control on the chip is regulated by a set of electronic pneumatic valves (Pneumadyne) that are pushing water into the control channels when switched on. The pressurized control channel collapses on the flow channel blocking the fluid flow, as described in the previous chapter.

The micromechanical valves connected to electronic valves are controlled by a home-made Matlab GUI (Figure 2-6) in order to run an automated sandwich assay. Figure 2-6a shows the control setup consisting of solenoid valves from Pneumadyne, controlled by a controller box (home-made). The electronic valves are connected to the chip through tygon tubings that are filled with water, pushing the water into the control channels on chip when pressurized. The closing pressure of a micromechanical valves are 15-30 psi. The electronic valves are controlled by the matlab GUI shown in Figure 2-6b, which allows the switching the valves on and off by clicking on the chip layout map, or running automated and timed scripts for the steps of the sandwich assay measurement. This enables the full automation of measurements, with the flexibility to interfere and manipulate the measurement if needed.

(a) (b)

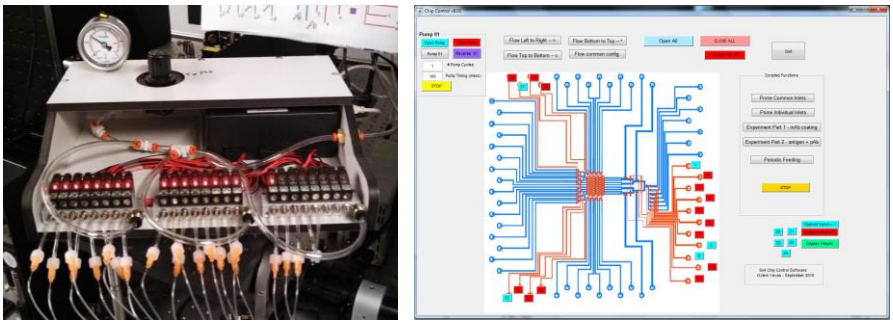

Figure 2-6 The valve control setup and software. (a) electronic solenoid valves (Pneumadyne) are connected to the chip through tygon tubing filled with water. The pressure regulator is used to control the pressure inside the control channels. (b) The custom home-made software (Matlab) to control the electronic valves. The buttons on the chip map can be clicked to turn the valves on and off. There are also embedded script functions to run a part or the whole of the sandwich assay on the chip.

The samples are connected to the flow layer with tygon tubings that are connected to a nitrogen flow at a constant pressure of 3 psi. This allows for the sample to flow into the channels when the control valves are opened.

2.5 Immunoassays for on-chip biosensing

As described in the first chapter, the sensing applications in this thesis mainly use sandwich assay type of immunoassays. All the measurements, except for specifically stated ELISA measurements in Chapter 3, take place on chip. The microfluidic channels are used to control the flow of reagents on specific sensing sites. The details of the full microfluidic chip designs and experiments will be discussed in next chapters, while in this section the focus will be on the sandwich immunoassay specifics.

In the sandwich assay, the capture antibody, immobilized on the sensor surface, specifically captures the target marker. The resonance response for the small target molecule is typically small and the resolution between different concentrations of the marker is not high enough to obtain a reliable sensing signal. Therefore, an amplification antibody that also recognizes and binds to the target biomolecule is used for signal amplification. In this section, the details of the immunochemistry used for the sensing with both LSPR and silicon nanoresonator sensors are described.

2.5.1 Cancer marker detection with Au NR sensors

In order to immobilize the capture antibodies on the sensor surface coated with MUA, EDC/NHS chemistry is used to prepare amine-reactive esters of carboxylate groups. EDC/NHS reaction takes place in 45 minutes in MES buffer. Right after EDC/NHS reaction, the capture antibodies in 10 mM phosphate buffer (PB) are introduced into the channels for binding on the sensor surface. Once the sensor surface is coated with capture antibodies, the LSPR centroid shift signal saturates. Depending on the concentration of the antibody solution in PB, the saturation time changes slightly between 10 and 30 minutes. For most of the measurements presented in this thesis, the capture antibodies are flown in the channels for 60 minutes unless otherwise is specified.

Following the immobilization of the capture antibodies on the specific detection sites on the sensors by the help of microfluidics, to prevent non-specific binding and for the blocking of unreacted NHS-ester groups on the sensors are blocked with ethanolamine solution in PB for 10 minutes. Next, the cocktail of markers prepared in PBS-BSA buffer or 100% unfiltered human serum (Sigma Aldrich) are introduced to the detection sites for an hour, each having different concentrations, in order to obtain calibration curves. In the case of multiplexed detection of multiple markers, each marker is captured by their specific antibody, giving LSPR shifts on the corresponding detection sites. Finally, the amplification antibodies in PBS with 1% BSA with PH of 7.4 to match the human serum PH are introduced through the channels, in order to amplify the LSPR shift.

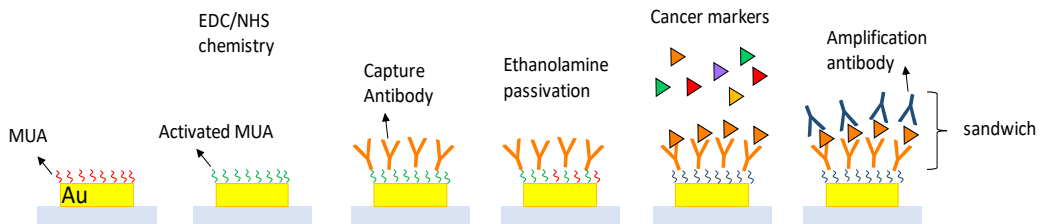

Figure 2-7 Sandwich assay protocol on gold sensor surface.

2.5.2 Cancer marker detection with Si NR sensors

For the specific detection of the target protein (prostate specific antigen, PSA) we formed a layer of capture antibody on the sensor surface. The sensors were first flushed with 10 mM phosphate buffer (PB) in order to have a base for tracking the

shifts. The monoclonal antibody (mAb) (BiosPacific, A45160) for PSA was introduced to the channels in 10 mM PB through a common inlet so that the solution flowed through all the channels simultaneously and all the sensors were coated with the capture antibody. Once the capture antibody layer was formed, the resonance shift signal saturated and the channels were then washed with PB shortly to remove the excess unbound antibodies. The signal saturated after only 15 mins after 150 µg/ml mAb solution was introduced to the sensors. The binding kinetics and the saturation time depend on the mAb concentration used.

For the proof of concept experiments we have measured the PSA calibration curve in phosphate buffer saline (PBS) with 1% bovine serum albumin (BSA). The BSA was added to the PBS as a blocking agent to prevent the unspecific binding and also to mimic the human serum proteins in this preliminary measurement. The 7 PSA calibration concentrations were prepared and introduced to different sensors through individual inlets of each channel. An extra channel was used as a control channel with no PSA added in the buffer.

For the PSA calibration curve measurements in human serum, the calibration concentrations were similarly prepared in 50% diluted human serum instead of PBS with BSA. For the experiment presented in the Fig. 6, the capture antibody concentration used was 300 µg/ml.

For the target proteins that are small in size compared to antibodies, the shift due to different concentrations of these proteins is not easy to detect directly. For the signal amplification, we used an amplification antibody that recognizes the target protein. For our measurements with PSA, polyclonal antibody (pAb) (BiosPacific, D63010) for PSA was used as a detection antibody. 100 µg/ml pAb in PBS with 1% BSA was introduced in the channels through common inlets after a short washing step with buffer. After the pAb binding signal was saturated, the channels were again washed with buffer to remove unbound antibodies and to eliminate the bulk refractive index effect due to free pAb solution in the channels. This way the absolute effect of pAb binding on the sensor area was measured. The centroid shifts due to the absolute pAb binding step were extracted to plot the calibration curves presented in this work.

2.6 ELISA protocol

Enzyme linked immunosorbent assay, ELISA, is a gold standard method for detection of markers in clinical diagnostics. We have performed a few ELISA measurements to compare it with our platform performance.

We followed a standard ELISA protocol starting with a non-coated 96 well ELISA plate. To immobilize the capture antibodies, we prepared antibody dilutions in 50 mM carbonate buffer (CB) incubated them in the wells for 18 hours at 4^{o}C. Then, the wells were washed 3 times with 10mM PBS-Tween and the markers are introduced into the wells, diluted in PBS-BSA (1%). After an hour of incubation at 37^{o}C the wells are again washed 3 times with PBS-Tween and the amplification antibody used on-chip experiments is introduced to the wells to form the sandwich. Similarly to the previous steps, after 1 hour of incubation, the wells were washed and secondary antibody - horseradish peroxidase (HRP) conjugate is added to the wells. It is important to note that the Goat anti-Mouse (GAM) or Goat anti-Rabbit (GAR) antibodies are used depending on the source of the amplification antibody in the previous step. After the incubation of the conjugate, the wells are again washed and the colorimetric substrate, OPD (o-phenylenediamine dihydrochloride) is added to the wells. Once the color of the solution in the wells turn yellow (takes around 30 mins) the stop solution (2.5 M H_2SO_4) is added on the OPD and absorption in the wells are read by the plate-reader.

2.7 Data processing and Analytics

One of the key advantages of the integration of optical sensing with the microfluidic chip technology is to be able to get an instant readout of the sample concentration during the assay steps. In order to achieve that, our transmission microscopy set-up and a dedicated labview program collect the real-time transmission spectra of the sensing sites on the chips. The $reference$ signal from an area on the chip with no sensors for each sensing site and the $background$ signal (dark signal) are recorded in the beginning of the measurement and the rest of the readout is ran automatically, scanning the sensing chip with a galvo mirror. The extinction is calculated by the following formula:

$$E = \log(1 - T) = \log\left(\frac{reference - background}{signal - background}\right) \quad (11)$$

where T is transmission through the sample and $signal$ is the experimental signal readout of the sensors. The extinction centroid is calculated as described in Chapter 1 in real-time and displayed during the measurement, enabling immediate access to the results and quick troubleshooting in case of any problem with the assay or the chip. Figure 2-8 shows the real-time centroid shifts for CA15-3 detection measurement on an LSPR chip. All the surface chemistry and assay steps can be tracked during the experiment, allowing for gathering the maximum information.

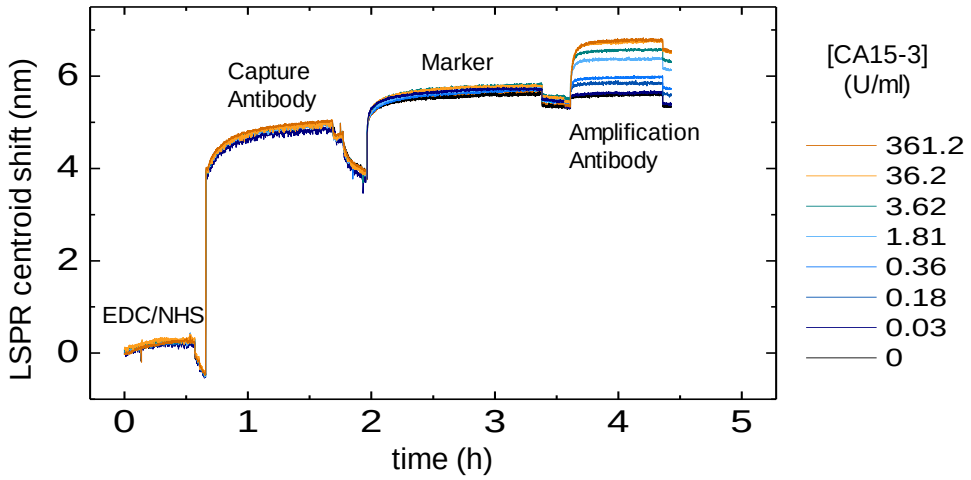

Figure 2-8 The real-time LSPR centroid shifts due to 8 different CA 15-3 concentration solutions at the 8 separate detection sites on a chip.

After the measurements, offline data processing is performed to get more information out of the collected data. The centroid shifts for detection antibody binding over the time is calculated for each sensing site and plotted against corresponding concentrations (See Figure 2-9). This plot is called *concentration-response curve* or *calibration curve* in analytical chemistry and has a trend of an S-curve. The data is fitted by four parameter logistic function:

$$y = max + \frac{min - max}{1 + \left(\frac{x}{C}\right)^{s}} \tag{12}$$

where;

max = the maximum value that can be obtained (at infinite concentration)

min = the minimum value that can be obtained (at zero concentration)

C = deflection point of the S-curve, EC50 value (the point halfway between max and min, 50% Effect Concentration)

s = Hill's slope of the curve (steepness of the curve at EC50 value)

From the fitted data, the dynamic range and limit of detection (LOD) and limit of quantification (LOQ) of the calibration curve are calculated.

Dynamic range is the interval between upper and lower limits of quantitation, which is the range that the curve is linear and therefore the measurement is expected to be precise and accurate, also called as the working range of the sensors. This range is taken to be the range between EC20 and EC80 values of the calibration curve.

LOD of the sensor is the smallest analyte concentration that can be detected but not necessarily quantified exactly. Commonly it is defined as the 3 times the standard deviation on the blank measurement (measurement of the noise level in the assay when no analyte is present). For our measurements we took the EC10 value of the fitted curve as the LOD, as a convention.

LOQ is the lowest concentration that can be quantified exactly. It is defined as 10xLOD.

The sensitivity is defined as the assay response per unit analyte concentration. However this parameter is often defined differently by researchers and sometimes in conflicting senses. Some researchers define sensitivity as the LOD or LOQ or the resolution (smallest concentration difference that can be determined with confidence). Therefore, proper assessment of dynamic range and LOD is what we focus on in our measurements. For sensitivity we present the EC50 value of our sensors in the following chapters.

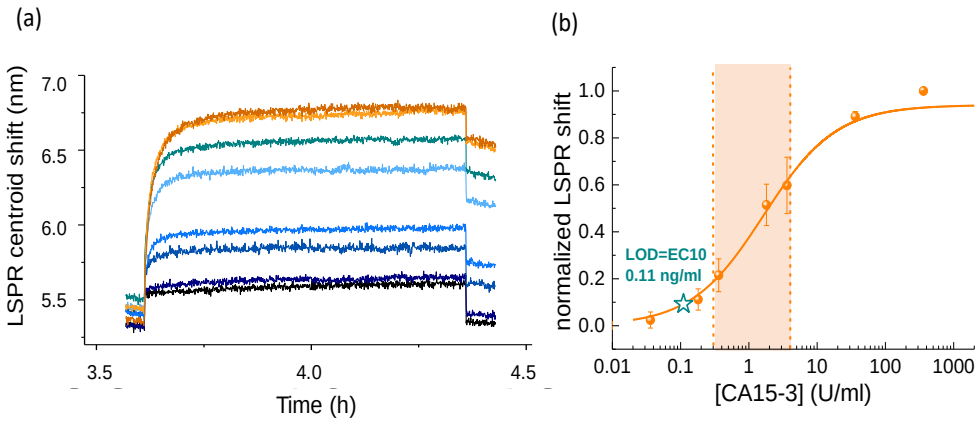

Figure 2-9 Obtaining calibration curves. (a) the LSPR shifts for the amplification antibody step from Figure 2-8. (b) the calibration curve obtained. The line is the 4-parameter logistic curve fit and the dashed region is the dynamic range of the sensor. LOD of 0.11 ng/ml is marked with a star.

3 ON-CHIP MULTIPLEXED LSPR SENSING

The results presented in this chapter as well as part of text and figures are published in ACS Sensors during the course of my PhD studies.[59]

Yavas, O.; Acimovic, S. S.; Garcia-Guirado, J.; Berthelot, J.; Dobosz, P.; Sanz, V.; Quidant, R. Self-Calibrating on-a-Chip LSPR Sensing for Quantitative and Multiplexed Detection of Cancer Markers in Human Serum. ACS Sensors 2018, 3 (7), 1376–1384.

Abstract - The need for point-of-care (POC) devices capable of early detecting diseases and monitoring their status, out of a lab environment, has stimulated the development of compact biosensing configurations. While Localized Surface Plasmon Resonance (LSPR) sensing integrated into a state-of-the-art microfluidic chip stands as a promising approach to meet this demand, its implementation into an operating sensing platform capable to detect quantitatively a set of molecular biomarkers in an unknown biological sample is only at its infancy. In this chapter, we present an on-chip LSPR chip capable to perform automatic, quantitative and multiplexed, screening of biomarkers. We demonstrate its versatility by programming it to detect and quantify in human serum four relevant human serum protein markers associated with breast-cancer.

Early diagnosis and accurate monitoring of disease progression is required to determine an optimum treatment and increase the recovery rate of patients. The complex nature of biological processes and pathways leads to significant changes in the levels of multiple molecular markers in patient's blood over the course of a disease.[60–62] Therefore, it is highly relevant to be able to track simultaneously the levels of a set of these markers, in order to spot the actual disease status. Enzyme-linked immunosorbent assay, ELISA is one of the most commonly used detection technique in clinics and research laboratories.[63] Its reliability, low limit of detection and commercial availability are the biggest advantages. However, the bulky well-plates and readers, long assay times and the large reagent volumes are not compatible with on-site, quick and multiplexed measurements. The ultimate goal

of developing point-of-care (POC) devices that allow for on-site, multiplexed measurement of analytes in a fast and cost-effective manner has motivated the development of a variety of biosensors based on different transduction mechanisms.[64–67] Among them, optical sensors are particularly attractive owing to their fast response and compatibility with miniaturization and parallel sensing.[34,68,69] Surface Plasmon Resonance (SPR) sensing is one of the well-developed and commercially available optical sensing schemes.

A competitive approach to optical sensing relies on Localized Surface Plasmon Resonance (LSPR) supported by noble metal nanoparticles. Unlike SPR-sensing based on flat metal films, LSPR-sensing enables engineering the sensing volume down to the subwavelength (molecular) scale and benefits from direct coupling with propagating light. LSPR-based biosensing has shown to be a powerful approach to compact and simple platforms, especially attractive for POC applications.[34,69–75] Yet, despite its great potential, its implementation into operating sensing devices capable to quantitatively assess the analyte concentration from unknown biological samples, remains little advanced.[29,76] This is in part due to the complexity of implementing a working platform, where several disciplines like physics, surface chemistry, fluidics and electronics have to be optimally combined. Furthermore, while most efforts have so far focused on the detection of single analytes, reliable detection and monitoring of diseases generally requires multiplexed detection of several biomarkers. To this end, earlier works proposed employing colloidal metallic nanoparticles with different LSPR frequencies, each functionalized with a different receptor.[77] While promising, this solution-based approach currently faces several drawbacks including aggregation of nanoparticles and optical signal fluctuations due to multiple washing steps. Another related configuration for multiplexing consists in immobilizing on a substrate antibody-functionalized gold nanorods of different aspect ratios[78] that exhibit different optical properties allowing the selection of multiple working wavelengths. Chen *et al*. developed a multiplex serum cytokine immunoassay using nanoplasmonic biosensor microarrays. In this configuration, the solution based gold nanorods were immobilized on a substrate using a microfluidic channel network which was then removed and replaced by another microfluidic network used for the sensing assay.[69] To date, none of the proposed LSPR-based schemes has enabled multiplexed and quantitative detection of several analytes in a biological sample.

As a first step towards this goal, we recently presented a strategy[34] that combines top-down engineered gold nanoparticle arrays with state-of-the-art microfluidics[19–23] comprising micromechanical valves.[46] This unique combination, which provides a controlled environment to the sensors, accurate delivery of

reagents and sample as well as automated assay operation, was successfully used to detect protein cancer markers in human serum with high sensitivity and specificity. As a proof of principle, detection of prostate specific antigen (PSA) and alpha-fetoprotein (AFP) in a clinically relevant level range were successively obtained.[34]

Here, by leveraging on the developed toolbox, we report on the first implementation of quantitative and multiplexed LSPR sensing on-a-chip. Our LSPR chip enables us to perform simultaneously self-calibrating, automated and multiplexed real-time detection of four breast cancer protein markers in human serum. These sensing performances combined with the long shelf-life of the chips, brings the LSPR based sensing one step closer to real-life operating POC devices.

In the next sections, we discuss the clinical motivation, the platform design, and the results related to the sensing applications.

3.1 Clinical Motivation

Clinical studies show that accurate detection of serum protein markers for breast cancer are pivotal to treatment monitoring towards a better prognosis.[84–92] The most common markers are CA (cancer antigen) 15-3 and CEA (carcinoembryonic antigen).[86,87,92] Also high serum ErbB2 (HER-2/Neu) concentrations are shown to be of use to monitor the response to specific treatment types.[85,91] In addition to these antigens, the CA 125, which is a serum marker for ovarian cancer and some other diseases, is also shown to be a predictive marker of metastasis in breast cancer patients.[84] More serum protein markers are relevant to breast cancer; extensive reviews can be found in the literature.[88,92,93] Since tracking the level of a single marker alone may not be sufficiently conclusive in most cases, one needs to be able to monitor multiple markers in parallel. In our multiplexed measurements, we have focused on the four aforementioned molecules to demonstrate that our platform enables us to reliably quantify the concentrations of four relevant molecules with high specificity and reduced cross-reactivity.

To assess our sensing performance, we also list the clinical cut-off concentrations of the selected markers with our results later in Table 2. The clinical cut-off concentration of a marker is the maximum concentration that a sample can contain to be considered healthy.

3.2 Multiplexed detection chip

To meet all requirements for quantitative multiplexed sensing, our chip design makes use of orthogonally crossing channels compartmented by micro-mechanical valves. The eight microfluidic channels intersect with four orthogonal channels and each intersection area contains an array of gold nanorods sensors (Figure 3-1). Eventually, the density of sensing sites is 32/mm^2, enabling time-shared parallel detection over different positions by using a galvanometric mirror in a transmission measurement setup[34].

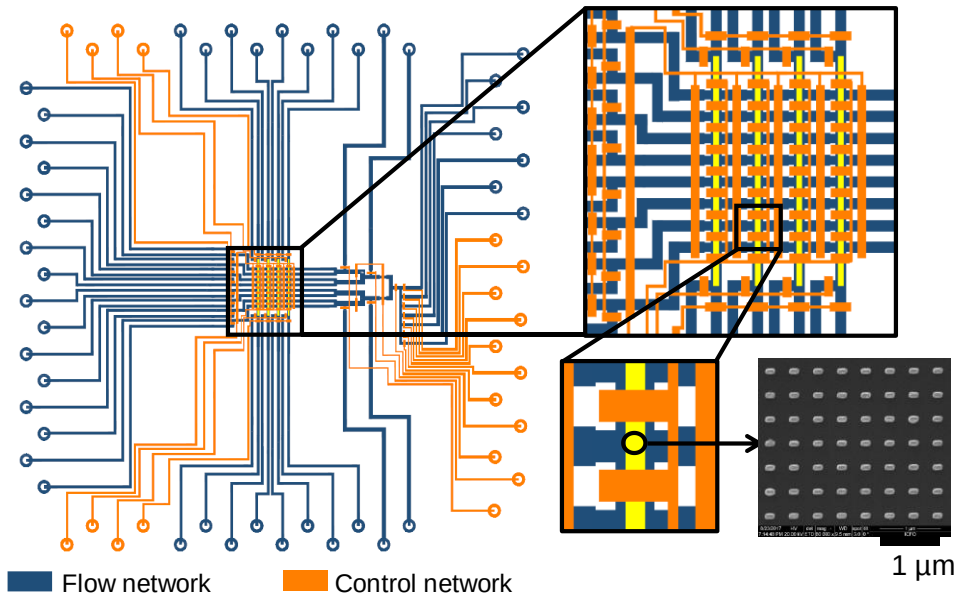

Figure 3-1 Description of the microfluidic LSPR sensing chip. Design of the microfluidic chip where the blue lines represent the flow network and the orange lines represent the valve control network of the multilayer PDMS chip. The yellow lines inside the blue channels locate the gold nanorod array.

The dimensions and the periodicity of the gold nanorods in this work are similar to some previous works[34,94] Gold nanorods are 160 nm x 80 nm with thickness of 50 nm and arranged in a square lattice of 400 nm pitch. This design was selected to minimize near and far field coupling effects and to lead to a strong resonance in the extinction signal. Figure 3-2 shows the SEM image of the gold nanorod arrays and their extinction spectrum in water.

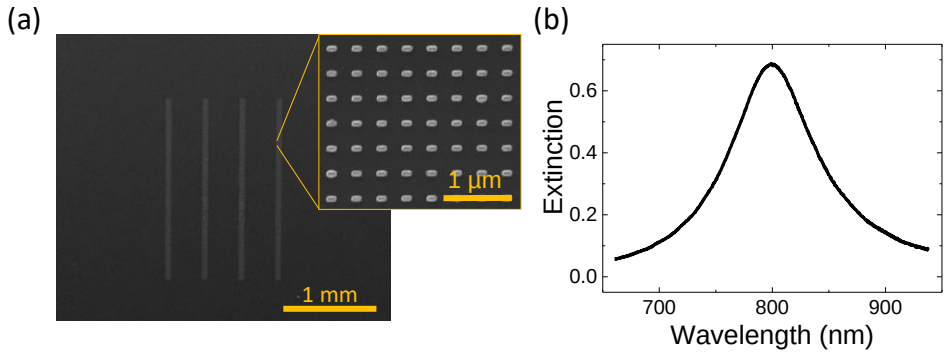

Figure 3-2 The gold nanorod sensor arrays. (a) The SEM image of the fabricated arrays. 4 lines of gold nanorod arrays are fabricated for easy aligning with the detection sites on the microfluidic channel network. (b) The extinction spectra of the gold nanorod array in (a), measured in aqueous environment.

Figure 3-1 displays the chip outline where blue lines depict the flow network and red lines the valve-actuation architecture for flow control[46]. As detailed in Chapter 2, e-beam lithography with negative resists combined with reactive ion etching were used to fabricate gold nanorod arrays on a glass substrate (Figure 3-2). Subsequently, the surface of the nanorods was coated with a self-assembled monolayer (SAM) of MUA (mercaptoundecanoic acid) for further modification aimed at specific analyte binding. Finally, we aligned and assembled the sensor substrate with microfluidic channels, fabricated by multilayer soft lithography[46], in such a way the nanorod arrays sit at the intersection points of orthogonal channels (Figure 3-1). By regulating the pressure inside the control lines, the flow on the chip can be actuated to address specific detection sites. The details of the opto-fluidic setup and the automated valve control system is described in Chapter 2.

For the biomarker detection on chip, the sandwich assay format was used, where a capture antibody is first immobilized on the sensor in order to specifically capture the protein of interest and, when needed, the LSPR shift is subsequently amplified with an amplification antibody (Figure 3-3a). The LSPR centroid red-shift at the detection sites due to bioanalyte binding is tracked in real-time with a home-made transmission spectroscopy setup controlled by a Labview interface. Figure 3-3b shows the real-time measurement of the successive assay steps for obtaining CA15-3 calibration curve, involving only 25% of the total sensing sites available on the chip. The EDC/NHS activation of the carboxyl groups of the SAM is followed by the capture antibody immobilization on 8 sensors, onto which 8 different concentrations of the marker are introduced. The final step (zoomed in inset) shows the amplification antibody binding at the 8 different detection sites,

resolving the different concentrations of the marker. The washing steps in between can be seen in the real-time data.

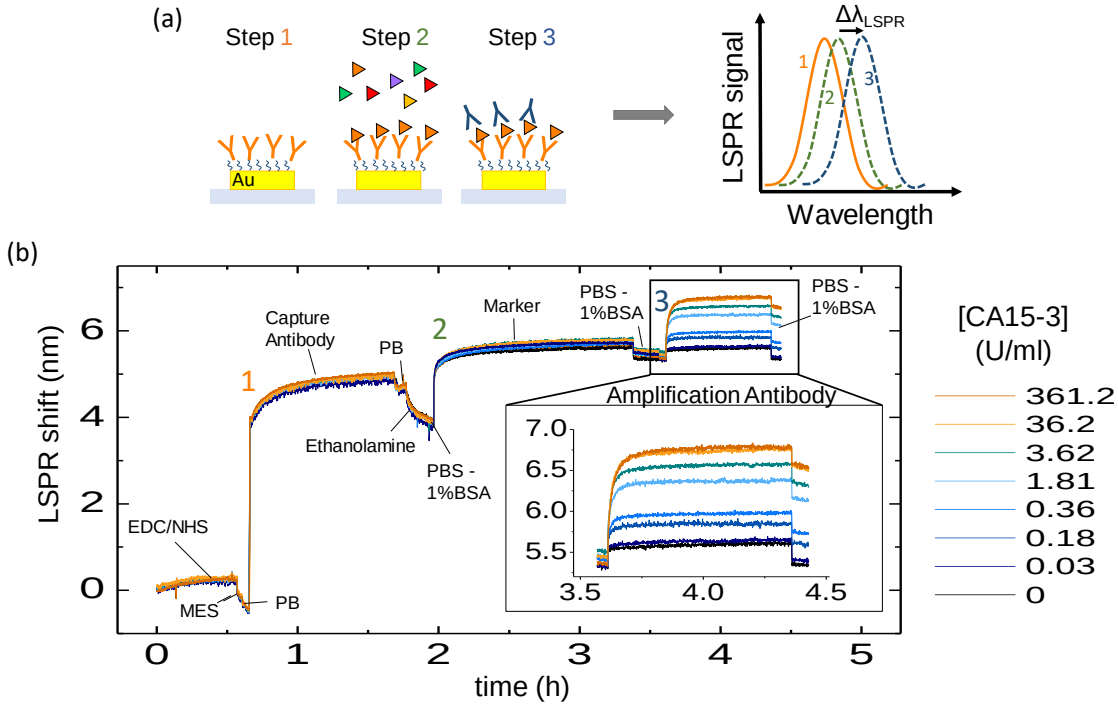

Figure 3-3 Sandwich assay on LSPR sensors. (a) The sketch of the sandwich assay steps and the LSPR signal response. (b) Real-time monitoring of the LSPR centroid shift for different concentrations of CA15-3 (on-a-chip calibration curve).

The inlets and outlets of the chip are designed such that the antigen cocktail samples and the capture and amplification antibody solutions are connected to the chip through tygon tubing and they can be flowed whenever needed without any further manual manipulation by the help of electronic valves and the control software. Controlled flow of different solutions in specific directions and without cross contamination is shown in Figure 3-4a, where the main three flow modes of the microfluidic operation are captured using food colorant. This way, every detection site can be treated simultaneously with the same reagent/solution through a common inlet (Figure 3-4a, mode i). Additionally, different solutions can be delivered to the detection sites through the orthogonal channels in different directions as shown in Figure 3-4a, mode ii and Figure 3-4a, mode iii. These different flow modes, together with the low dead volumes and absence of cross-talk between channels, are crucial for reliable multiplexed measurements.

In the specific multiplexed sensing assay, the common treatment of all sensor sites (mode i) is used to activate the gold sensor surface with EDC/NHS chemistry[8,38] and for common blocking and washing steps. Mode iii is employed to immobilize the 4 different capture antibodies on the four sensor arrays (Figure 3-4b and c, Step 1). Six of the eight parallel channels are used, utilizing mode ii, to deliver to the sensors the cocktail of proteins with different concentrations and obtain the calibration curves of the four proteins. The last two channels are simultaneously used for the unknown sample replicas to be quantified (Figure 3-4b and c, Step 2). Finally, whenever necessary, the amplification antibodies are flowed through to amplify resonance shift (Figure 3-4b and c, Step 3). More details on the surface chemistry and marker detection protocol can be found in Chapter 2. The contribution of the flow control by the micromechanical valves to both the sensor functionalization and the sensing measurements, is illustrated by the cross-section view of the chip in Figure 3-4c.

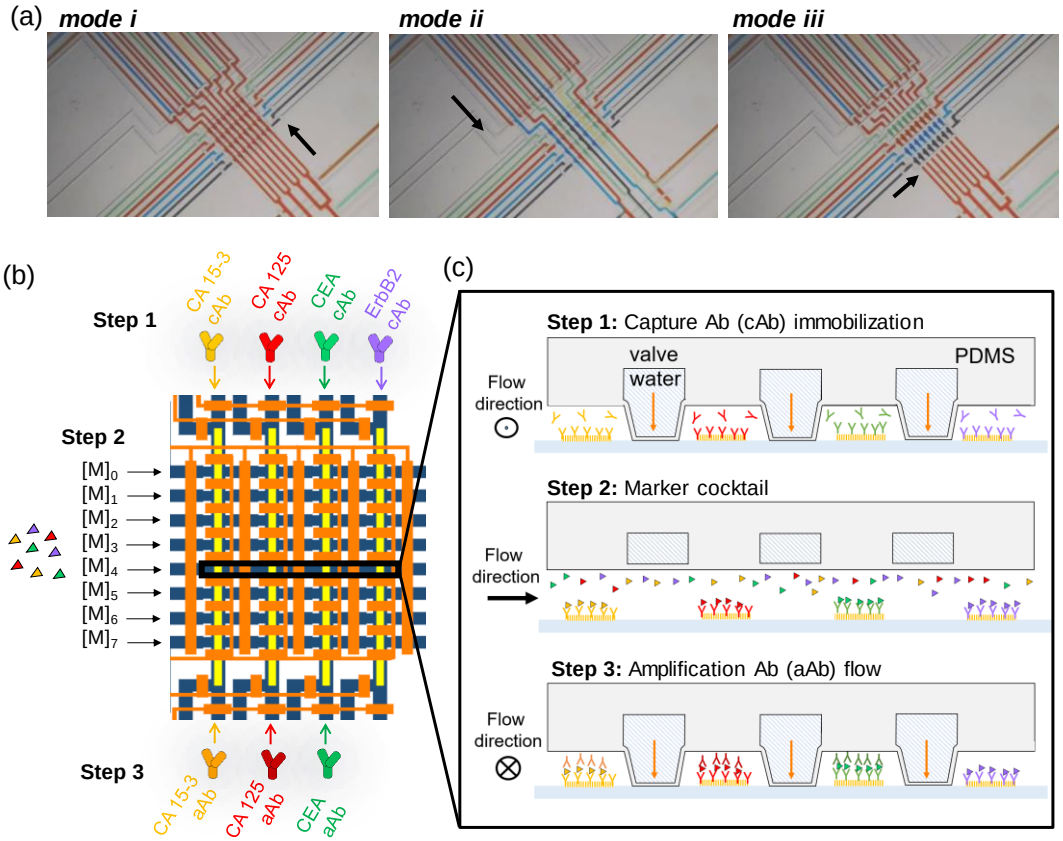

Figure 3-4 Description of the chip operation protocol for the multiplexed detection of four protein cancer markers. (a) Pictures of the microfluidic channels flow layer at different instants of the sensing

protocol. For sake of clarity, food dyes were used. The 8 channels can be either fed by a common inlet (mode i) or addressed individually (mode ii). In mode iii, the 4 orthogonal channels are addressed separately and flow can be adjusted to be in two opposite directions. (b) Steps of the multiplexed sensing assay in which the capture antibodies of different markers are first immobilized on the surface (Step 1), then the marker cocktails with different concentrations [M]i are flown through individual channels (Step 2) and finally the amplification antibody of respective markers are flown through the orthogonal channels (Step 3). (c) Cross section of the chip at the position marked by the black rectangle on (b) illustrating the flow directions and the valve operation.

With this novel LSPR chip design, the high density of addressable sensing sites increases the throughput and a proper configuration of the assay via the flow step sequence enables the chip to perform self-calibrations. Remarkably, the on-chip calibration for a given analyte can be simultaneously recorded while measuring the actual unknown biological sample, improving the reliability of the quantification. Equally important, the orthogonal channels allow the antibodies to be immobilized exclusively on the sensing areas, thus significantly reducing parasitic effects of analyte depletion (due to non-specific interactions)[33], and allowing more freedom in passivation strategies. Finally, the whole biosensing assay can be fully programmed and automatized for a wider range of applications based on label-free operation (for instance, affinity screening in pharmaceutical industry). All these advanced features of microfluidic platform combined with the real-time LSPR centroid shift tracking, enables a reliable, multipurpose platform.

3.3 Multiplexed cancer marker detection in human serum

3.3.1 Optimizations

In order to have reliable and sensitive sensing protocol developed, many parameters such as assay time, antibody type and antibody concentrations have to be optimized. This requires multiple test runs before any meaningful multiplexing application can be implemented. The next subsections are going to focus on the steps followed for optimizing the performance of sensing.

Antibody selection

The selection of available antibodies is especially a tricky step due to low quality of antibodies available only for research in the market. The protocol is to order multiple antibodies from different vendors and test them on our own platform. A pair of antibodies recognizing the same marker on different epitopes are needed to be selected. We have tested numerous antibody pairs in order to settle the pairs that worked well for our multiplexed detection measurements. CA15-3, CA 125, CEA and ErbB2 capture antibody (Biospacific A46040, A46075, G-116-C and Abcam ab16901 respectively) and amplification antibody (Biospacific A46050, A46074, A26021489P respectively) are selected for the markers (Biospacific J66301170, J6620117, J62000452 and Abcam ab60866, respectively) by trial and error. For ErbB2, the amplification step is skipped since the marker detection directly resulted in a sensitive calibration curve.

Antibody concentrations

To ensure the quality of the on-chip sandwich assays, we have first optimized the capture and amplification antibody concentrations and determined the analytical performances of each of the 4 molecules, individually.

In order to determine the optimum concentrations of each of the capture antibodies, we first immobilized 4 different concentrations of capture antibody for the marker of interest and then flowed 8 different marker concentrations, followed by the amplification antibody solution at constant concentration. From these collection of data, all obtained from a single chip, one can plot four different calibration curves, one for each of the capture antibody concentrations. The best capture antibody concentration was selected accounting for the high slope, low unspecific signal and high sensitivity. To compensate for the reduced dynamical range, one can use sample dilution. Alternatively, antibody concentration and assay conditions can be optimized to obtain larger dynamic ranges. Following a similar approach, on another chip, we optimized the amplification antibody concentrations, immobilizing the optimum solution of capture antibody on the sensors and running the calibration curve measurements with 4 varying amplification antibody concentrations this time. Figure 3-5 shows the obtained calibration curves for tested capture and amplification antibody concentrations. For ErbB2, since there is no amplification antibody, in (f) the further capture antibody optimization is presented.

Following this protocol, we determined the optimum concentrations of all the antibody pairs used for further sensing applications (Table 1) . As a result, the individual calibration curves for the 4 protein markers to be detected, by optimized antibody concentrations are obtained (Figure 3-6). The dynamic ranges and the

limit of detections of these individual marker measurements can be found in Table 2. For ErbB2 protein, the direct protein detection without amplification antibody signal was sufficient to obtain a sensitive enough calibration curve. This effect can be due to the possible higher affinity constant of the selected antibody for ErbB2 compared to the other proteins or effects related to the 3D structure of the protein or steric hindrances when the antigen is immobilized on the sensor surface.

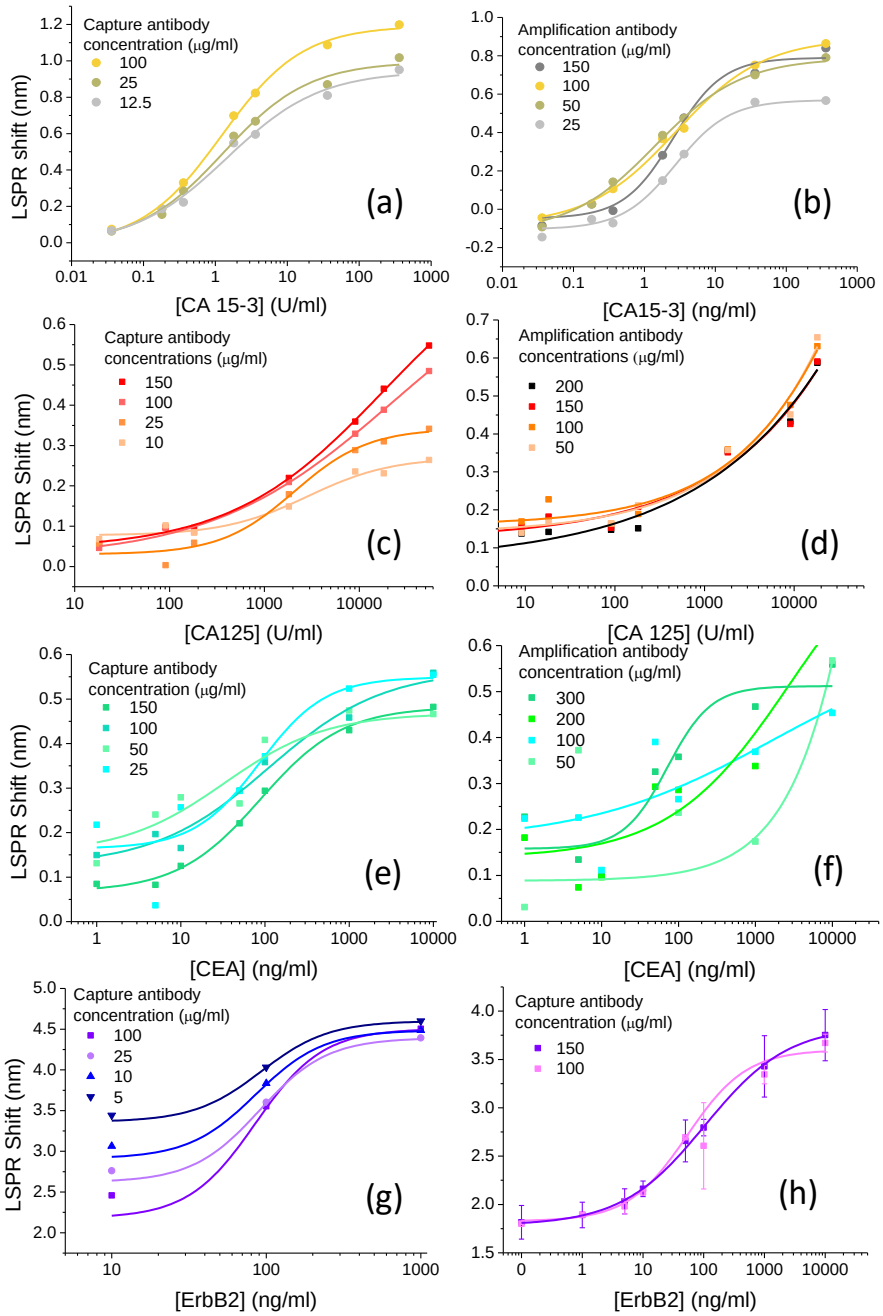

Figure 3-5 Antibody concentration optimization experiments for (a,b) CA 15-3, (c,d) CA125, (e,f) CEA and (g,h) ErbB2 markers.

	Optimum Capture Antibody Concentration (mg/ml)	Optimum Amplification Antibody Concentration (mg/ml)
CA 15-3	100	100
CA 125	150	150
CEA	150	200
ErbB2	150	-

Table 1 Optimum antibody concentrations determined from the optimization experiments.

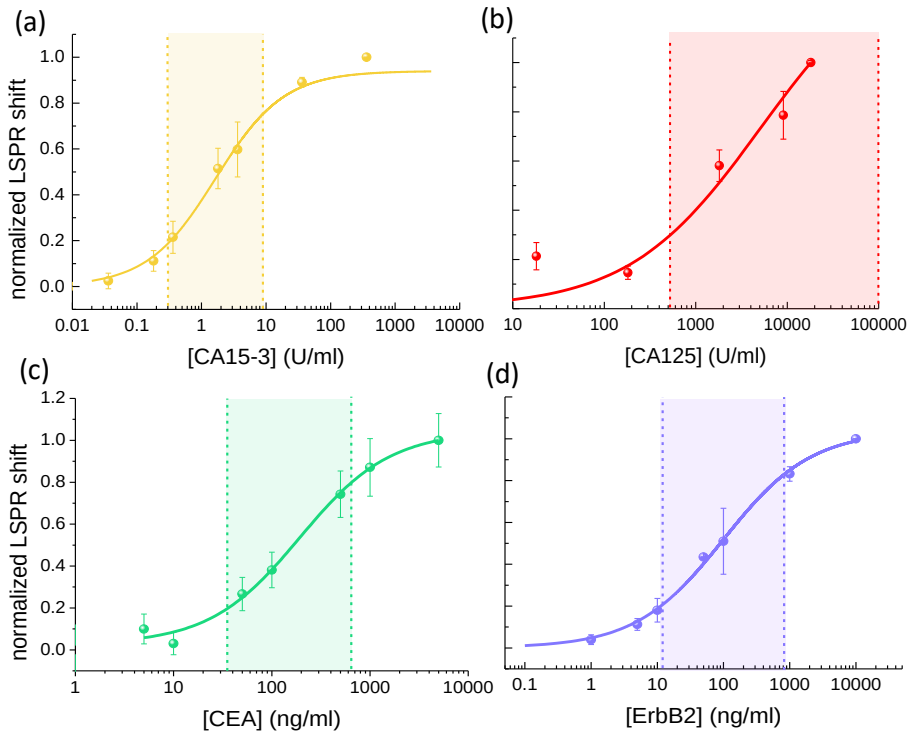

Figure 3-6 Individual calibration curves for the four biomarkers obtained for optimized antibody concentrations. Error bars reflect the deviation between replicas on different chips for (c) and (e), and on the same chip for (d) and (f).

In order to have a clear comparison between different measurements and different markers, the normalized calibration curve data is plotted in Figure 3-6. The error bars on the calibration curve data represent the variation between replicas from different chips for CA 15-3 and CA 125 and on the same chip for CEA and ErbB2. The relative standard deviation (standard deviation/mean signal)

between replicas in the dynamic range is ~14% for interchip measurements and ~19% for intrachip measurements, suggesting that the reproducibility on different chips is as high as on the same chip. Owing to the self-calibration capacity of the platform, the sample quantification performance of the platform is independent of such small variations.

The detection sensitivity extracted from the calibration curves for CA 15-3, Erb2 and CEA are compatible with clinical cut-off values[84,85,87,92]. For CA 125, the not so good limit of detection is attributed to the low quality of available antibodies.

Shelf-life of the device

It is important to know the shelf-life of the fabricated platform for a step towards POC device development. We have tested and found that once assembled, the chip can be stored at room temperature, in dark, up to 3 months without any significant alteration of its performance. Figure 3-7, shows the antibody binding performance of 1-week old and 3-months old chips, as well as associated calibration curves obtained by sandwich assay for CA15-3 protein.

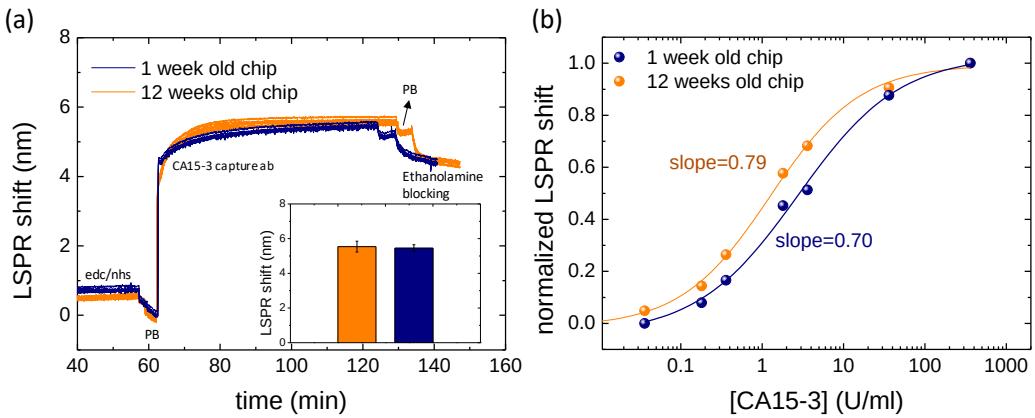

Figure 3-7 Shelf life of the fabricated chips. (a) the real time LSPR shift signals of the capture antibody binding on the sensors tested by 1 week old and 12 week old chips.(b) the CA15-3 calibration curves obtained on the respective chips in (a). The slope of the curves are shown on the graph. Data in (b) is normalized for fair comparison of shifts on different chips.

Assay time

The assay time for the on-chip immunoassays is another parameter to optimize, in order to achieve an efficient and fast detection scheme. In our experiments, we have used 1 hour of antibody and sample flow time, to keep consistency between previous measurements[34] and our experiments and keeping this parameter constant, we optimized for antibody concentrations. However, the capture antibody immobilization time can be optimized to achieve faster sensor

preparation. As can be seen from Figure 3-7a, the LSPR shift saturates quickly after the capture antibody is introduced into the channels. 10-15 minutes of minimum antibody flow time is sufficient for coating the sensor surface with capture antibodies. Similarly, the real time LSPR sensing data (see Figure 2-8) suggests that the calibration curves obtained during the detection antibody flow, can be shortened down to 15 minutes, as the LSPR shift signal saturates after 15 minutes. A careful conduction of assay time optimization experiments can provide the minimum assay time with maximum sensitivity and dynamic range.

3.3.2 Cross reactivity

Nonspecific antibody-protein cross-reaction results in inaccuracy and unreliable sensor response, interfering with the purpose of multiplexing[95,96]. In order to verify the specificity of the platform, we conducted a cross-reactivity control experiment (Figure 3-8a), where we immobilized the capture antibodies against CA 15-3, CA125, CEA and Erb2 on four sensor arrays (flow mode iii) and we flowed high concentrations of the four proteins individually (flow mode ii). Concentrations of proteins were selected to be the maximum ones of the dynamic ranges of their respective calibration curves. LSPR shifts obtained after sandwich formation for CA 15-3, CA125 and CEA channels and during the sample flow for ErbB2 channels are presented in Figure 3-8b. No cross-reactivity was observed between different species despite the high concentrations of proteins used.

Conventionally, the cross-reactivity between two molecules are analysed by comparing the calibration curves obtained alone and in presence of the two molecules and calculated as shown in ref [95]. To test our platform and antibody-marker pairs in a conventional way, in addition to the cross-reactivity experiment described above and in main text, we have selected the CA15-3 antibody and ErbB2 protein pair and performed a conventional cross-reactivity control experiment. Figure 3-9 show the calibration curve of CA 15-3, obtained alone and in presence of ErbB2 molecule. Black data points are corresponding to a measurement of CA15-3 and ErbB2 mixture at the linear range of CA15-3 calibration curve obtained alone (yellow data points). The raw LSPR shifts for both experiments are shown with no normalization. The agreement between two sets of data show that there is no effect of the presence of ErbB2 molecule on the CA15-3 calibration curve obtained by sandwich assay.

Similarly, the data on multiplexed detection in PBS buffer presented in the next section, compared with the individually obtained calibration, show that there is no cross-reactivity between any of the antigen-antibody pairs (Figure 3-10).

Our data show that the platform ensures limited cross-contamination between the channels and the antibody selections prevent any significant cross-reactivity.

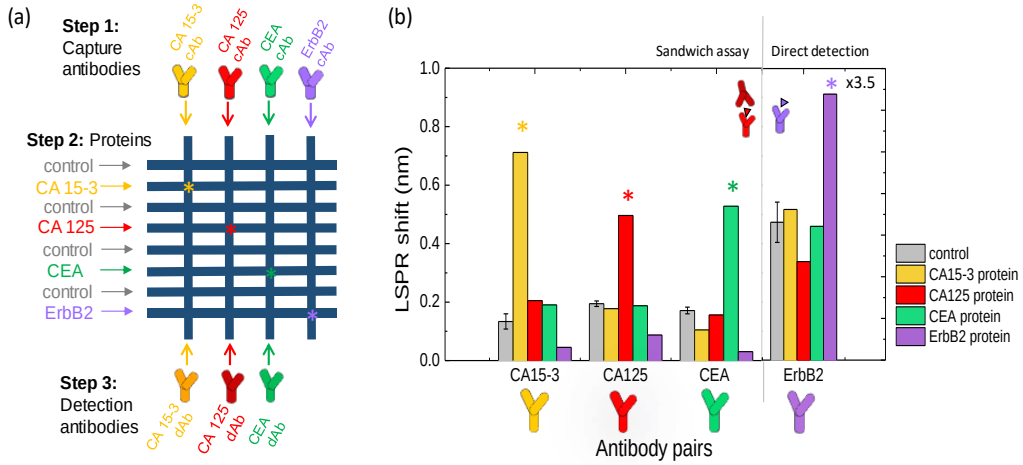

Figure 3-8 Cross-reactivity experiments. (a) Sketch of the experimental steps (For sake of clarity, the control layer of the chip is not shown). Capture antibodies are immobilized and the proteins are flowed separately in different channels. Four replicas of the controls with no proteins is flowed also to check for channel-to-channel variation of the signals. Every intersection of the orthogonal flow channels is a sensing region. The sensing regions corresponding to each matching antibody-protein pair is marked with a star. (b) Corresponding LSPR shifts on the sensors. Shifts for the control channels are merged and the error bar is associated to the standard deviation of four replicas for the control measurement with each antibody pair. The protein concentrations are 18U/ml, 9000kU/ml, 3200ng/ml and 600ng/ml for CA 15-3, CA 125, CEA and ErbB2 respectively.

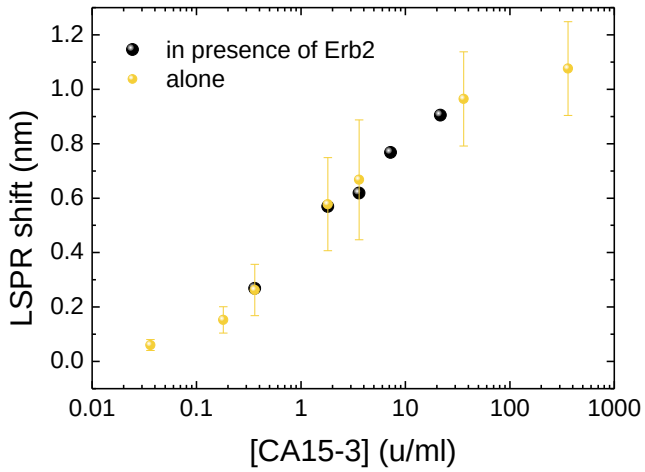

Figure 3-9 The cross-reactivity control experiment where the CA15-3 calibration points are obtained individually and in presence of ErbB2 marker. No cross-reactivity is observed. The calibration data obtained with solutions prepared in PBS with 1% BSA.

3.3.3 Multiplexed detection

As a proof of principle experiment of multiplexed detection of the 4 biomarkers, we performed calibration curve measurements in 10mM PBS buffer with 1% BSA (bovine serum albumin) as a blocking agent. Each of the four capture antibodies was immobilized on a different sensor array (utilizing mode iii and step 1 described in Figure 3-4) and 8 cocktails of proteins with varying concentrations were flowed into the chip (utilizing mode ii and step 2 described in Figure 3-4) before introducing the amplification antibodies (Figure 3-4b, step3). Normalized calibration curves obtained for each protein marker are presented in Figure 3-10. Multiplexed measurements exhibit similar response compared to individually obtained calibration curves (dashed lines in Figure 3-10), showing no cross-reactivity between the four proteins. A detailed comparison of the sensitivity (half maximal effective concentration, EC50), limit of detection (LOD at EC10), and the dynamic ranges of the curves (EC20-EC80) is presented in Table 1.

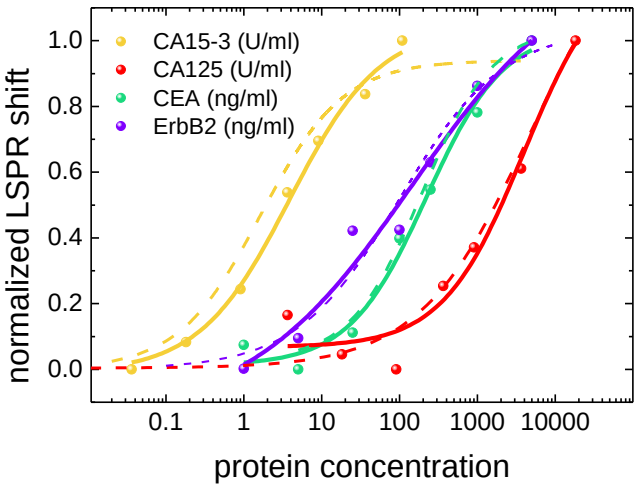

Figure 3-10 Multiplexed detection of four molecules in PBS. Solid lines are the four-parameter logistic equation fit to the data. The dashed lines are the fit to the individually obtained calibration curves.

3.3.4 Detection in human serum and sample quantification

Following the multiplexed measurement in buffer, we demonstrate here multiplexed detection in 100% human serum. Figure 3-11a demonstrates the calibration curves obtained simultaneously from a single chip. Table 1 summarizes the LOD, sensitivity and dynamic range of the four markers measured in human serum. Due to the complex matrix, the curves are shifted towards higher concentrations compared to the measurements in PBS-BSA(1%) (dashed lines in Figure 3-11a) and therefore the LOD and EC50 values are slightly higher. Measurements were repeated 3 times to demonstrate their reproducibility. Data, presented in Figure 3-11b, exhibit very similar characteristics, suggesting high interchip reproducibility, especially in the sandwich assays for CA 15-3, CEA and CA125. The calibration curves for ErbB2 show larger dispersion, mostly because, for this molecule, no amplification antibody was used. Therefore for this application, the sandwich assay approach with detection antibodies provided more reproducible curves in complex media.

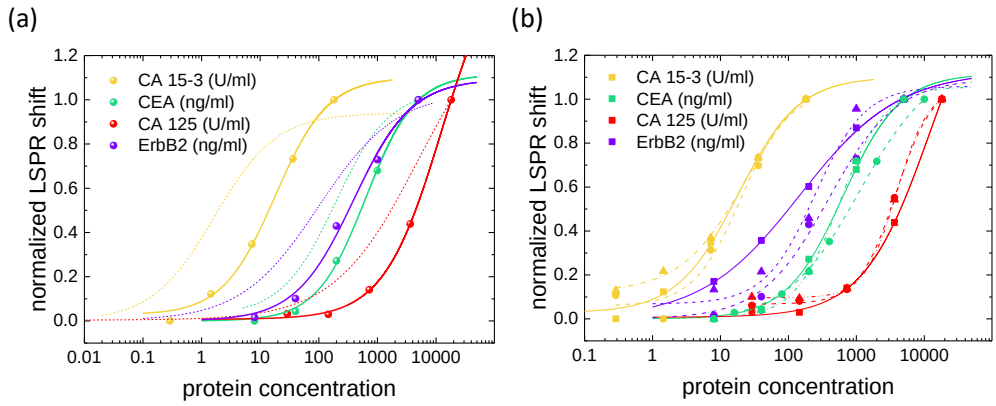

Figure 3-11 Multiplexed detection in human serum. (a) Calibration curves simultaneously obtained in 100% human serum (solid lines), and in PBS buffer from Figure 3-10 (dashed lines). (b) The calibration curves obtained on 3 different chips (solid, dashed and dotted lines).

As a final step, towards real multiplexed sensing experiment on an unknown clinical sample, we demonstrate multiplexed sample recovery. To this end, we prepared six cocktails with varying biomarker concentrations for calibration curve. Then for recovering purpose, we spiked two samples with a mixture of targeted markers at different levels in human serum to mimic an unknown clinical sample. The spiked sample concentrations were interpolated from the calibration curves that were simultaneously acquired. Figure 6b shows an example recovery measurement in whole human serum for four molecules obtained for various replicas. The recovery rates (R) are listed in the table. Two of the sample concentrations, being CA15-3 and CA 125, were found to be significantly different but not incoherent ($120\% < R \leq 130\%$). The recovery value for CEA was underestimated ($R < 80\%$). ErbB2 concentration in the spiked sample is below the linear range of the calibration curve, in order to demonstrate the sensing performance below the LOD. The prepared and quantified ErbB2 concentrations were 15 ng/ml and 20±20.2 ng/ml respectively. The uncertainties on the recovery are mostly attributed to spiking errors during sample preparation.

Marker	Cut-off concentration	Measurement	LOD	Sensitivity	Dynamic Range
CA 15-3	25-40 U/ml [92]	Individual	0.11 U/ml	2.0 U/ml	0.30-8.9 U/ml
		Multiplexed in PBS	0.21 U/ml	3.88 U/ml	0.6 – 19.2 U/ml
		Multiplexed in HS	1.85 U/ml	17.9 U/ml	4.2 – 75.4 U/ml
CA 125	35 U/ml [84]	Individual	0.138 kU/ml	4.5 kU/ml	0.524 – 100 kU/ml
		Multiplexed in PBS	0.139 kU/ml	3.9 kU/ml	0.580 – 30 kU/ml
		Multiplexed in HS	1.021 kU/ml	12.522 kU/ml	2.575 – 6.089 kU/ml
CEA	2 ng/ml [87] 5 ng/ml [84]	Individual	14.7 ng/ml	192.0 ng/ml	35.2 – 645.7 ng/ml
		Multiplexed in PBS	16.3 ng/ml	220.5 ng/ml	44.5 – 1191.3 ng/ml
		Multiplexed in HS	76.19 ng/ml	635.4 ng/ml	166.7-2422.3 ng/ml
ErbB2	15 ng/ml [85]	Individual	3.5 ng/ml	99.8 ng/ml	12.07 – 824.5 ng/ml
		Multiplexed in PBS	3.9 ng/ml	145.0 ng/ml	11.75– 1742.6 ng/ml
		Multiplexed in HS	31.9 ng/ml	391.7 ng/ml	80.5 – 1904.8 ng/ml

Table 2 The analytical parameters of the assays on chip summarized for individual marker detection (Figure 3-6), multiplexed detection in PBS buffer (Figure 3-10) and multiplexed detection in human serum (Figure 3-11a).

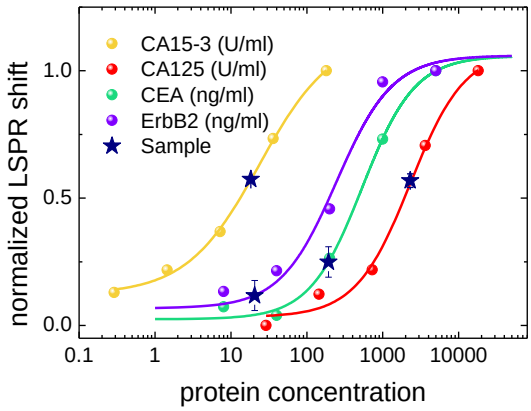

	Sample prepared	Quantified	Recovery rate
CA 15-3	14.5 U/ml	18.3 ±1.2 U/ml	126%
CA 125	1.9 kU/ml	2.30 ± 0.07 kU/ml	121 %
CEA	250 ng/ml	193 ± 52 ng/ml	77.2 %
ErbB2	15 ng/ml	<LOD	-

Figure 3-12 Sample recovery in 100% human serum. The concentrations of each marker is quantified by interpolating the measured LSPR shifts from the simultaneously acquired calibration curves. The table summarizes the recovery for each of the markers.

While our results are satisfying, this remains as proof of principle and there is quite some room left for boosting the platform performances. At that stage, the LOD levels for CA125 and CEA are higher than clinical cut-off values. The significant LOD difference between the different markers is attributed to the uneven performance of the different commercially available antibody pairs as discussed by Volpetti et al.[83] Sensitivity and recovery rates could be further improved by i) optimizing the assay buffer for human serum, ii) managing better antibody pairs that will result in better LOD and sensitivity, iii) changing the assay type[97] (competitive assay, *etc.*) or iv) engineering nanoparticle geometry[33,36,98,99].

3.4 Comparison with ELISA

Finally, in order to benchmark our technology with an established standard, we performed ELISA measurements on all four markers, using the same antibody pairs. We first optimized the capture and detection antibody concentrations for ELISA. For the sandwich step of ELISA, we selected a commercial polyclonal

antibody for ErbB2. All the rest of the antibody pairs are used in the same way as in the on-chip measurements. Calibration curves obtained with ELISA are presented in Figure 3-13.

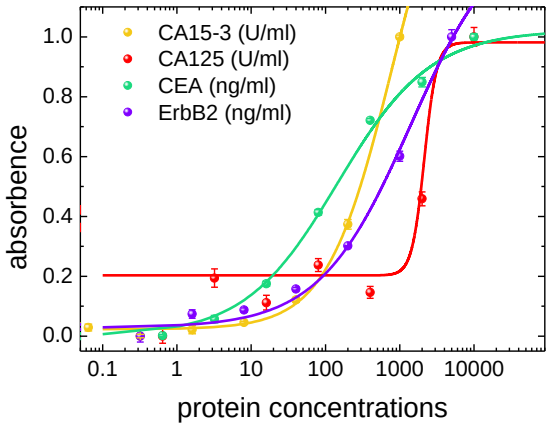

	LOD (EC10)	Sensitivity	Dynamic Range
CA 15-3	85.5 u/ml	778.7 u/ml	193.3 – 3137.7 u/ml
CA 125	1.4 ku/ml	2.1 ku/ml	1.6 –2.8 ku/ml
CEA	6.1 ng/ml	145.3 ng/ml	19.7 – 1069.2 ng/ml
ErbB2	63.2 ng/ml	1409.9 ng/ml	198.8 – 10000 ng/ml

Figure 3-13 The calibration curves obtained by ELISA. The table summarizes the analytical parameters.

From this direct comparison, we show that the LOD for CA15-3, CA125 and ErbB2 molecules are lower for on-chip measurements, outperforming the corresponding ELISA measurements. Another advantage our platform holds is its shorter total assay time, which in the commercialized kits, reported as 5 hours for ELISA, where the capture antibody is already immobilized inside the wells. After the capture antibody is immobilized on our sensors, our assay time is maximum 2.5 hours which can be seen in Figure 3-3b. The detection antibody step is now set at 1 hour but can be easily reduced to 15-20 minutes (as can be seen from the time traces) without altering the LOD levels significantly. Finally, the reagent volume used for the flowing and washing steps on-chip is 10 to 10000 folds smaller than the reagent volume used for ELISA measurements, for sensing and washing steps respectively. With the constant flow rate on-chip, the reagent consumption is less than 50 µl/hour.

Additionally, a summary of comparison between on-chip multiplexed LSPR, ELISA and SPR methods can be found in supporting information (Table S-1).

3.5 Conclusions

In this work, we demonstrated how LSPR sensing integrated with state-of-the-art microfluidics enables to achieve quantitative multiplexed detection of 4 breast cancer protein markers in human serum. This demonstration stands as an important milestone in the field of LSPR sensing and brings us closer to stand-alone and compact automated point of care platforms with a suitable balance between compactness, reliability and sensitivity. In the presented work, miniaturization efforts have been exclusively focused on the sensing chip. Further integration on both the optical measurement and valve controlling set-ups would be required for point of care applications. Additionally, the sensor fabrication costs can be reduced by using mass fabrication methods such as nanoimprinting[100], hole-mask colloidal lithography (HCL) both compatible with microfluidic platforms.[33] The next steps for improvement should involve validation of the platform on clinical samples including direct comparison with gold standard techniques. In order to overcome the complex media effects of clinical samples, either sample dilution or standard addition technique can be implemented.[101] While tested here in the context of medical diagnostics, the proposed scheme is compatible with a wide range of applications. For instance, in the context of drug discovery, it would potentially allow high throughput screening combining very low reagent consumption with access to real-time binding kinetics.[102]

4 PERIODIC SILICON NANORESONATOR ARRAYS FOR ON-CHIP BIOSENSING

The results presented in this chapter as well as part of the text and figures are published in ACS Nano Letters during the course of the PhD program.[103]

Yavas, O.; Svedendahl, M.; Dobosz, P.; Sanz, V.; Quidant, R. On-a-Chip Biosensing Based on All-Dielectric Nanoresonators. Nano Lett. 2017, 17 (7), 4421–4426.

Abstract: Nanophotonics has become a key enabling technology in biomedicine with great promises in early diagnosis and less invasive therapies. In this context, the unique capability of plasmonic noble metal nanoparticles to concentrate light on the nanometer scale has widely contributed to biosensing and enhanced spectroscopy. Recently, high-refractive index dielectric nanostructures featuring low loss resonances have been proposed as a promising alternative to nanoplasmonics, potentially offering better sensing performances along with full compatibility with the microelectronics industry. In this work, we report the first demonstration of biosensing with silicon nanoresonators integrated in state-of-the-art microfluidics. Our lab-on-a-chip platform enables detecting Prostate Specific Antigen (PSA) cancer marker in human serum with a sensitivity that meets clinical needs. These performances are directly compared with its plasmonic counterpart based on gold nanorods. Our work opens new opportunities in the development of future point-of-care devices towards a more personalized healthcare.

The need for point-of-care devices in health and wellness monitoring is one of the principal motivations behind the current development in biosensing. Among the different available transduction schemes, optical biosensors hold the advantage of being highly sensitive, enabling label free and cost effective real time sensing[104]. Beyond silicon-based integrated optics[68,105,106] that shows great promises for sensing, surface plasmon resonance (SPR)[27,107–109] and fiber optics[110,111] based sensors utilizing propagating evanescent waves have been extensively studied and

validated on a wide range of analytes. However, coupling incoming light to the surface modes usually requires sophisticated optics and such sensors are often limited to large bioanalytes, owing to a substantial spatial mismatch of the sensing mode with the tiniest molecules.

These limitations can partially be overcome by using 3D nano-optical resonators. In particular, extensive efforts have been put on localized surface plasmon resonance (LSPR) sensors[73,112,113] which exploit the unique properties of noble metal nanoantennas. The ability to excite LSPR with freely propagating incident light considerably simplifies the optical setup needed for such label free measurements. Highly confined modes also provide strong overlap between the electromagnetic field on the surface and the relevant biological analyte dimensions. Finally, the tiny size of each nanosensors enable their assembly in small foot print sensing areas compatible with parallel multi-detection platforms[73,112,113]. However, plasmonic nanoparticles suffer from dissipative losses in the metal that lead to broad resonances that eventually limit the sensitivity of the sensor read-out. Recently, high refractive index dielectric nanoparticles have been proposed as an attractive alternative to plasmonic nanoparticles in wide range of applications.[13,19]

All-dielectric nanophotonics is a fast progressing field which enables manipulation of both electric and magnetic components of the incoming light. These unique properties open up new opportunities in the field of metamaterials including negative refractive index, cloaking, superlensing and many more.[13,114–118] In practice, light coupling to dielectric subwavelength particles results in the excitation of both magnetic and electric multipole resonances which translates into multiple peaks in their extinction spectrum. Similar to metallic nanoparticles, the resonance frequencies depend on their geometry, constitutive material and the dielectric environment. Their sensitivity to the surrounding dielectric permittivity along with their strong mode localization suggests high index dielectric nanoparticles could perform well as biosensing transducers.[19,18,40,119] Silicon nanoresonators, with resonances in visible-NIR spectral range, were first studied theoretically and more recently measured experimentally[21,120–123]. The use of silicon is motivated by its compatibility with the microelectronics industry, high material abundance and low cost. While it has recently been suggested that Si nanoresonators could benefit to the detection of biological molecules, so far, only bulk refractive index sensing measurements[18,40,119] and biotin-streptavidin binding responses have been reported.[20,39]

In this chapter, we demonstrate that Si nanoresonator arrays integrated with state-of-the-art microfluidics result in an efficient sensing platform for the detection of protein cancer markers in human serum, at clinically relevant

concentrations for cancer screening. We first study the optimal structural design of Si nanodisks for molecular sensing. Then, we demonstrate detection of PSA (prostate specific antigen) in buffer with a limit of detection (LOD) that is comparable to gold standard immunoassay techniques. Finally, to validate its operation in clinical conditions, the platform is tested in human serum. To the best of our knowledge, this is the first report combining silicon nanoresonators and microfluidics to perform clinically relevant immunoassays.

4.1 Detection chip

Our platform consists of silicon nanodisk arrays on a quartz substrate integrated with a PDMS microfluidic chip including micromechanical valves (Figure 4-1). We fabricate the silicon nanodisk arrays using standard negative resist e-beam lithography followed by a reactive ion etching step on commercial amorphous silicon coated quartz samples (see Chapter 2). The nanodisk arrays have a fixed height *h*=50 nm. We choose to tune the disk radius *r* and inter-particle distance *s* to assess the optimum nanosensor parameters. The extinction spectra of the nanodisk arrays are measured using our homemade transmission microscopy set-up[34]. Our optical detection enables us to interrogate up to 32 regions in parallel throughout the chip for real-time resonance tracking of different sensor arrays as described in previous chapters.

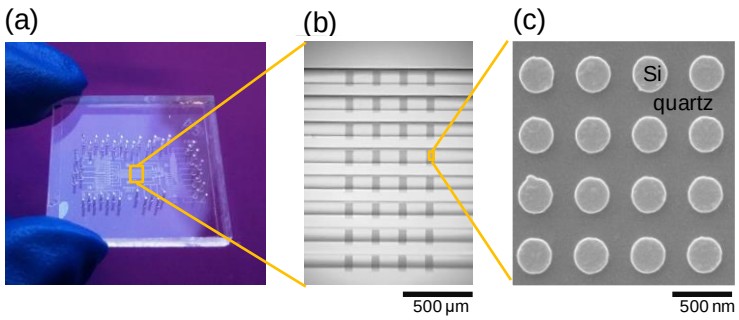

Figure 4-1 The sensing chip with 32 arrays. (a) Picture of an assembled chip with 8 sensing channels. (b) Close-up picture of the 8 sensing channels showing silicon nanodisk arrays with different parameters. (c) SEM micrograph of a small portion of a silicon nanodisk array with h=50nm, r=140 nm and s=200 nm.

The PDMS chip is fabricated by multilayer soft lithography (see Chapter 2) leading to 8 sensing channels that are all individually and simultaneously addressable.[34] The sample flow on the experiment channels is controlled by the micromechanical valves.[46] The map of flow and control channel networks are shown in Figure 4-2 in blue and red, respectively. A common reagent can be flown in all sensing channels through a common inlet (labeled yellow), or individual samples can be flown through different sensing channels through the individual inlet (labeled green). This enables the sandwich assay formation steps for a full calibration curve with 8 different concentrations. Unlabeled blue channels are the outlets of the chip.

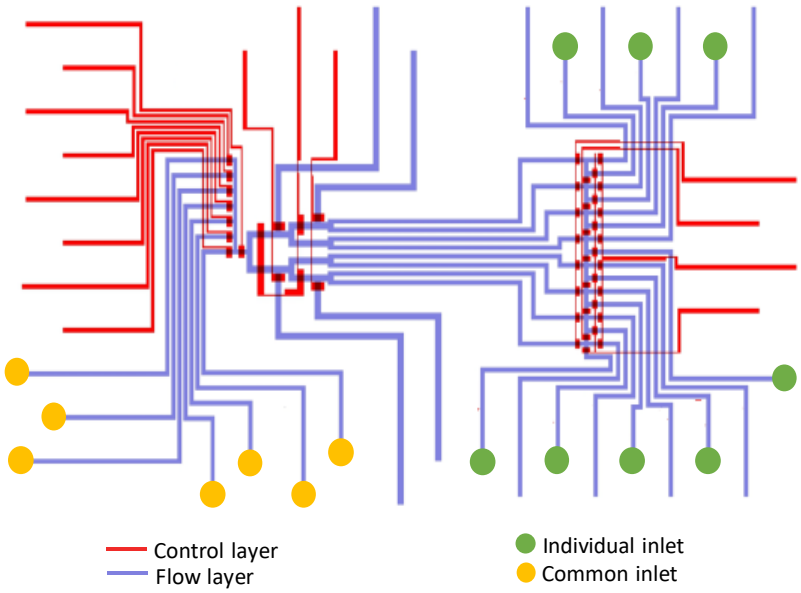

Figure 4-2 The microfluidic flow (blue) and control (red) channel network with 8 sensing channels. The fluids can be flown into all the 8 channels through a common inlet (yellow), or individually through individual inlets (green). Unlabelled blue channels are the waste outlets of the chip.

The detection of the biomolecules is based on a standard sandwich assay scheme. The capture antibody is immobilized on the silicon sensors by passive adsorption similarly to ELISA and other immunoassay techniques.[124] The details of the sensing protocol will be explained in the following sections. Figure 4-3 schematically summarizes the sensing steps with the corresponding real-time resonance shifts.

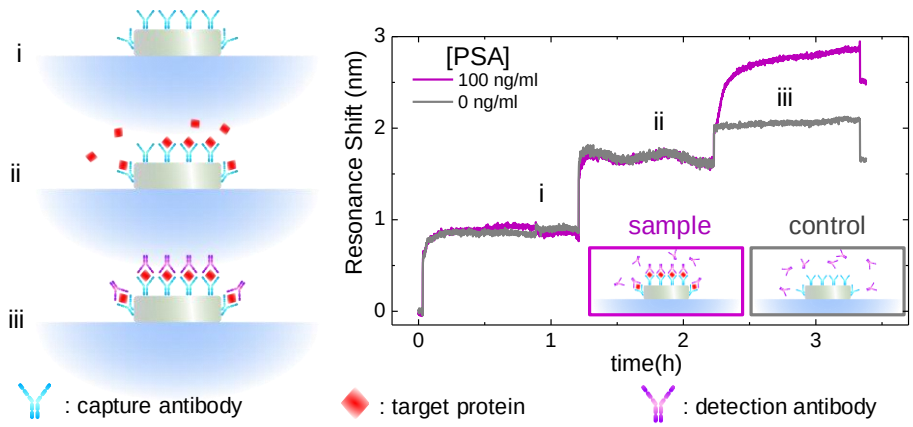

Figure 4-3 Schematics of the sensing protocol (left) and the evolution of the nanodisk resonance during the different steps of the sandwich assay (right). The sample (100 ng/ml PSA) and control (no PSA) experiments are in grey and purple, respectively.

4.2 Optical characterization

The extinction spectrum of individual *h*=50 nm Si nanodisks is mainly dominated by their electric dipole resonance (See Finite Element Method (FEM) simuations in Figure 4-4).[21,125] Here, for sensing purposes, we aim at exploiting the strong collective resonance arising from coherent far field dipole coupling due to the periodicities of the arrays. These diffractive modes only arise when each individual particle support an electric dipole resonance.[121] The array resonance is optimized by changing the disk radius (*r*) and separation (*s*). Figure 4-5 shows the measured extinction spectra of the different arrays along with the corresponding Finite Element Method (FEM) simulations. The resonances are tuned by changing the periodicity at fixed radius (Figure 4-5a), or conversely, changing the nanodisk radius at constant disk separation (Figure 4-5c). The corresponding FEM simulations on infinitely large arrays are in good agreement with the measured data (Figure 4-5 b and d). The amplitude and width of each of these resonances vary for different nanodisk arrays. While these properties are important for the detectability of spectral shifts, also the refractive index sensitivity is expected to vary with the array parameters.

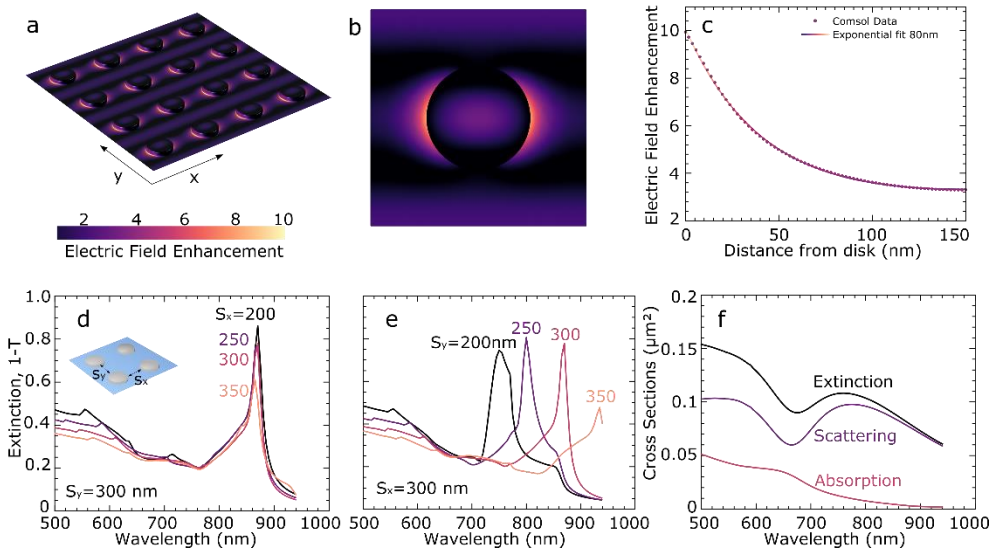

Figure 4-4 FEM Simulations of infinite Si nanodisk arrays. Electric field enhancement (a) on the nanodisk and glass surface, plotted in a periodic manner to visualize the interparticle couplings, and (b) in a cross section of one unit cell, 25 nm from the glass surface. (c) The near field exponential decay by the distance from the nanodisk in the x-direction. The nanodisk array was placed on a glass/water interface with parameters r=140 nm and s=300 nm. (d) The extinction spectra of the nanodisk arrays with varying periodicity in x-direction with fixed nanodisk separation in y-direction (S_y=300 nm). (e) The extinction spectra of the nanodisk arrays with varying periodicity in y-direction with fixed nanodisk separation in x-direction (S_x=300 nm). (f) Single particle extinction, scattering and absorption spectra for r=140 nm and h=50 nm disk.

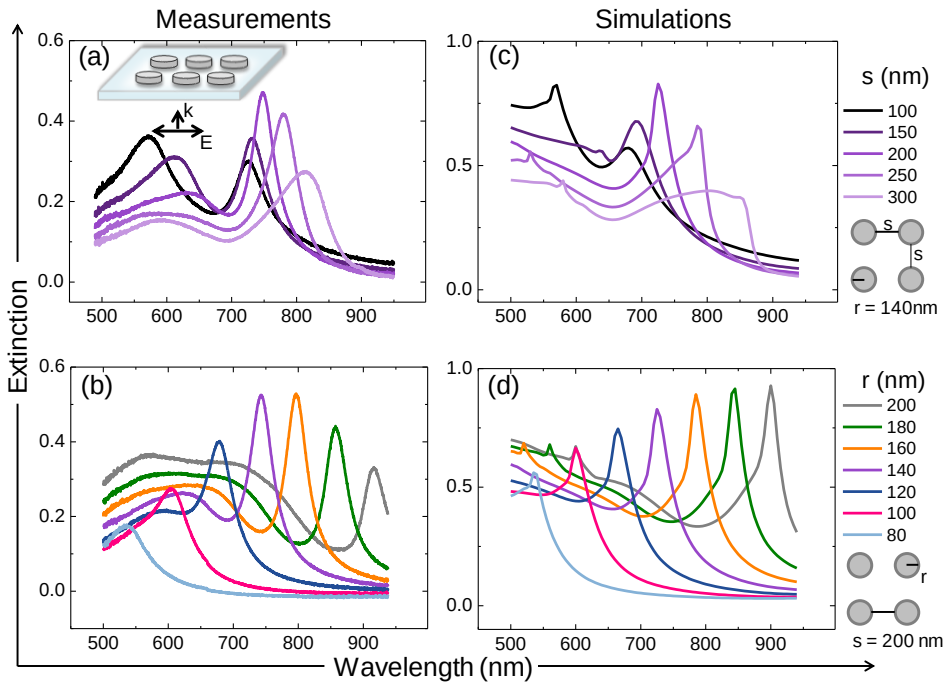

Figure 4-5 Resonance tuning of Si-nanodisk arrays. Experimental extinction spectra of silicon nanodisk arrays in air: (a) Influence of the disk separations at fixed radius r=140 nm and (b) Influence of the disk radius at fixed disk separation of s=200 nm. (c, d) Corresponding FEM simulations. Inset in (a) shows the geometry of the disks and the incident light polarization.

4.3 Bulk refractive index sensitivity characterization

In order to identify the structural parameters (*r* and *s*) that provide the highest sensitivity to the surrounding media we performed bulk refractive index sensitivity (BRIS) experiments. In these experiments, we fabricated sensor arrays with 4 different radii (*r*=120, 140, 160 and 180 nm) and with disk separations varying from 100 nm to 450 nm with 50 nm increments. Once integrated to the microfluidics, the fabricated sensor arrays are exposed to increasing concentrations of glucose solutions in ultra-pure water (Figure 4-6a).

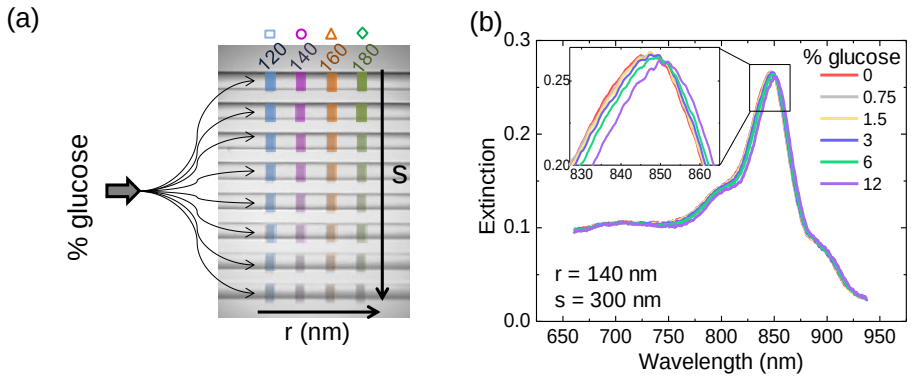

Figure 4-6 Bulk refractive index sensitivity (BRIS). (a) Schematics of the BRIS experiment in which the 8 microfluidic channels are used to flow different water/glucose mixtures on Si nanodisk arrays with different s and r. (b) Evolution of the extinction spectra of a nanodisk array (r=140 nm, s=300 nm) exposed to 6 different glucose-water mixtures.

For illustration, Figure 4-6b shows the resulting redshift in the extinction spectra for *r*=140 nm and *s*=300 nm. Our automated parallel acquisition enables us to track in real time the spectrum of each of the different arrays on the chip and extract the corresponding shifts in the main peak centroid. Figure 4-7 shows the peak and centroid shifts of two sets of sensors where different glucose concentrations are flowed in the channels sequentially with a step of washing with water in between. We observe instantaneous shifts as the refractive index of the surrounding media changes. The redshifted signal returns back to the baseline value for the washing steps with water ensuring that there is no irreversible modification of the sensors and the shifts are indeed due to bulk refractive index changes. For asymmetric extinction peaks like the one considered here, peak centroid tracking was found to be more sensitive than standard peak tracking (Figure 4-7).[26]

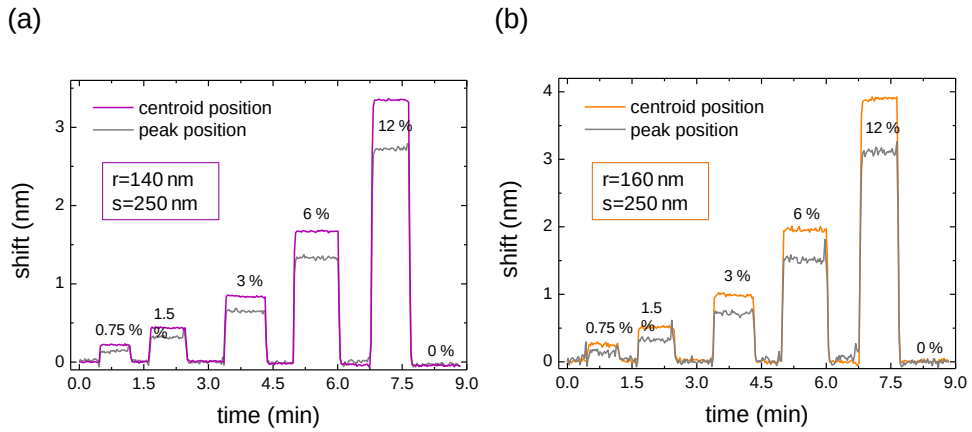

Figure 4-7 Comparison of the shifts of the centroid and peak positions of the resonances. Real-time centroid and peak position shifts of the resonances due to changing bulk refractive index of the surrounding media (glucose percentage concentrations) for (a) r=140 nm and s=250 nm and (b) r=160 nm and s=250 nm nanodisk arrays. The shifts of the peak positions (grey lines in both plots), are slightly lower than the shifts of the centroid positions.

Figure 4-8 shows the evolution of the solution of the peak centroid with the refractive index for r=140 nm and s=300 nm nanodisk array. From the slope of the linear fit we extract the bulk refractive index sensitivity (BRIS) of the sensor. Figure 4-9 shows the centroid shifts of all the different arrays fabricated on the same chip. The BRIS values for sensors with different disk separation and radius are gathered in Figure 4-10. The arrays with separations larger than 300 nm were not considered as they either exhibit very low extinction, due to a low particle density, or resonances that were out of the spectral range of our set-up. Within the considered parameter range, we found that the BRIS values increased with increasing nanodisk separations. The highest BRIS value, 227 nm/RIU, was measured for the array with *r*=140 nm and *s*=300 nm featuring a resonance centered at 844nm with a quality factor of 20. Despite the simplicity of our structure, this BRIS value is only slightly lower than the previously reported BRIS values of more complex silicon nanostructure arrangements.[40,119]

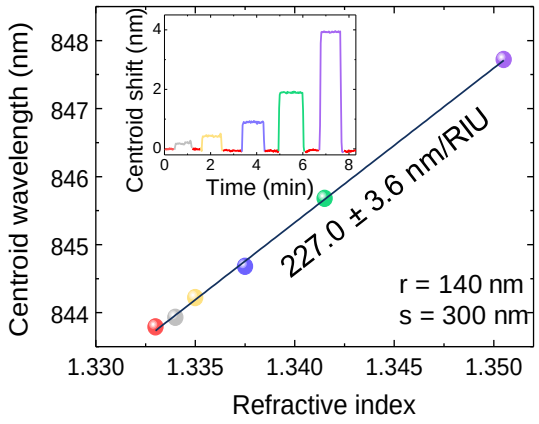

Figure 4-8 BRIS of the Si nanodisk array with r=140, s=300 nm. The centroid positions extracted from the extinction spectra in Figure 4-6b as a function of the refractive index of the glucose solutions. The inset is the real time centroid shifts during the sequential flow of varying glucose concentrations separated by rinsing step.

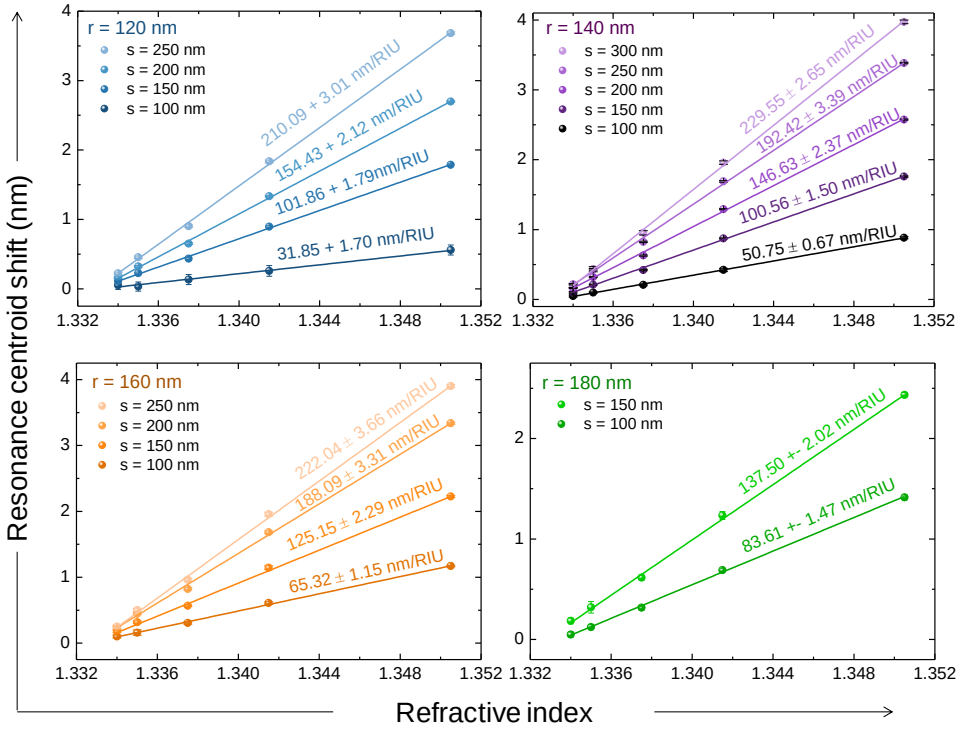

Figure 4-9 The BRIS measurements for all the presented arrays with varying radius r, and nanodisk separation s.

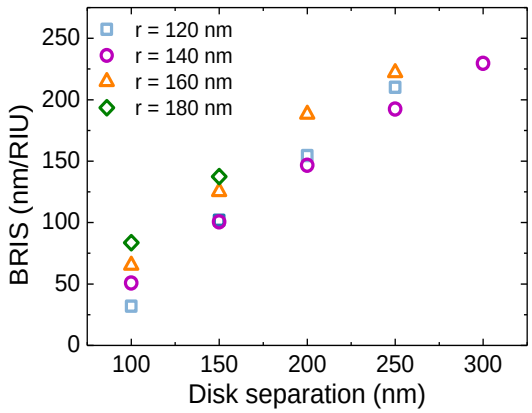

Figure 4-10 Summary of the BRIS values obtained for different arrays with different radii and disk separations from Figure 4-9. The error bars are smaller than the data points in the plot.

4.4 Cancer marker detection

4.4.1 Detection in PBS-BSA buffer

For the target analyte sensing proof of concept experiments, we selected the two sensors exhibiting the highest BRIS values (with radii of 140 and 160 nm and disk separations of 300 and 250 nm, respectively). The experiment consists of flowing different concentrations of the target molecule in each of the individual channels in order to obtain an 8-point calibration curve. We here focused on the detection of Prostate Specific Antigen (PSA). PSA is a 34 kDa protein whose high concentration in blood (greater than 4-10 ng/ml) can be associated to prostate cancer or other prostate disorders.[126,127]

For the detection of PSA, the capture antibody is first immobilized on the sensor surface by passive adsorption by flowing the antibody solution in phosphate buffer through all 8 channels. The sensors were first flushed with 10 mM phosphate buffer (PB) in order to have a base for tracking the shifts of the monoclonal antibody (mAb) (BiosPacific, A45160) for PSA which was introduced to the channels in 10 mM PB through a common inlet so that the solution flowed through all the channels simultaneously and all the sensors were coated with the capture

antibody. Once the capture antibody layer was formed, the resonance shift signal saturated and the channels were then washed with PB shortly to remove the excess unbound antibodies. The signal saturated after only 15 mins after 150 µg/ml mAb solution was introduced to the sensors. The binding kinetics and the saturation time depend on the mAb concentration used.

For the proof of concept experiments we have measured the PSA calibration curve in phosphate buffer saline (PBS) with 1% bovine serum albumin (BSA). The BSA was added to the PBS as a blocking agent to prevent the unspecific binding and also to mimic the human serum proteins in this preliminary measurement. The 7 PSA calibration concentrations were prepared and introduced to different sensors through individual inlets of each channel. The 8th channel was used as a control channel with no PSA added in the buffer.

For the target proteins that are small in size compared to antibodies, the shift due to different concentrations of these proteins is not easy to detect directly. For the signal amplification, we used an amplification antibody that recognizes the target protein. For our measurements with PSA, polyclonal antibody (pAb) (BiosPacific, D63010) for PSA was used for this purpose. 100 µg/ml pAb in PBS with 1% BSA was introduced in the channels through common inlets after a short washing step with buffer. After the pAb binding signal was saturated, the channels were again washed with buffer to remove unbound antibodies and to eliminate the bulk refractive index effect due to free pAb solution in the channels. This way the absolute effect of pAb binding on the sensor area was measured. The centroid shifts due to the absolute pAb binding step were extracted to plot the calibration curves presented in this work.

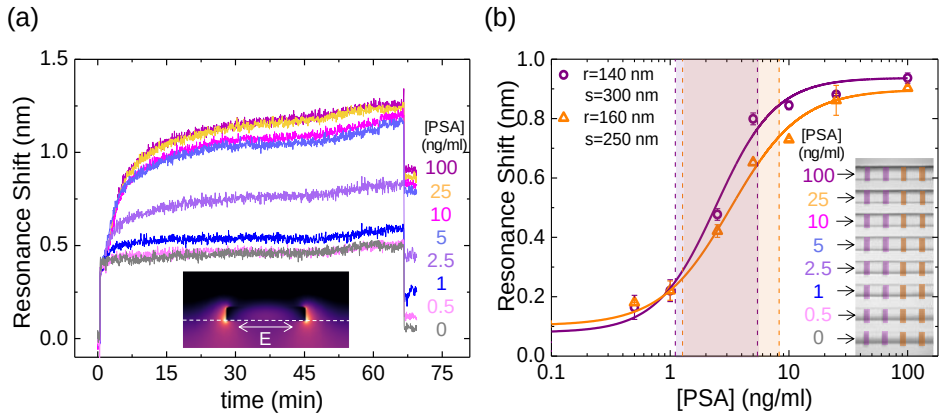

Figure 4-11 Cancer marker sensing in PBS. (a) Real time resonance shifts of the silicon NC arrays (r=140nm, s=300nm) due to the detection of different concentration of PSA. The inset shows the calculated near field distribution for one nanodisk from an infinite array. The white dashed line

indicates the substrate-NC interface. (b) Calibration curves for PSA in PBS buffer with 1% BSA obtained using two different sensor arrays on the same chip (inset is a diagram showing the sensor organization in the channels). The shaded areas on the calibration curves represent the dynamic ranges of the curves (purple: r=140 nm, s=300 nm array, orange: r=160 nm, s=250 nm array). The error bars indicate the standard deviation of the 2 parallel measurements on the same chip.

Figure 4-11a shows the real time recorded shifts of the sensors with radius of 140 nm and separation of 300 nm in the detection step. The channels are washed with PBS to remove unbound detection antibodies and reduce the bulk refractive index effect. This washing step is also seen in Figure 4-11a, as a drop of signal after the detection antibody binding curves have reached the plateau. The final shifts after the washing step are extracted to obtain the calibration curves for PSA (Figure 4-11b). The standard curves were fitted using a four-parameter logistic equation. The analytical parameters of the sandwich assay are shown in Table 3.

The dynamic ranges of the sensors are shown by the shaded areas on the calibration curves which cover the clinically relevant range for both of the sensors. The limit of detection (LOD, estimated as the conventional IC_{10} value of the four-parameter logistic curve fit) for both sensors are beyond the cut-off concentration for patients. The LOD for *r*=140 nm and *r*=160 nm sensors are around 0.69 ng/ml and 0.74 ng/ml, respectively. The sensitivity of a sensor is conventionally defined as the IC_{50} value of the calibration curve which is found to be 2.45 ng/ml and 3.24 ng/ml, respectively. We find that the sensors with higher BRIS (*r*=140 nm, *s*=300 nm) led to calibration curves with slightly better sensitivity and lower LOD values with a higher slope of the dynamic range of the sensors (Table 3). The error bars are representing the signal variations between the replicas on the same chip and the relative standard deviation for intrachip reproducibility is found to be varying between 0.5% and 5.1% for the working range of the sensors.

4.4.2 Detection in human serum

To demonstrate the clinical relevance of our sensing platform, we performed the PSA calibration curve measurements in human serum (Fig. 4c). Serum was diluted at 50% in PBS in order to reduce the matrix effects. The LOD (IC_{10}) is 1.6 ng/ml which is below the cut-off value of the PSA concentration in patients and the dynamic range is between 2.5 ng/ml and 16.0 ng/ml which covers the clinically relevant range for cancer screening. Further details about the analysis of the calibration curve can be found in Table 3. This result suggests that the sensor performance is within the clinically relevant range and the measurements are feasible even in a complex matrix such as human serum. Very low shifts of the control channel (0.005 ± 0.035 nm) indicates negligible unspecific signal.

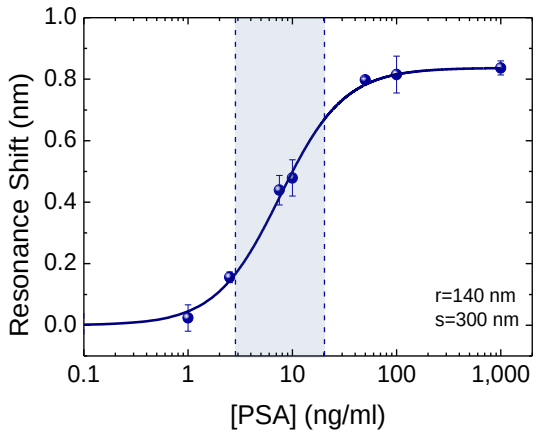

Figure 4-12 PSA calibration curve obtained in 50% diluted human serum for sensor with r=140 nm and s=300 nm. The shaded area defines the dynamic range and the error bars are the standard deviations of the 4 different measurements on the same chip.

4.4.3 Effect of molecular adsorption on the substrate

Passive adsorption of the capture antibody layer on the sensors clearly enables faster experiments compared to the LSPR sensing where the sensor surface needs to be functionalized and activated (See Chapter 2 and 3). However, Si sensors on quartz substrates are prone to adsorption of molecules on the substrate as well as the sensors. Our preliminary tests with our substrates for passive adsorption of capture antibodies showed us that the antibodies bind to the substrate surface when they are dropcasted and incubated. This was a non-quantitative test where we immobilized an antibody with gold nanoparticle (1.4nm) attached to it on the substrate by dropcasting reagents by a pipette and finally used silver enhancement method[128] to observe the color change on the surface. Figure 4-13 shows the photographs of the tested substrates. In Figure 4-13b and c untreated quartz and Si surfaces are tested with different buffers for antibody carrier solution. This off-chip tests showed that the antibodies are absorbed both on silicon and quartz substrates. In Figure 4-13d and e we have quickly tested the epoxy coating protocol for antibody immobilization on Si surface as described in literature.[83] At this stage, it was important to test if the epoxy coating will survive the baking step for chip assembly step, therefore we checked non-baked and baked (10h at 50C) Si surfaces separately. The antibodies were immobilized in both cases. Epoxy coating might have enhanced the antibody binding to the Si surface, however we have decided to work with passive adsorption method, as it is simpler, faster and still

yields good antibody coverage of the surface with PB based solutions which is the common buffer we use in all our experiments.

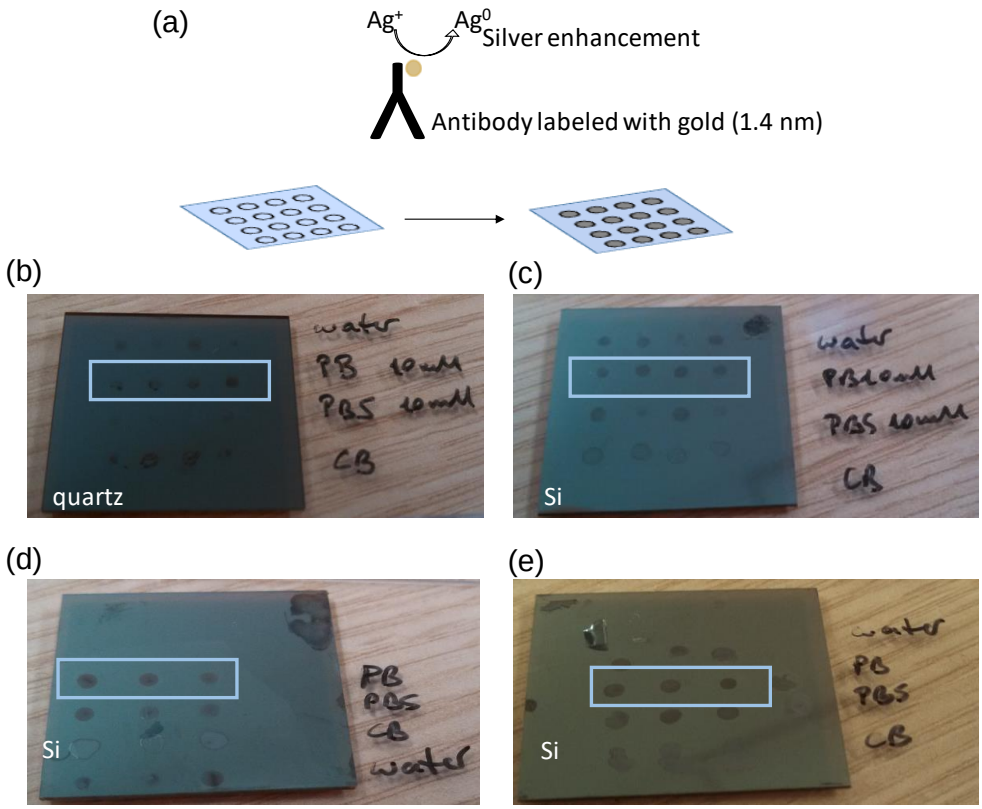

Figure 4-13 Off-chip test for antibody immobilization on quartz and silicon. (a) tbe silver enhancement method schematically explained. Test for immobilization of antibodies in different buffer solutions as labelled (water, 10mM Phosphate Buffer (PB) with pH 7.5, 10mM PBS with pH 7.5, 50 mM Carbonate Buffer (CB) with pH 9.6) on (b) untreated quartz surface (passive adsorption) (c) untreated Si surface (passive adsorption), (d) non-baked epoxy coated Si surface and (d) baked epoxy coated Si surface. The blue rectangle marks the tests performed with PB.

To understand the actual effect of molecular adsorption on the substrate, we did FEM simulations and compared the two cases where the molecules are adsorbed only on sensors, and on substrates along with the sensors. Figure 4-14 demonstrates the effect of moleculer absorption on sensor and substrates. According to these results the shifts observed for the case where the substrate is coated along with sensors are higher than only the sensors. This matches also with the amount of shifts observed in our experiments for 5-10 nm of expected capture antibody coating during the immobilization step (Figure 4-3) suggesting that the capture antibody is also absorbed by the substrate in our experiments.

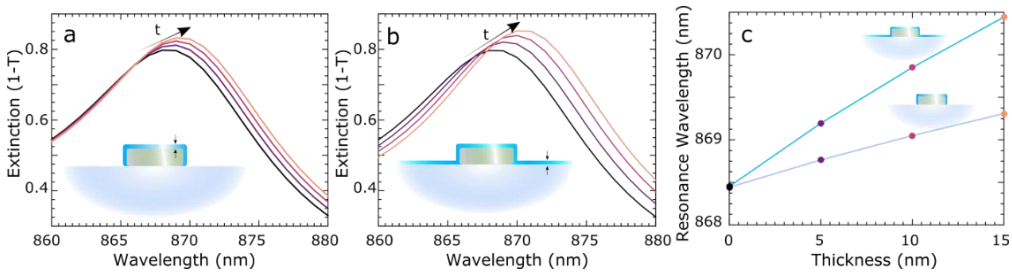

Figure 4-14 Simulated effect of molecule adsorption on the substrate. Extinction spectra from FEM simulations of a nanodisk array when a layer of thickness t and refractive index n=1.45 is placed (a) only on the nanodisk, and (b) on the nanodisk and on the glass. (c) The corresponding resonance positions as a function of layer thickness. The nanodisk arrays were placed on a glass/water interface with r=140 nm and s=300 nm. These results suggest that the primary antibodies might adsorb not only on the Si, but also on the glass surface.

This observation brings up the discussion about the unspecific signal during biomolecule detection experiments. Unselective adsorption of molecules on the sensor and substrate surface might result in unreliable results due to unspecific binding signals. However, as stated in the previous section, the resonance shifts observed in the control channel is very low and suggests no unspecific signal. High surface coverage with capture abs or competition between adsorption and antibody antigen affinity.

4.5 Comparison of Si nanodisk arrays with LSPR sensors

In order to compare the sensing performance of our silicon nanoresonators with their plasmonic counterparts[73,112,113], we repeated the on-chip PSA calibration curve experiment with the gold nanorod array studied in the previous chapter (Chapter 3) and in our previous work[34,59]. The only significant experimental difference comes from the use of EDC/NHS based surface chemistry prior to antibody immobilization on gold. Otherwise, both measurements were performed under the same conditions, such as antibody concentrations, buffers and similar flow times.

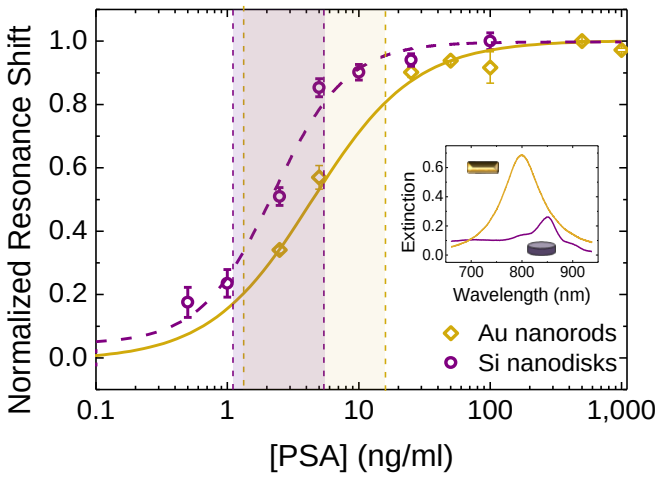

Figure 4-15 Comparison of the Si and Au platforms. PSA calibration curves for gold nanorod arrays (gold) and silicon nanodisk arrays (purple). Both curves were normalized for clearer comparison. The error bars represent the standard deviation of 2 parallel measurements on the same chip. The shaded areas are the respective dynamic ranges. The inset shows the experimental extinction spectra of gold nanorod arrays and silicon nanodisk arrays.

The normalized PSA calibration curves for the gold nanorods (100 nm x 200 nm) and the silicon nanodisks (*r*=140 nm, *s*=300 nm) are compared in Figure 4-15. The analytical parameters of the sandwich assay on both sensors can be found in Table 3. The LOD (IC_{10}) of the gold sensors is found to be around 0.87 ng/ml which is slightly higher than the LOD of the silicon based sensors. Conversely, the dynamic range of the LSPR-based sensors is broader for higher concentrations, giving a lower slope, which leads to higher limit of quantification. Besides, the assay time was much shorter for silicon based sensors since the LSPR sensing protocol requires self-assembled monolayer preparation and activation as well as blocking steps using ethanolamine (Figure 4-16).

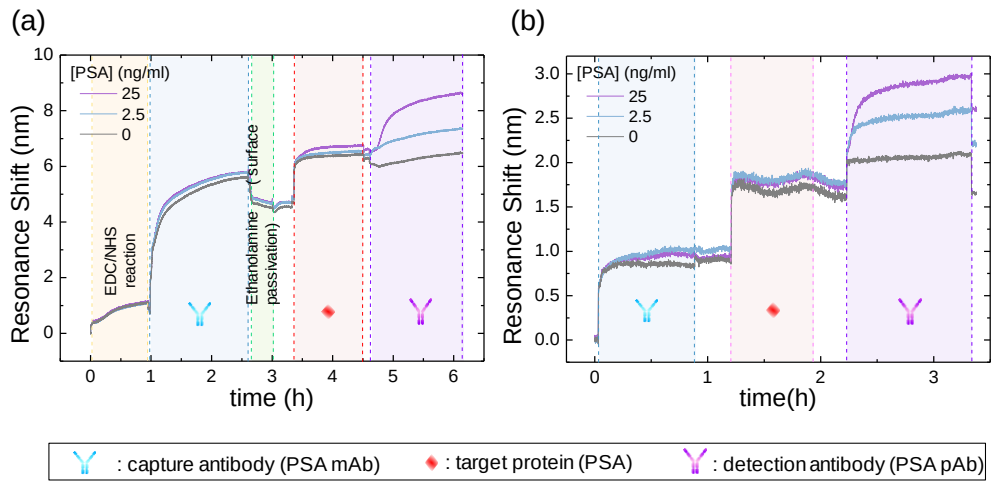

Figure 4-16 Comparison of LSPR and silicon nanoresonator based biosensing experiments. The real-time measurement of PSA sensing experiment in PBS with 1% BSA for (a) gold nanorod based LSPR sensors (b) silicon nanodisk sensors. The shaded areas in both plots represent the corresponding assay steps. The non-shaded time intervals correspond to the washing steps with buffers as explained in the previous sections.

Sensor Array (h=50nm)	Buffer/matrix	LOD (IC_{10}) (ng/ml)	Sensitivity (IC_{50}) (ng/ml)	Dynamic Range (ng/ml)	r^2
Silicon nanodisks r=140nm, s=300	50% human serum	1.60	7.59	2.85 - 20.27	0.9973
Silicon nanodisks r=140nm, s=300	PBS + 1% BSA	0.69	2.45	1.10 - 5.43	0.9891
Silicon nanodisks r=160nm, s=250	PBS + 1% BSA	0.74	3.24	1.27 - 8.27	0.9987
Gold nanorods (200 nm x 100 nm)	PBS + 1% BSA	0.87	4.41	1.33 - 15.96	0.9980

Table 3 Analytical features for PSA sandwich assay on different sensors with different matrix.

4.6 Conclusions

We have studied the use of silicon nanoresonators integrated in a state-of-the-art microfluidic architecture for biosensing. We demonstrated that the resulting

platform is compatible with detection of small biomolecules in complex matrices for clinical applications. The reported sensing performance enables us to detect clinically relevant concentrations of PSA.

We have also compared our platform with a well-developed LSPR-based sensing protocol and shown that the sensitivity, LOD and the dynamic ranges are comparable. (i) Besides the similar sensing performance, one of the advantages of the silicon based sensors is the significantly longer decay length of the surface field over LSPR modes in metal nanoantennas (Figure S1), which can be beneficial for multilayer assays involving detection of molecules relatively far from the surface. This suggests that in comparison with LSPR sensors, different assay types with multiple layers of antibodies can be efficiently monitored using the silicon nanoresonators which in practice enables more practical and faster detection of the target analyte. (ii) While the extinction resonance of the Si nanoresonators considered here is much weaker compared to gold nanoantennas (inset Figure 4-15), its quality factor is substantially higher (20 versus 10). We foresee further engineering of the Si nanoresonators including arrangement in dimers and oligomers could improve the sensing performance. (iii) While the location of the adsorbed antibodies is not controlled in the present study, a Si-selective surface chemistry is foreseen to compare the sensor performance. (iv) It is also noteworthy mentioning that Si nanoresonators feature higher stability in solution compared to their gold counterparts. While gold requires stabilization with a passivation layer (*e. g.* using mercaptoundecanoic acid), we did not observe any significant degradation of bare Si cylinders, even after long time exposure to both water and buffer. (v) Finally, the quality of the sandwich assay, hence the LOD and sensitivity, can further be improved by additional optimizations of the capture and detection antibody concentrations.

5 SEMI-RANDOM SILICON NANORESONATOR ARRAYS FOR BIOSENSING

The results presented in this chapter as well as part of the text and figures are published in ACS Nano during the writing of the PhD thesis.[129]

Yavas, O.; Svedendahl, M.; Quidant, R. Unravelling the role of electric and magnetic dipoles in biosensing with Si nanoresonators. ACS Nano 2019, 13 (4), pp 4582–4588.

Abstract: High refractive index dielectric nanoresonators are attracting much attention due to their ability to control both electric and magnetic components of light. Combining confined modes with reduced absorption losses, they have recently been proposed as an alternative to nanoplasmonic biosensors. In this context, we study the use of semi-random silicon nanocylinder arrays, fabricated with simple and scalable colloidal lithography for the efficient and reliable detection of biomolecules in biological samples. Remarkably, electric and magnetic dipole resonances are associated to two different transduction mechanisms: resonance redshift and extinction decrease. By contrasting both observables, we identify clear advantages in tracking changes in the extinction magnitude. Our data suggest that, despite its simplicity, the proposed platform is able to detect prostate specific antigen (PSA) in human serum with limits of detection meeting clinical needs.

In the previous chapter, for an on-chip biosensing platform, we have focused on periodic Si nanodisk arrays of 50 nm height, where the main resonance modes were the bragg diffraction modes and electric dipole excitations of the silicon nanodisks and performed real-time detection of cancer biomarkers in human serum.[103] While at that stage, Si-based nano-optical sensors have already reached comparable performances to LSPR counterparts, further developments are required to fully exploit their potential. In particular, there is a need to further understand how the control over both electric and magnetic dipoles could benefit

the detection sensitivity. Furthermore, especially within the context of point-of-care applications, one needs to identify cost effective strategies to fabricate high refractive index dielectric nanoresonators (HRDN) sensors over large areas.

In this chapter, we present a novel platform which contributes to both objectives. A semi-random array of silicon nanocylinders (Si-NCs), fabricated by low-cost and scalable colloidal lithography, is integrated into a microfluidic environment to perform prostate specific antigen (PSA) detection through two different transduction mechanisms: resonance redshift and extinction reduction. Remarkably, we find these observables are associated to electric and magnetic dipole resonances, respectively. Through real-time tracking of both signals, we demonstrate that extinction reduction leads to better sensing performances.

5.1 Semi-random Si-NC arrays

Our sensing chip consists of a semi-random array of Si-NCs integrated into a microfluidic environment. Similar arrays have previously been used in various LSPR biosensing schemes.[130–134] In order to achieve fast, cheap and large-scale fabrication, we used colloidal lithography and fabricated semi-randomly distributed Si-NC of height of 130 nm and radius of 140 nm with electric and magnetic dipole resonance at 900 nm in aqueous environment (Figure 5-1). We first coated the Si-on-quartz substrates with a 50 nm gold layer. Then, we drop-casted the sulfate latex beads which are charged and therefore repel each other and form a semi-random array, that is, without any long-range order but with a typical nearest neighbour distance.[135] We used them as a reactive ion etching mask for etching the gold layer in RIE chamber. Next, we removed them by an adhesive tape and used the patterned gold mask for etching the silicon layer with RIE. Finally, we cleaned the substrate by piranha solution, which removed the gold mask layer by etching away the Ti layer below (see Chapter 2 for the detailed fabrication protocol).

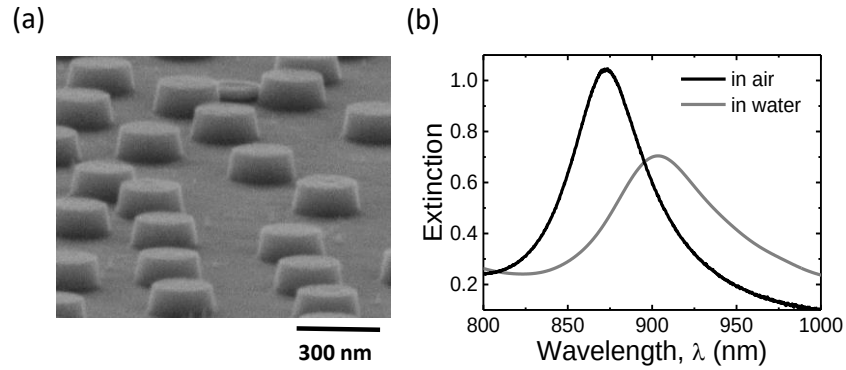

Figure 5-1 Semi-random Si NC arrays. (a) SEM image of the Si-NCs on quartz. (e) The measured extinction spectra of the silicon NCs in air (black) and in water (grey).

The SEM image of the semi-randomly distributed Si-NCs are shown in Figure 5-1a. With this EBL-free method, the whole sample area can be patterned with nanostructures simultaneously without altering the fabrication time or cost. The areas on the substrate to be patterned can be selected by tape stripping the beads away before using them as an etch mask. More precise bead stripping method is described by Acimovic *et. al* for patterning the sample surface with precision of few micrometers by using a homemade PDMS stripping tape.[33] For our sensing device, we tape stripped the edges of the sample, leaving the NCs only at the central region of 0.5 cm^2 on the chip.

The extinction spectra of the semi-random Si-NC array measured in air and in water are shown in Figure 5-1b. The resonance position in air and in water was 870 and 900 nm, respectively, showing a clear redshift due to the large refractive index change of the local environment. Furthermore, the extinction amplitude is reduced in water compared to the spectrum in air, which is in-line with previous reports.[17,20,120]

To test the sensing performance of the fabricated Si-NC arrays, we integrated it with a multilayer microfluidic network of PDMS,[34] which enables the control of the sample flow on the sensing regions that are separated by microfluidic channels (Figure 5-2). The microfluidic chip design and the operation principles, as well as the fabrication procedure are described in the previous chapters. This configuration is crucial for rapid and practical execution of complex immunoassay steps in a highly controlled environment.

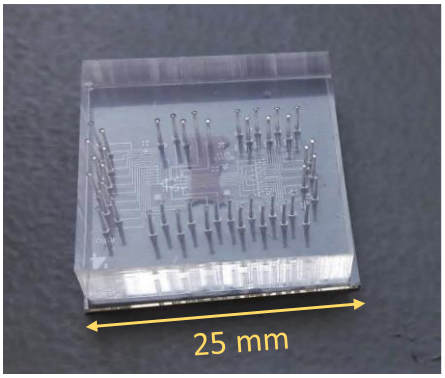

Figure 5-2 The integrated chip. The sensor area is visible as a darker area on the substrate under the PDMS microfluidic channels.

5.2 Bulk refractive index sensitivity and transduction mechanisms

Initially, we evaluated the bulk refractive index sensitivity (BRIS) of the Si-NCs by sequentially flowing different percentage glucose solutions through the channels and tracking the centroid position and the extinction amplitude. The centroid shift of the extinction peak with respect to the refractive index of the glucose solution is shown in Figure 5-3a-b. The semi-random Si-NC arrays exhibited a BRIS of 86 nm/RIU by the conventional centroid tracking method. Previously, the BRIS of periodic silicon nanodisk arrays of 50 nm height was reported to be 227 nm/RIU, exhibiting much higher BRIS value, due to enhancement of sensitivity by the diffractive modes induced by the periodicity.[103]

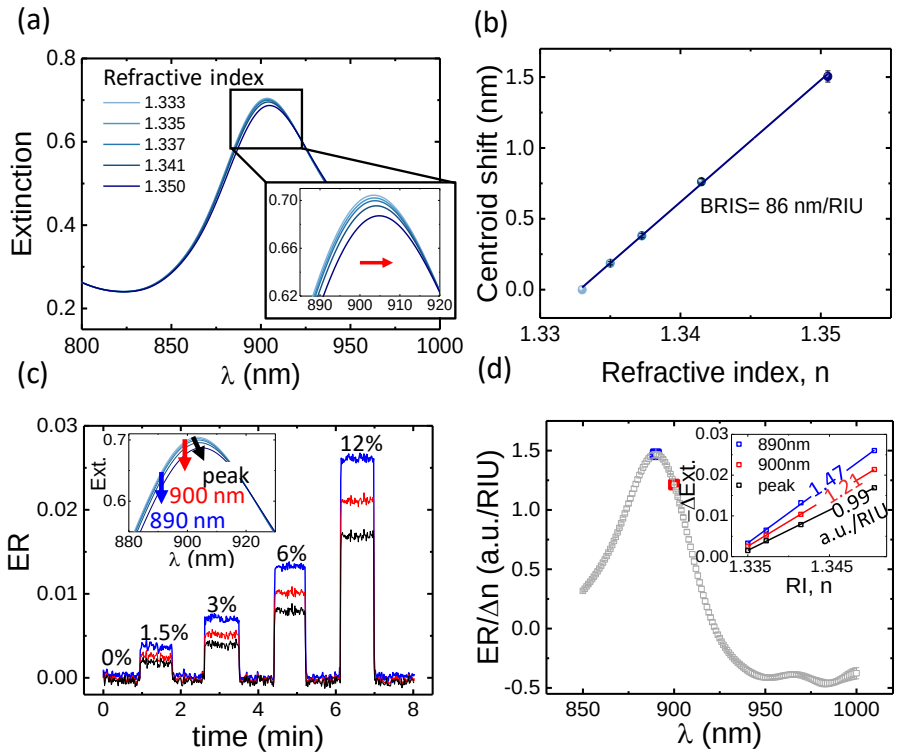

Figure 5-3 Bulk refractive index sensing experiments with semi-random Si-NC arrays. The two different transduction mechanisms analysed. (a) The extinction spectra of the sensors in glucose solutions of varying concentrations. (b) The respective centroid shifts from (a). The slope of the linear response of centroid position to changing refractive index is the BRIS. (c) The real time traces of the extinction amplitude response to changing refractive index by sequential flow of different percentage glucose concentrations. The inset shows the wavelength positions the three measurements: the peak wavelength (black line), at 900 nm (red line) and at 890 nm (blue line). (d) The extinction reduction sensitivity as a function of wavelength. The extinction reduction (ER) is the negative change of extinction signal with respect to the refractive index. The highest sensitivity was reached at 890 nm (blue). The change in extinction with respect to the refractive index, n, of the surrounding medium is shown in the inset for 890 nm, 900 nm and at the peak position of the extinction.

In addition to the centroid shift, we notice that the extinction is reduced while increasing the surrounding refractive index, as seen in Figure 5-3a. Based on this observation, we evaluate the sensing performance of our sensors by tracking the extinction reduction in Figure 5-3c-d. We define extinction reduction as the negative change in the extinction signal. In Figure 5-3c, the real-time response of the extinction amplitude to the sequential flow of the distinct glucose concentrations, with washing steps in between, is presented for three different cases. We have tracked the extinction amplitude change at the peak maxima, at 900 nm and at 890 nm, which was found to exhibit the highest extinction reduction sensitivity. The whole wavelength range scanned for the maximum

extinction reduction sensitivity is shown in Figure 5-3d. These results suggest that the optical platform could be rearranged to detect only the transmission amplitude instead of the full spectra, in order to perform biosensing in a cheaper and simpler way.

To back up our experimental observations and to study the origin behind the two different transduction mechanisms, we performed extensive numerical simulations using COMSOL FEM solver (See Appendix A for the semianalytical calculations by island film theory[136,137]). First, we simulated and compared the single and ensemble of Si-NCs. Figure 5-4a and c show the resonances of an isolated Si-NC in aqueous solution while Figure 5-4b and d demonstrate a small part of a semi-random array of Si-NCs under identical conditions. As seen in Figure 5-4a, the resonance position of an isolated Si-NC redshifts and the extinction amplitude decreases as the surrounding refractive index increases. However, this effect is enhanced as more Si-NCs are assembled in a semi-random array. As can be seen in Figure 5-4f, the resonance shift for the array is about twice larger than for an isolated Si-NC. Also, the extinction reduction is increased by a similar amount (Figure 5-4g). These results are likely due to increased shielding effects on the interparticle electromagnetic coupling induced by the increased refractive index of the surrounding medium. While plasmonic metal nanostructures in similar arrangements have shown negligible coupling,[136] the mode extension for Si-NCs is significantly greater.[103] Furthermore, due to limited computation power, we only modelled 10 nanostructures in the semi-random array assembly. We foresee the observed effects to increase further for a larger array and to reduce the mismatch with experimental observations.

For the parameters of the fabricated Si-NCs, both magnetic and electric fields are enhanced at resonance. Interestingly, by separating the extinction cross section into electric and magnetic dipolar components (Figure 5-4e), the underlying mechanisms of the resonance shift and the extinction reduction can be unveiled. From Figure 5-4f and g, it appears that the magnetic resonance is responsible for the resonance redshift, while the extinction reduction is related to the electrical dipole. This observation explains the sources of the experimentally measured BRIS results. We can therefore associate the measured resonance centroid redshift and the extinction reduction with the respective Mie resonance modes.

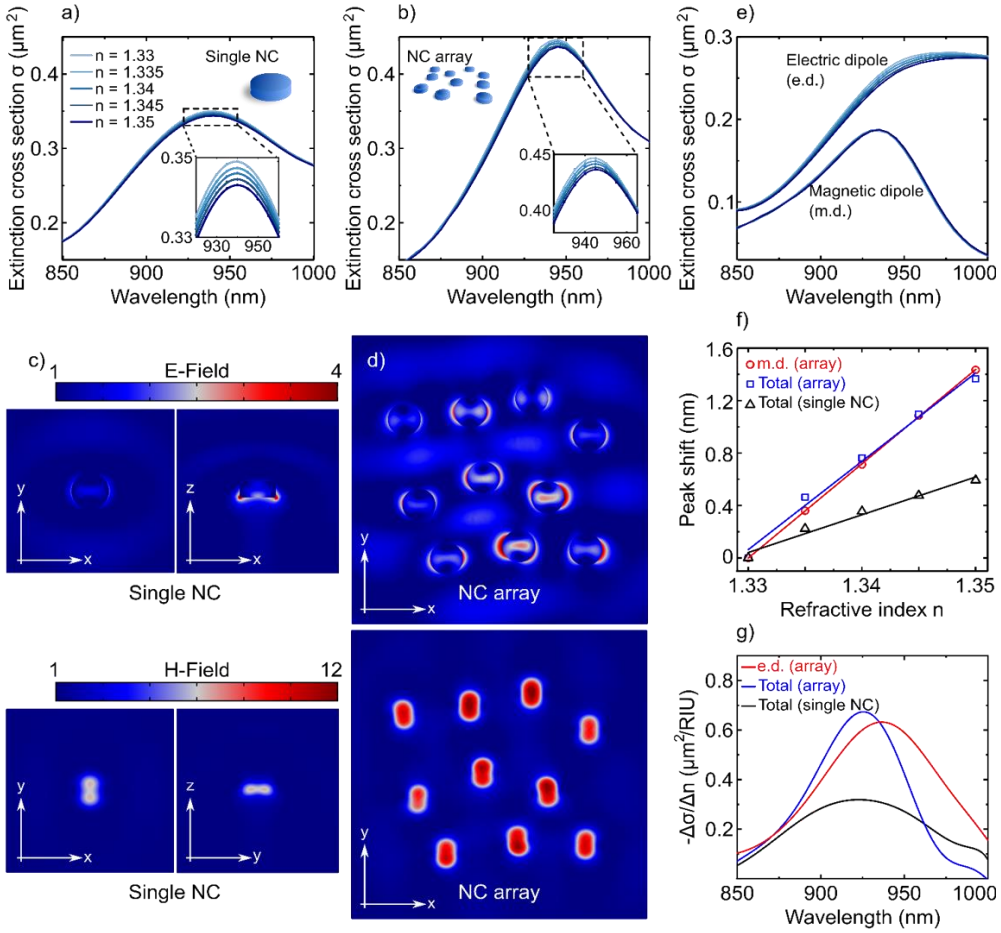

Figure 5-4 FEM simulations of Si-NCs. The extinction cross section of (a) a single Si-NC and (b) the average response from a semi-random Si-NC array of 10 particles, surrounded by media with different refractive indices. The E-field and H-field enhancements of (c) the single Si-NC and (d) the semi-random Si-NC array, around the resonance wavelength (940nm). (e) The electric and magnetic dipolar (e.d. and m.d.) components of the extinction cross section of the Si-NC array. (f) The extinction peak shifts due to changing refractive index of surrounding medium. The m.d. resonance of the Si-NC array (red circles) and the total extinction of the Si-NC array (blue squares) and total extinction of a single Si-NC (black triangles) are analysed and compared separately. (g) The wavelength dependence of the extinction cross section reduction (ERσ) due to changing refractive index.

5.3 Cancer marker detection

In order to demonstrate the biomolecule detection capability of our platform and compare both aforementioned transduction mechanisms, we focused on the

detection of prostate specific antigen, PSA. PSA is a protein cancer marker whose concentration in serum tends to overpass its normal level (4-10 ng/ml) for patients affected by prostate cancer.[126,127]

We used a sandwich immunoassay scheme (Figure 5-5a) for detecting PSA on the chip. The binding events are observed in real-time as a redshift of the resonance centroid and a reduction of the extinction. First, a selective monoclonal capture antibody for PSA is immobilized on the sensor surface in all the eight channels by a common inlet, through passive adsorption, similarly to clinically used enzyme linked immunosorbent assay (ELISA). Then, through individual inlets, eight calibration samples in PBS-BSA (Phosphate Buffer Saline-Bovine Serum Albumin, 1%) buffer with different PSA concentrations is flowed into the distinct channels and the PSA is captured by the antibody on the sensor surface, leading to additional adsorption signals. One of the eight channels was used as a control channel, with only PBS-BSA(1%) buffer flowing and no PSA. Following the PSA capture step, a polyclonal antibody is then introduced in all the channels as an amplification antibody, binding to PSA, resulting in larger and more detectable signals as well as a higher selectivity of the assay. Each step of the sandwich assay is adjusted to be 1 hour to have saturated signal shifts for each channel.

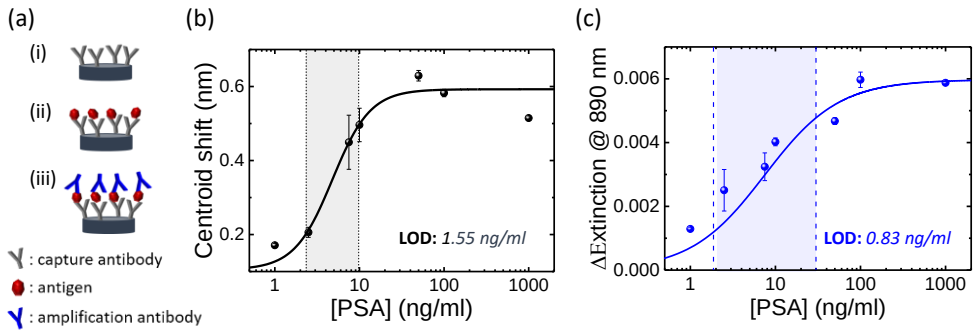

Figure 5-5 PSA detection results with semi-random Si-NC arrays.. (a) The sketch of the sandwich assay steps for antigen detection. First the capture antibody is immobilized on the sensor surface by passive adsorption (i), then the antigen is captured by the capture antibody (ii) and finally the signal is amplified by an amplification antibody (iii). (b-c) The calibration curve by the (b) centroid shifts and (c) extinction reduction due to the amplification antibody step obtained from the eight channels of the chip. Error bars represents the replicas of the measurement on the same chip.

The PSA calibration curves obtained by tracking the resonance centroid redshift and by tracking the extinction reduction at 890 nm are displayed in Figure 5-5b and c, respectively. The control channel shows no binding signal, suggesting a high specificity. The limit of detection (LOD), calculated conventionally as the EC10 value of the four-parameter logistic curve fit, reached by centroid shift tracking was 1.55 ng/ml, which is below the clinical cut-off concentration of PSA for

prostate cancer detection (4-10 ng/ml). Interestingly, the LOD reached by extinction reduction analysis of the same data is 0.83 ng/ml, outperforming the centroid tracking method as well as the well-developed LSPR counterpart.[34,103]

Beyond the LOD, another relevant parameter for diagnostics purposes is the dynamic range of the calibration curves (EC20-EC80 range), determining the working/operating ranges of the sensor and shown as the shaded regions in Figure 4. The dynamic range for the centroid shift-based curve is 2.35 – 9.79 ng/ml, while the dynamic range for the extinction reduction-based curve extends over 1.87 – 30.0 ng/ml. While both calibration curves are within the clinically relevant range, the extinction reduction-based sensing offers a higher dynamic range and a smaller LOD, which is beneficial for diagnostic applications. Error bars in Figure 5-5 represent the replicas of the measurements on the same chip. The coefficient of variation (CV) for replicated measurements is between 1.1% and 16.3% for centroid shifts and 0.7% and 25.9% for extinction reduction.

From our numerical simulations, we conclude that the electric dipolar mode, which dominates the extinction reduction mechanism, exhibits a better biomolecular sensing performance. This result is due to the higher exposure of the electrical mode to the surrounding medium. The magnetic dipolar modes are highly confined inside the Si-NCs, resulting in smaller response to the changes at the Si-NC surface.

Additionally, we have also calculated the total extinction reduction for the same measurement, by integrating the extinction peak over a wavelength range where the reduction is dominant, in order visualize the performance using a broadband illumination or detection scheme. Between 840 nm and 920 nm, the extinction reduction of the integrated signal lead to a very similar calibration curve for the PSA detection with LOD of 0.83 ng/ml (Figure 5-6), offering a possibility of even cheaper and simpler excitation and detection schemes. This result suggests that a LED light source and a simple CCD camera or photodiode can be employed for the excitation and readout, simplifying and reducing the cost of the set-up and paving the way for an efficient POC platform to be developed.

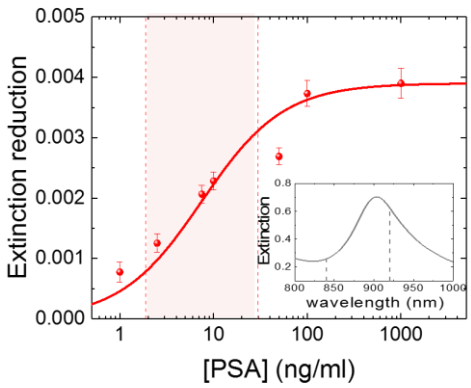

Figure 5-6 PSA calibration curve obtained by integrated extinction reduction. The inset shows the extinction wavelength range that is integrated (840-920nm).

5.4 Conclusions

The PSA detection results demonstrate that the on-chip sensing performance of partially randomized Si-NC arrays are competing with their periodic and LSPR based counterparts previously studied.[103] With the low LODs reached within the clinically relevant dynamic ranges, an early cancer detection platform can be used for human serum sample measurements. The ease of fabrication at a large scale combined with the simplicity of the surface chemistry based on passive adsorption in comparison to the SPR and LSPR applications, suggest Si-NC arrays as a powerful sensing tool. The total label-free assay time of 3 hours outperforms the commonly used clinical diagnostic scheme, ELISA, which takes 5 hours following and overnight immobilization of initial antibodies. Possibilities for resonance mode tuning for obtaining higher sensitivities, leaves room for improvement of such sensors.

In conclusion, we have demonstrated on-chip cancer marker detection using semi-randomized Si-NC arrays, employing the electric and magnetic dipole resonances for sensing, with low LOD and clinically relevant working ranges. We associated our two transduction mechanisms with the distinct electrical and magnetic dipolar modes, demonstrating the electric dipole mode sensitivity through the extinction reduction and magnetic dipole sensitivity through the resonance redshift. Our PSA detection results prove that the electric dipole mode, which is more exposed to the surrounding media, is outperforming the magnetic mode. The performance observed by tracking the extinction reduction at a single wavelength or a

wavelength range could bring in new possibilities of using cheaper and simpler, spectroscopy-free, optical set-ups and read-out devices.

The integrated LOC platform, as well as enabling parallel measurements, can also be used for multiplexing and more complicated immunoassay steps for more sophisticated measurements, in a highly controlled and automated environment. The silicon nanocylinders fabricated with colloidal lithography, exhibiting highly sensitive and specific sensing performance, is promising for on-chip POC diagnostic devices, due to faster, easier, cheaper and large-scale fabrication possibilities.

CONCLUSIONS AND OUTLOOK

In this thesis, we developed on-chip biosensing platforms based on the integration of PDMS microfluidics with optical nanoresonators. First, we demonstrated multiplexed cancer biomarker detection in human serum employing LSPR sensors and a microfluidic chip design for automated, real-time, and spontaneous sensing in up-to 32 sensing sites, comparing the platform performance to a gold standard ELISA technique. Next, we evaluated dielectric nanoresonators for biosensing in microfluidic environments. We presented our cancer marker detection results using periodic and semi-randomized arrays of silicon nano-cylinders and interpreted different transduction mechanisms through simulations.

The platforms and sensing results presented in this thesis brings the scientific community one step closer to understanding the capability of LSPR and dielectric nanoresonators (NR) for on-chip biosensing applications and demonstrates functional sensing modules to produce more complete POC devices in the future. The read-out platform can be engineered to fit in a small box or a handheld device. The future of diagnostics depends on the engineering of the sensitive resonance modes for optical NRs and on the efforts spent on real-life large-scale integration of the microfluidics technology. It is only a matter of re-designing the system to achieve more sensing sites and increase the multiplexing capabilities.

The research I conducted also leads to valuable questions to be addressed in the future. As shown in Chapters 4 and 5, we demonstrated the biomarker detection of Si-NR sensors with no special surface functionalization steps for the selective binding of molecules but only on the sensor sites. One advantage of our experimental approach is that we show specific and sensitive measurements without the need for specific treatments of the sensor surface. Studying the specific surface chemistry for Si-NR sensor substrates would be one of the remaining points to address to complete the study and improve the sensor performance.

Another important direction exposed by this thesis is the engineering of the Mie resonance modes for sharper and more sensitive extinction peaks. Here, very simple geometries of the Si-NR systems are used. The possibility to obtain sharper resonances with different geometries exhibiting fano-type resonances can be engineered and tested for sensing. Those sensors can then be integrated with microfluidics for highly-multiplexed and high-throughput sensing applications.

BIBLIOGRAPHY

(1) Rayleigh, J. W. S. B. *On the Scattering of Light by Small Particles*; 1871.

(2) Bohren, C. F.; Huffman, D. R. *Absorption and Scattering of Light by Small Particles*; 1998; Vol. 1.

(3) Maier, S. a. *Fundamentals and Applications Plasmonics : Fundamentals and Applications*; 2004; Vol. 677.

(4) Devaux, E.; Ebbesen, T. W.; Weeber, J. C.; Dereux, A. Launching and Decoupling Surface Plasmons via Micro-Gratings. *Appl. Phys. Lett.* **2003**, *83* (24), 4936–4938.

(5) Otto, A. Excitation of Nonradiative Surface Plasma Waves in Silver by the Method of Frustrated Total Reflection. *Zeitschrift für Phys. A Hadron. Nucl.* **1968**, *216* (4), 398–410.

(6) Kretschmann, E.; Raether, H. Radiative Decay of Non-Radiative Surface Plasmons Excited by Light. *Z. Naturforsch.* **1968**, *23* (November 1968), 2135–2136.

(7) Willets, K. A.; Van Duyne, R. P. Localized Surface Plasmon Resonance Spectroscopy and Sensing. *Annu. Rev. Phys. Chem.* **2007**, *58* (1), 267–297.

(8) Alkilany, A. M.; Thompson, L. B.; Boulos, S. P.; Sisco, P. N.; Murphy, C. J. Gold Nanorods: Their Potential for Photothermal Therapeutics and Drug Delivery, Tempered by the Complexity of Their Biological Interactions. *Adv. Drug Deliv. Rev.* **2012**, *64* (2), 190–199.

(9) Luo, S. C.; Sivashanmugan, K.; Liao, J. Der; Yao, C. K.; Peng, H. C. Nanofabricated SERS-Active Substrates for Single-Molecule to Virus Detection in Vitro: A Review. *Biosens. Bioelectron.* **2014**, *61*, 232–240.

(10) Liao, H.; Nehl, C. L.; Hafner, J. H. Biomedical Applications of Plasmon Resonant Metal Nanoparticles. *Nanomedicine* **2006**, *1* (2), 201–208.

(11) Johnson, P. B.; Christy, R. W. Optical Constants of the Noble Metals. *Phys. Rev. B* **1972**, *6* (12), 4370–4379.

(12) Ruemmele, J. A.; Hall, W. P.; Ruvuna, L. K.; Van Duyne, R. P. A Localized Surface Plasmon Resonance Imaging Instrument for Multiplexed Biosensing. *Anal. Chem.* **2013**, *85* (9), 4560–4566.

(13) Krasnok, A.; Makarov, S.; Petrov, M.; Savelev, R.; Belov, P.; Kivshar, Y. Towards All-Dielectric Metamaterials and Nanophotonics. *SPIE Opt. Optoelect.* **2015**, *9502*, 950203–950203.

(14) Fan, X.; Zheng, W.; Singh, D. J. Light Scattering and Surface Plasmons on Small Spherical Particles. *Light Sci. Appl.* **2014**, *3* (6), e179.

(15) Pendry, J. B. Negative Refraction Makes a Perfect Lens. *Phys. Rev. Lett.* **2000**, *85* (18), 3966–3969.

(16) Shalaev, V. M. Optical Negative-Index Metamaterials. *Nat. Photonics* **2007**, *1*, 41.

(17) García-Cámara, B.; Gómez-Medina, R.; Saenz, Jose, J.; Sepulveda, B. Sensing with Magnetic Dipolar Resonances in Semiconductor Nanospheres. *Opt. Express* **2013**, *21* (20), 23007–23020.

(18) Semouchkina, E.; Duan, R.; Semouchkin, G.; Pandey, R. Sensing Based on Fano-Type Resonance Response of All-Dielectric Metamaterials. *Sensors* **2015**, *15* (4), 9344–9359.

(19) Regmi, R.; Berthelot, J.; Winkler, P. M.; Mivelle, M.; Proust, J.; Bedu, F.; Ozerov, I.; Begou, T.; Lumeau, J.; Rigneault, H.; et al. All-Dielectric Silicon Nanogap Antennas to Enhance the Fluorescence of Single Molecules. *Nano Lett.* **2016**, *16* (8), 5143–5151.

(20) Yan, J.; Liu, P.; Lin, Z.; Yang, G. New Type High-Index Dielectric Nanosensors Based on the Scattering Intensity Shift. *Nanoscale* **2016**, *8*, 5996–6007.

(21) Groep, J. Van De; Polman, a. Designing Dielectric Resonators on Substrates : Combining Magnetic and Electric Resonances. *Opt. Express* **2013**, *21* (22), 1253–1257.

(22) Oe-24-3-2047.Pdf.Crdownload.

(23) Yu, Y. F.; Zhu, A. Y.; Fu, Y. H.; Luk, B.; Kuznetsov, A. I. High-Transmission Dielectric Metasurface with 2 π Phase. **2015**, *418* (4), 412–418.

(24) Butakov, N. A.; Schuller, J. A. Designing Multipolar Resonances in Dielectric Metamaterials. *Nat. Publ. Gr.* **2016**, *6* (38487), 1–8.

(25) Miller, M. M.; Lazarides, A. A. Sensitivity of Metal Nanoparticle Surface Plasmon Resonance to the Dielectric Environment. *J. Phys. Chem. B* **2005**, *109* (46), 21556–21565.

(26) Dahlin, A. B.; Tegenfeldt, J. O.; Hőök, F. Improving the Instrumental Resolution of Sensors Based on Localized Surface Plasmon Resonance. *Anal. Chem.* **2006**, *78* (13), 4416–4423.

(27) Singh, P. SPR Biosensors: Historical Perspectives and Current Challenges. *Sensors Actuators, B Chem.* **2016**, *229*, 110–130.

(28) Haes, A. J.; Stuart, D. A.; Nie, S.; Van Duyne, R. P. Using Solution-Phase Nanoparticles, Surface-Confined Nanoparticle Arrays and Single Nanoparticles as Biological Sensing Platforms. *J. Fluoresc.* **2004**, *14* (4), 355–367.

(29) Haes, A. J.; Chang, L.; Klein, W. L.; Van Duyne, R. P. Detection of a Biomarker for Alzheimer's Disease from Synthetic and Clinical Samples Using a Nanoscale Optical Biosensor. *J. Am. Chem. Soc.* **2005**, *127* (7), 2264–2271.

(30) Haes, a. J.; Hall, W. P.; Chang, L.; Klein, W. L.; Van Duyne, R. P. A Localized Surface Plasmon Resonance Biosensor: First Steps toward an Assay for Alzheimer's Disease. *Nano Lett.* **2004**, *4* (6), 1029–1034.

(31) Kim, S.-W.; Lee, J.-S.; Lee, S.-W.; Kang, B.-H.; Kwon, J.-B.; Kim, O.-S.; Kim, J.-S.; Kim, E.-S.; Kwon, D.-H.; Kang, S.-W. Easy-to-Fabricate and High-Sensitivity LSPR Type Specific Protein Detection Sensor Using AAO Nano-Pore Size Control. *Sensors (Basel, Switzerland)*. April 2017.

(32) Song, L.; Zhang, L.; Huang, Y.; Chen, L.; Zhang, G.; Shen, Z.; Zhang, J.; Xiao, Z.; Chen, T. Amplifying the Signal of Localized Surface Plasmon Resonance Sensing for the Sensitive Detection of Escherichia Coli O157:H7. *Sci. Rep.* **2017**, *7* (1), 3288.

(33) Acimovic, S. S.; Šípová, H.; Emilsson, G.; Dahlin, A. B.; Antosiewicz, T. J.; Käll, M. Superior LSPR Substrates Based on Electromagnetic Decoupling for On-a-Chip High-Throughput Label-Free Biosensing. *Light Sci. Appl.* **2017**, *6* (8), 1–8.

(34) Aćimović, S. S.; Ortega, M. A.; Sanz, V.; Berthelot, J.; Garcia-Cordero, J. L.; Renger, J.; Maerkl, S. J.; Kreuzer, M. P.; Quidant, R. LSPR Chip for Parallel, Rapid, and Sensitive Detection of Cancer Markers in Serum. *Nano Lett.* **2014**, *14* (5), 2636–2641.

(35) Chen, S.; Svedendahl, M.; Käll, M.; Gunnarsson, L.; Dmitriev, a. Ultrahigh Sensitivity Made Simple: Nanoplasmonic Label-Free Biosensing with an Extremely Low Limit-of-Detection for Bacterial and Cancer Diagnostics. *Nanotechnology* **2009**, *20* (43), 434015.

(36) Aćimović, S. S.; Kreuzer, M. P.; González, M. U.; Quidant, R. Plasmon Near-Field Coupling in Metal Dimers as a Step toward Single-Molecule Sensing. *ACS Nano* **2009**, *3* (5), 1231–1237.

(37) Feng, B.; Zhu, R.; Xu, S.; Chen, Y.; Di, J. A Sensitive LSPR Sensor Based on Glutathione-Functionalized Gold Nanoparticles on a Substrate for the

Detection of Pb^{2+}Ions. *RSC Adv.* **2018**, *8* (8), 4049–4056.

(38) Krasnok, A.; Caldarola, M.; Bonod, N.; Alú, A. Spectroscopy and Biosensing with Optically Resonant Dielectric Nanostructures. **2017**, No. January 2018.

(39) Bontempi, N.; Chong, K. E.; Orton, H. W.; Staude, I.; Choi, D.-Y.; Alessandri, I.; Kivshar, Y. S.; Neshev, D. N. Highly Sensitive Biosensors Based on All-Dielectric Nanoresonators. *Nanoscale* **2017**, *9* (15), 4972–4980.

(40) Yang, Y.; Kravchenko, I. I.; Briggs, D. P.; Valentine, J. All-Dielectric Metasurface Analogue of Electromagnetically Induced Transparency. *Nat. Commun.* **2014**, *5*, 5753.

(41) Davies, M. J.; Marques, M. P. C. Radhakrishnan, A. N. P. Microfluidics Theory in Practice. In *Microfluidics in Detection Science*; 2014; p pp 29–60.

(42) Sia, S. K.; Whitesides, G. M. Microfluidic Devices Fabricated in Poly(Dimethylsiloxane) for Biological Studies. *Electrophoresis* **2003**, *24* (21), 3563–3576.

(43) Reynolds, O. An Experimental Investigation of the Circumstances Which Determine Whether the Motion of Water Shall Be Direct or Sinuous, and of the Law of Resistance in Parallel Channels. *Philos. Trans. R. Soc. London* **1883**, *174*, 935–982.

(44) Melin, J.; Quake, S. R. Microfluidic Large-Scale Integration: The Evolution of Design Rules for Biological Automation. *Annu. Rev. Biophys. Biomol. Struct.* **2007**, *36* (1), 213–231.

(45) Garcia-Guirado, J.; Rica, R. A.; Ortega, J.; Medina, J.; Sanz, V.; Ruiz-Reina, E.; Quidant, R. Overcoming Diffusion-Limited Biosensing by Electrothermoplasmonics. *ACS Photonics* **2018**, *5* (9), 3673–3679.

(46) Unger, M. a; Chou, H. P.; Thorsen, T.; Scherer, A.; Quake, S. R. Monolithic Microfabricated Valves and Pumps by Multilayer Soft Lithography. *Science (80-.).* **2000**, *288* (5463), 113–116.

(47) Bhagat, a. a S.; Kuntaegowdanahalli, S. S.; Papautsky, I. Inertial Microfluidics for Continuous Particle Filtration and Extraction. *Microfluid. Nanofluidics* **2009**, *7* (2), 217–226.

(48) Gossett, D. R.; Weaver, W. M.; MacH, A. J.; Hur, S. C.; Tse, H. T. K.; Lee, W.; Amini, H.; Di Carlo, D. Label-Free Cell Separation and Sorting in Microfluidic Systems. *Anal. Bioanal. Chem.* **2010**, *397* (8), 3249–3267.

(49) Selmi, M.; Gazzah, M. H.; Belmabrouk, H. Optimization of Microfluidic Biosensor Efficiency by Means of Fluid Flow Engineering. *Sci. Rep.* **2017**, *7* (1), 1–11.

(50) Stanford University - Stanford Microfluidics Foundry https://web.stanford.edu/group/foundry/Microfluidic valve technology.html.

(51) Bhadra, P.; Shajahan, M. S.; Bhattacharya, E.; Chadha, A. Studies on Varying N-Alkanethiol Chain Lengths on a Gold Coated Surface and Their Effect on Antibody-Antigen Binding Efficiency. *RSC Adv.* **2015**, *5* (98), 80480–80487.

(52) Ahmad, A.; Moore, E. Electrochemical Immunosensor Modified with Self-Assembled Monolayer of 11-Mercaptoundecanoic Acid on Gold Electrodes for Detection of Benzo[a]Pyrene in Water. *Analyst* **2012**, *137* (24), 5839–5844.

(53) Kumar, A.; Rajesh, P.; Chaubey, A.; Grover, S. K.; Malhotra, B. D. Immobilization of Cholesterol Oxidase and Potassium Ferricyanide on Dodecylbenzene Sulfonate Ion-Doped Polypyrrole Film. *J. Appl. Polym. Sci.* **2001**, *82* (14), 3486–3491.

(54) Love, J. C.; Estroff, L. A.; Kriebel, J. K.; Nuzzo, R. G.; Whitesides, G. M. *Self-Assembled Monolayers of Thiolates on Metals as a Form of Nanotechnology*; 2005; Vol. 105.

(55) Kamra, T.; Chaudhary, S.; Xu, C.; Montelius, L.; Schnadt, J.; Ye, L. Covalent Immobilization of Molecularly Imprinted Polymer Nanoparticles on a Gold Surface Using Carbodiimide Coupling for Chemical Sensing. *J. Colloid Interface Sci.* **2016**, *461*, 1–8.

(56) Biswas, A.; Bayer, I. S.; Biris, A. S.; Wang, T.; Dervishi, E.; Faupel, F. Advances in Top-down and Bottom-up Surface Nanofabrication: Techniques, Applications & Future Prospects. *Adv. Colloid Interface Sci.* **2012**, *170* (1–2), 2–27.

(57) Chen, Y. Nanofabrication by Electron Beam Lithography and Its Applications: A Review. *Microelectron. Eng.* **2015**, *135*, 57–72.

(58) Yang, S. M.; Jang, S. G.; Choi, D. G.; Kim, S.; Yu, H. K. Nanomachining by Colloidal Lithography. *Small* **2006**, *2* (4), 458–475.

(59) Yavas, O.; Acimovic, S. S.; Garcia-Guirado, J.; Berthelot, J.; Dobosz, P.; Sanz, V.; Quidant, R. Self-Calibrating on-a-Chip LSPR Sensing for Quantitative and Multiplexed Detection of Cancer Markers in Human Serum. *ACS Sensors* **2018**, *3* (7), 1376–1384.

(60) Lee, M. J.; Ye, A. S.; Gardino, A. K.; Heijink, A. M.; Sorger, P. K.; MacBeath, G.; Yaffe, M. B. Sequential Application of Anticancer Drugs Enhances Cell Death by Rewiring Apoptotic Signaling Networks. *Cell* **2012**, *149* (4), 780–794.

(61) Gonzalez-Angulo, A. M.; Hennessy, B. T. J.; Mills, G. B. Future of Personalized Medicine in Oncology: A Systems Biology Approach. *J. Clin. Oncol.* **2010**, *28* (16), 2777–2783.

(62) Donzella, V.; Crea, F. Optical Biosensors to Analyze Novel Biomarkers in Oncology. *J. Biophotonics* **2011**, *4* (6), 442–452.

(63) Hornbeck, P. V. Enzyme-Linked Immunosorbent Assays. *Curr. Protoc. Immunol.* **2015**, *110* (1), 2–1.

(64) McKeating, K. S.; Aubé, A.; Masson, J.-F. Biosensors and Nanobiosensors for Therapeutic Drug and Response Monitoring. *Analyst* **2016**, *141* (2), 429–449.

(65) Vigneshvar, S.; Sudhakumari, C. C.; Senthilkumaran, B.; Prakash, H. Recent Advances in Biosensor Technology for Potential Applications – An Overview. *Front. Bioeng. Biotechnol.* **2016**, *4* (February), 1–9.

(66) Spindel, S.; Sapsford, K. E. Evaluation of Optical Detection Platforms for Multiplexed Detection of Proteins and the Need for Point-of-Care Biosensors for Clinical Use. *Sensors* **2014**, *14* (12), 22313–22341.

(67) Arlett, J. L.; Myers, E. B.; Roukes, M. L. Comparative Advantages of Mechanical Biosensors. *Nat. Nanotechnol.* **2011**, *6* (4), 203–215.

(68) Mukherji, S.; Punjabi, N. Label Free Integrated Optical Biosensors for Multiplexed Analysis. *J. Indian Inst. Sci.* **2012**, *92* (21), 254–293.

(69) Chen, P.; Chung, M. T.; Mchugh, W.; Nidetz, R.; Li, Y.; Fu, J.; Al, C. E. T. Multiplex Serum Cytokine Immunoassay Using Nanoplasmonic Biosensor Microarrays. *ACS Nano* **2015**, *9* (4), 4173–4181.

(70) Coskun, A. F.; Cetin, A. E.; Galarreta, B. C.; Alvarez, D. A.; Altug, H.; Ozcan, A. Lensfree Optofluidic Plasmonic Sensor for Real-Time and Label-Free Monitoring of Molecular Binding Events Over a Wide Field-of-View. *Sci. Rep.* **2014**, *4*, 1–7.

(71) Cappi, G.; Spiga, F. M.; Moncada, Y.; Ferretti, A.; Beyeler, M.; Bianchessi, M.; Decosterd, L.; Buclin, T.; Guiducci, C. Label-Free Detection of Tobramycin in Serum by Transmission- Localized Surface Plasmon Resonance. *Anal. Chem.* **2015**, *87* (10), 5278–5285.

(72) Ruemmele, J. A.; Hall, W. P.; Ruvuna, L. K.; Van Duyne, R. P. A Localized Surface Plasmon Resonance Imaging Instrument for Multiplexed Biosensing. *Anal. Chem.* **2013**, *85* (9), 4560–4566.

(73) Unser, S.; Bruzas, I.; He, J.; Sagle, L. Localized Surface Plasmon Resonance Biosensing: Current Challenges and Approaches. *Sensors* **2015**, *15* (7),

15684–15716.

(74) Yonzon, C. R.; Jeoung, E.; Zou, S.; Schatz, G. C.; Mrksich, M.; Van Duyne, R. P. A Comparative Analysis of Localized and Propagating Surface Plasmon Resonance Sensors: The Binding of Concanavalin A to a Monosaccharide Functionalized Self-Assembled Monolayer. *J. Am. Chem. Soc.* **2004**, *126* (39), 12669–12676.

(75) Anker, J. N.; Hall, W. P.; Lyandres, O.; Shah, N. C.; Zhao, J.; Van Duyne, R. P. Biosensing with Plasmonic Nanosensors. *Nat. Mater.* **2008**, *7* (6), 442–453.

(76) Joshi, G. K.; Deitz-McElyea, S.; Liyanage, T.; Lawrence, K.; Mali, S.; Sardar, R.; Korc, M. Label-Free Nanoplasmonic-Based Short Noncoding RNA Sensing at Attomolar Concentrations Allows for Quantitative and Highly Specific Assay of MicroRNA-10b in Biological Fluids and Circulating Exosomes. *ACS Nano* **2015**, *9* (11), 11075–11089.

(77) Yu, C.; Irudayaraj, J. Multiplex Biosensor Using Gold Nanorods. *Anal. Chem.* **2007**, *79* (2), 572–579.

(78) Wang, Y.; Tang, L. Multiplexed Gold Nanorod Array Biochip for Multi-Sample Analysis. *Biosens. Bioelectron.* **2015**, *67*, 18–24.

(79) Ouellet, E.; Lausted, C.; Lin, T.; Yang, C. W. T.; Hood, L.; Lagally, E. T. Parallel Microfluidic Surface Plasmon Resonance Imaging Arrays. *Lab Chip* **2010**, *10* (5), 581.

(80) Luo, Y.; Yu, F.; Zare, R. N. Microfluidic Device for Immunoassays Based on Surface Plasmon Resonance Imaging. *Lab Chip* **2008**, *8* (5), 694.

(81) Sackmann, E. K.; Fulton, A. L.; Beebe, D. J. The Present and Future Role of Microfluidics in Biomedical Research. *Nature* **2014**, *507* (7491), 181–189.

(82) Chin, C. D.; Linder, V.; Sia, S. K. Lab on a Chip Commercialization of Microfluidic Point-of-Care Diagnostic Devices. *Lab Chip* **2012**, *12*, 2118–2134.

(83) Volpetti, F.; Garcia-Cordero, J.; Maerkl, S. J. A Microfluidic Platform for High-Throughput Multiplexed Protein Quantitation. *PLoS One* **2015**, *10* (2).

(84) Norum, L. F.; Erikstein, B.; Nustad, K. Elevated CA 125 in Breast Cancer –A Sign of Advanced Disease. *Tumor Biol.* **2001**, No. 22, 223–228.

(85) Esteva, F. J.; Cheli, C. D.; Fritsche, H.; Fornier, M.; Slamon, D.; Thiel, R. P.; Luftner, D.; Ghani, F. Clinical Utility of Serum HER2/Neu in Monitoring and Prediction of Progression-Free Survival in Metastatic Breast Cancer Patients Treated with Trastuzumab-Based Therapies. *Breast Cancer Res.* **2005**, *7* (4), 436–443.

(86) Duffy, M. J. Tumor Markers in Clinical Practice: A Review Focusing on Common Solid Cancers. *Med. Princ. Pract.* **2012**, *22* (1), 4–11.

(87) Stieber, P.; Untch, M.; Nagel, D.; Seidel, D. Serum CEA and CA 15-3 as Prognostic Factors in Primary Breast Cancer. *Br. J. Cancer* **2002**, *86* (February), 1217–1222.

(88) Weigelt, B.; Peterse, J. L.; van 't Veer, L. J. Breast Cancer Metastasis: Markers and Models. *Nat. Rev. Cancer* **2005**, *5* (August), 591–602.

(89) Marella, D. S. Prognostic and Predictive Markers in Early Detection of Different Types of Cancers for Selected Organ Sites. *IOSR J. Pharm. Biol. Sci.* **2013**, *8* (4), 25–42.

(90) Harris, L.; Fritsche, H.; Mennel, R.; Norton, L.; Ravdin, P.; Taube, S.; Somerfield, M. R.; Hayes, D. F.; Bast, R. C. American Society of Clinical Oncology 2007 Update of Recommendations for the Use of Tumor Markers in Breast Cancer. *J. Clin. Oncol.* **2007**, *25* (33), 5287–5312.

(91) Fehm, T.; Becker, S.; Duerr-Stoerzer, S.; Sotlar, K.; Mueller, V.; Wallwiener, D.; Lane, N.; Solomayer, E.; Uhr, J. Determination of HER2 Status Using Both Serum HER2 Levels and Circulating Tumor Cells in Patients with Recurrent Breast Cancer Whose Primary Tumor Was HER2 Negative or of Unknown HER2 Status. *Breast Cancer Res.* **2007**, *9* (5), 1–8.

(92) Duffy, M. J. Serum Tumor Markers in Breast Cancer: Are They of Clinical Value? *Clin. Chem.* **2006**, *52* (3), 345–351.

(93) Pultz, B. dos A.; da Luz, F. A. C.; de Faria, P. R.; Oliveira, A. P. L.; de Ara??jo, R. A.; Silva, M. J. B. Far Beyond the Usual Biomarkers in Breast Cancer: A Review. *J. Cancer* **2014**, *5* (7), 559–571.

(94) Svedendahl, M.; Chen, S.; Dmitriev, A.; Kall, M. Refractometric Sensing Using Propagating versus Localized Surface Plasmons: A Direct Comparison. *Nano Lett.* **2009**, *9* (12), 4428–4433.

(95) Laforte, V.; Juncker, D.; Li, H. Cross-Reactivity in Antibody Microarrays and Multiplexed Sandwich Assays : Shedding Light on the Dark Side of Multiplexing. *Curr. Opin. Chem. Biol.* **2014**, *18*, 29–37.

(96) Oubina, A.; Gascon, J.; Barcelo, D. Multianalyte Effect in the Determination of Cross-Reactivities of Pesticide Immunoassays in Water Matrices. *Anal. Chim. Acta* **1997**, *347* (97), 121–130.

(97) Darwish, I. A. Immunoassay Methods and Their Applications in Pharmaceutical Analysis : Basic Methodology and Recent Advances. *Int. J. Biomed. Sciense* **2006**, *2* (2), 217–235.

(98) Otte, M. A.; Estévez, M. C.; Carrascosa, L. G.; González-Guerrero, A. B.; Lechuga, L. M.; Sepúlveda, B. Improved Biosensing Capability with Novel Suspended Nanodisks. *J. Phys. Chem. C* **2011**, *115* (13), 5344–5351.

(99) Chung, T.; Lee, S. Y.; Song, E. Y.; Chun, H.; Lee, B. Plasmonic Nanostructures for Nano-Scale Bio-Sensing. *Sensors* **2011**, *11* (11), 10907–10929.

(100) Liang, C.-C.; Liao, M.-Y.; Chen, W.-Y.; Cheng, T.-C.; Chang, W.-H.; Lin, C.-H. Plasmonic Metallic Nanostructures by Direct Nanoimprinting of Gold Nanoparticles. *Opt. Express* **2011**, *19* (5), 4768.

(101) Pang, S.; Cowen, S. A Generic Standard Additions Based Method to Determine Endogenous Analyte Concentrations by Immunoassays to Overcome Complex Biological Matrix Interference. *Sci. Rep.* **2017**, *7* (1), 1–10.

(102) Kaminski, T.; Gunnarsson, A.; Geschwindner, S. Harnessing the Versatility of Optical Biosensors for Target-Based Small-Molecule Drug Discovery. *ACS Sensors* **2017**, *2* (1), 10–15.

(103) Yavas, O.; Svedendahl, M.; Dobosz, P.; Sanz, V.; Quidant, R. On-a-Chip Biosensing Based on All-Dielectric Nanoresonators. *Nano Lett.* **2017**, *17* (7), 4421–4426.

(104) Long, F.; Zhu, A.; Shi, H. Recent Advances in Optical Biosensors for Environmental Monitoring and Early Warning. *Sensors* **2013**, *13* (10), 13928–13948.

(105) Gavela, A. F.; García, D. G.; Ramirez, J. C.; Lechuga, L. M. Last Advances in Silicon-Based Optical Biosensors. *Sensors* **2016**, *16* (285), 1–15.

(106) Passaro, V. M. N.; Dell'Olio, F.; Casamassima, B.; De Leonardis, F. Guided-Wave Optical Biosensors. *Sensors* **2007**, *7* (4), 508–536.

(107) Barizuddin, S.; Bok, S.; Gangopadhyay, S. Nanomedicine & Nanotechnology Plasmonic Sensors for Disease Detection - A Review. *J. Nanomedicine Nanotechnol.* **2016**, *7* (3), 1000373.

(108) Homola, J. Present and Future of Surface Plasmon Resonance Biosensors. *Anal. Bioanal. Chem.* **2003**, *377* (3), 528–539.

(109) Nguyen, H. H.; Park, J.; Kang, S.; Kim, M. Surface Plasmon Resonance: A Versatile Technique for Biosensor Applications. *Sensors* **2015**, *15* (5), 10481–10510.

(110) Leung, A.; Shankar, P. M.; Mutharasan, R. A Review of Fiber-Optic Biosensors. *Sensors Actuators, B Chem.* **2007**, *125* (2), 688–703.

(111) Caucheteur, C.; Guo, T.; Albert, J. Review of Plasmonic Fiber Optic Biochemical Sensors: Improving the Limit of Detection. *Anal. Bioanal. Chem.* **2015**, *407* (14), 3883–3897.

(112) Cao, J.; Sun, T.; Grattan, K. T. V. Gold Nanorod-Based Localized Surface Plasmon Resonance Biosensors: A Review. *Sensors Actuators, B Chem.* **2014**, *195*, 332–351.

(113) Hammond, J.; Bhalla, N.; Rafiee, S.; Estrela, P. Localized Surface Plasmon Resonance as a Biosensing Platform for Developing Countries. *Biosensors* **2014**, *4* (2), 172–188.

(114) Cambiasso, J.; Grinblat, G.; Li, Y.; Rakovich, A.; Cortés, E.; Maier, S. A. Bridging the Gap between Dielectric Nanophotonics and the Visible Regime with Effectively Lossless GaP Antennas. *Nano Lett.* **2017**, acs.nanolett.6b05026.

(115) Li, J.; Verellen, N.; Vercruysse, D.; Bearda, T.; Lagae, L.; Van Dorpe, P. All-Dielectric Antenna Wavelength Router with Bidirectional Scattering of Visible Light. *Nano Lett.* **2016**, *16* (7), 4396–4403.

(116) Shalaev, M. I.; Sun, J.; Tsukernik, A.; Pandey, A.; Nikolskiy, K.; Litchinitser, N. M. High-Efficiency All-Dielectric Metasurfaces for Ultracompact Beam Manipulation in Transmission Mode. *Nano Lett.* **2015**, *15* (9), 6261–6266.

(117) Shcherbakov, M. R.; Vabishchevich, P. P.; Shorokhov, A. S.; Chong, K. E.; Choi, D. Y.; Staude, I.; Miroshnichenko, A. E.; Neshev, D. N.; Fedyanin, A. A.; Kivshar, Y. S. Ultrafast All-Optical Switching with Magnetic Resonances in Nonlinear Dielectric Nanostructures. *Nano Lett.* **2015**, *15* (10), 6985–6990.

(118) Wu, A.; Li, H.; Du, J.; Ni, X.; Ye, Z.; Wang, Y.; Sheng, Z.; Zou, S.; Gan, F.; Zhang, X.; et al. Experimental Demonstration of In-Plane Negative-Angle Refraction with an Array of Silicon Nanoposts. *Nano Lett.* **2015**, *15* (3), 2055–2060.

(119) Zhang, J.; Liu, W.; Zhu, Z.; Yuan, X.; Qin, S. Strong Field Enhancement and Light-Matter Interactions with All-Dielectric Metamaterials Based on Split Bar Resonators. *Opt. Express* **2014**, *22* (25), 30889–30898.

(120) Evlyukhin, A. B.; Novikov, S. M.; Zywietz, U.; Eriksen, R. L.; Reinhardt, C.; Bozhevolnyi, S. I.; Chichkov, B. N. Demonstration of Magnetic Dipole Resonances of Dielectric Nanospheres in the Visible Region. *Nano Lett.* **2012**, *12* (7), 3749–3755.

(121) Evlyukhin, A. B.; Reinhardt, C.; Seidel, A.; Luk'Yanchuk, B. S.; Chichkov, B. N. Optical Response Features of Si-Nanoparticle Arrays. *Phys. Rev. B - Condens. Matter Mater. Phys.* **2010**, *82* (4), 1–12.

(122) Evlyukhin, A. B.; Eriksen, R. L.; Cheng, W.; Beermann, J.; Reinhardt, C.; Petrov, A.; Prorok, S.; Eich, M.; Chichkov, B. N.; Bozhevolnyi, S. I. Optical Spectroscopy of Single Si Nanocylinders with Magnetic and Electric Resonances. *Sci. Rep.* **2014**, *4*, 4126.

(123) Habteyes, T. G.; Staude, I.; Chong, K. E.; Dominguez, J.; Decker, M.; Miroshnichenko, A.; Kivshar, Y.; Brener, I. Near-Field Mapping of Optical Modes on All-Dielectric Silicon Nanodisks. *ACS Photonics* **2014**, *1*, 794–798.

(124) Pei, X.; Zhang, B.; Tang, J.; Liu, B.; Lai, W.; Tang, D. Sandwich-Type Immunosensors and Immunoassays Exploiting Nanostructure Labels: A Review. *Anal. Chim. Acta* **2013**, *758*, 1–18.

(125) Miroshnichenko, A. E.; Evlyukhin, A. B.; Yu, Y. F.; Bakker, R. M.; Chipouline, A.; Kuznetsov, A. I.; Luk'yanchuk, B.; Chichkov, B. N.; Kivshar, Y. S. Nonradiating Anapole Modes in Dielectric Nanoparticles. *Nat. Commun.* **2015**, *6*, 8069.

(126) Catalona, W. J., J. P. Richie, F. R. Ahmann, M. A. Hudson, P. T. Scardino, R. C. Flanigan, J. B. deKernion. Comparison of DRE and Serum PSA in the Early Detection of Prostate Cancer: Results of a Multicenter Clinical Trial of 6630 Men. *J. Urol.* **1994**, *151*, 1283–1290.

(127) Brawer, MK. Chetner, MP. Beatie, J. Buchner, DM. Vessella, RL. Lange, P. Screening for Prostatic Carcinoma with Prostate Specific Antigen. *J. Urol.* **1992**, *147*, 841–845.

(128) Liu, R.; Zhang, Y.; Zhang, S.; Qiu, W.; Gao, Y. Silver Enhancement of Gold Nanoparticles for Biosensing: From Qualitative to Quantitative. *Appl. Spectrosc. Rev.* **2014**, *49* (2), 121–138.

(129) Yavas, O.; Svedendahl, M.; Quidant, R. Unravelling the Role of Electric and Magnetic. *ACS Nano* **2019**, *13*, 4582–4588.

(130) Feuz, L.; Jonsson, M. P.; Höök, F. Material-Selective Surface Chemistry for Nanoplasmonic Sensors: Optimizing Sensitivity and Controlling Binding to Local Hot Spots. *Nano Lett.* **2012**, *12* (2), 873–879.

(131) Dahlin, A. B.; Chen, S.; Jonsson, M. P.; Gunnarsson, L.; Käll, M.; Höök, F. High-Resolution Microspectroscopy of Plasmonic Nanostructures for Miniaturized Biosensing. *Anal. Chem.* **2009**, *81* (16), 6572–6580.

(132) Wersäll, M.; Verre, R.; Svedendahl, M.; Johansson, P.; Käll, M.; Shegai, T. Directional Nanoplasmonic Antennas for Self-Referenced Refractometric Molecular Analysis. *J. Phys. Chem. C* **2014**, *118* (36), 21075–21080.

(133) Chen, S.; Svedendahl, M.; Duyne, R. P. V.; Käll, M. Plasmon-Enhanced

Colorimetric ELISA with Single Molecule Sensitivity. *Nano Lett.* **2011**, *11* (4), 1826–1830.

(134) Svedendahl, M.; Verre, R.; Käll, M. Refractometric Biosensing Based on Optical Phase Flips in Sparse and Short-Range-Ordered Nanoplasmonic Layers. *Light Sci. Appl.* **2014**, *3* (11), e220.

(135) Fredriksson, H.; Alaverdyan, Y.; Dmitriev, A.; Langhammer, C.; Sutherland, D. S.; Zäch, M.; Kasemo, B. Hole-Mask Colloidal Lithography. *Adv. Mater.* **2007**, *19* (23), 4297–4302.

(136) Svedendahl, M.; Käll, M. Fano Interference between Localized Plasmons and Interface Reflections. *ACS Nano* **2012**, *6* (8), 7533–7539.

(137) Odebo Länk, N.; Verre, R.; Johansson, P.; Käll, M. Large-Scale Silicon Nanophotonic Metasurfaces with Polarization Independent Near-Perfect Absorption. *Nano Lett.* **2017**, *17* (5), 3054–3060.

(138) Yu, Y. F.; Zhu, A. Y.; Paniagua-Domínguez, R.; Fu, Y. H.; Luk'yanchuk, B.; Kuznetsov, A. I. High-Transmission Dielectric Metasurface with 2π Phase Control at Visible Wavelengths. *Laser Photonics Rev.* **2015**, *9* (4), 412–418.

(139) Bedeaux, D.; Vlieger, J. *Optical Properties of Surfaces*; Imperial Collage Press: London, 2001.

APPENDIX A

The electric ($\bar{p}$) and magnetic ($\bar{m}$) dipole moments where calculated using:[138]

$$\bar{p} = \int_V \varepsilon_0(\varepsilon(\bar{r}) - \varepsilon_1)\bar{E}(\bar{r})\, d\bar{r}$$
$$\bar{m} = \frac{-i\omega}{2}\int_V \varepsilon_0(\varepsilon(\bar{r}) - \varepsilon_1)\bar{r} \times \bar{E}(\bar{r})\, d\bar{r} \quad (1)$$

where ω is the radial frequency of light, $\bar{E}(\bar{r})$ is the electric field at position ($\bar{r}$), and ε and ε_1 are the permittivities of the nanostructure and the ambient, respectively.

The electric (α_e) and magnetic (α_m) dipole polarizabilities can be extracted from FEM simulations and (1) using $\bar{p} = \bar{\alpha}_e\bar{E}_0$ and $\bar{m} = \bar{\alpha}_m\bar{H}_0$, where $\bar{E}_0$ and $\bar{H}_0$ are the background electric and magnetic fields. In the case of the 10 nanocylinder assembly, we use the *average* polarizabilities. We can then calculate the reflection and transmission coefficients for an infinite semi-random array by using the so-called island film theory.[136,137,139] The transmission coefficient at normal incidence can be written as:

$$t = \frac{2n_1\left(1 + \frac{k_0^2\rho^2\alpha_e\alpha_m}{4\varepsilon_0}\right)}{(n_1 + n_2)\left(1 - \frac{k_0^2\rho^2\alpha_e\alpha_m}{4\varepsilon_0}\right) - ik_0\rho(n_1n_2\alpha_m + \alpha_e/\varepsilon_0)}, \quad (2)$$

where k_0 is the wave vector of light in vacuum, ε_0 is the vacuum permittivity, ρ is the surface density of nanostructures (here ~2.1 μm^{-1}) and n_1 and n_2 are the ambient (~water) and substrate (glass) refractive index, respectively. The extinction in absorbance units, *E*, can then be calculated as $E = -log\left(|t|^2\frac{n_2}{n_1}\right)$.

Figure A-0-1 show the results based on the polarizabilities based on the simulations shown in Figure 5-4. The amplitude of the extinction peak is very similar to the experimental values. As these results of a semi-infinite array are based on the simulations of a few nanocylinders, as described in the Chapter 5,

also the peak redshift (BRIS ~70 nm/RIU) is of the same order as in Figure 5.4. However, the semianalytical approach also gives us the possibility to compare the simulated extinction reduction amplitude with the experimental values. We find that the largest amplitude of extinction reduction was 0.8 RIU^{-1}, based on the 10 nanocylinder simulation, which is below the experimental sensitivity. However, we stress that there is a significant enhancement of the sensitivity to the local refractive index compared to the single particle case. Thus, we are confident that a simulation of additional nanostructures, in a similar array arrangement, would yield sensitivities even more comparable to the experimental values.

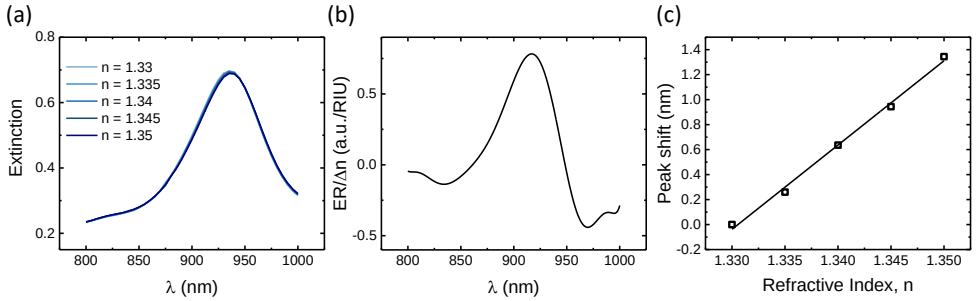

Figure A-0-1 Semianalytical calculations of an infinite array of nanoresonators . a) The extinction for a surface density of 2.1 μm^{-1}. b) The extinction sensitivity to the local refractive index as a function of wavelength. c) The extinction peak wavelength shift as the local refractive index, n_1, is changed from 1.33 to 1.35.